Broadband Long-wave Infrared Few-cycle Pulse Generation via Optical Parametric Chirped-pulse Amplification

by

Xuan Xiao

A dissertation submitted in partial fulfillment
of the requirements for the degree of
Doctor of Philosophy
(Nuclear Engineering and Radiological Sciences)
in the University of Michigan
2021

Doctoral Committee:

Professor Igor Jovanovic, Chair
Assistant Research Scientist Milos Burger
Professor Almantas Galvanauskas
Associate Professor Ryan McBride

Xuan Xiao
xuanxiao@umich.edu
ORCID ID: 0000-0002-8502-5316

DEDICATION

To healthcare professionals and scientists who fight against COVID-19 for the sake of humanity.

ACKNOWLEDGEMENTS

I am deeply indebted to my advisor, Prof. Igor Jovanovic, for his unparalleled support and unwavering guidance throughout my years in graduate school, and for introducing me to the field of optics and providing me research opportunities at the Center for Ultrafast Optical Science (CUOS). He directed me toward an exciting and cutting-edge dissertation topic, provided insightful discussions and comments in the research, and gave me rigorous training on source development. His trust, patience, and encouragement motivated me to overcome the difficulties in research.

I would like to extend my sincere thanks to John Nees and Dr. Milos Burger at the CUOS for the invaluable experimental training they provided and the vast technical experience they shared. Their enthusiasm, skill, and knowledge in research always inspired me. I also wish to thank Steve Katnik at the Physics department for the timely Quanta-ray maintenance, without which I would not complete this work in time. I will forever be thankful to my previous mentor Dr. Kyle C. Hartig at the University of Florida. He served as my early lab advisor in optics and provided me significant help on the spectroscopy project.

I am very grateful to have the opportunity to collaborate with Prof. Almantas Galvanauskas and his group members, Weizhi Du, Yifan Cui, and Mingshu Chen, from which I have gained a different perspective on this long-wave infrared (LWIR) project. Special thanks to my colleague Hao Huang for his excellent work on the ultrafast LWIR seed development and characterization, contributing to an essential part of this dissertation work. I must also thank all my other colleague, Patrick

J. Skrodzki, Jinpu Lin, Lauren A. Finney, Bryan W. Morgan, Nicholas Peskosky, Yong Ma in Prof. Jovanovic's group and Prof. Karl Krushelnick's group for their generous assistance on the experiments and their valuable advises both academically and personally. Thanks should also go to Dr. Scott F. Wandel, Dr. Mingwei Lin, Dr. Tan Shi, Dr. Felicia Sutanto, and Dr. Sunming Qin, whose help in my academic life cannot be underestimated.

I cannot leave the University of Michigan without mentioning Prof. Theodore B. Norris and Prof. Herbert G. Winful in the Electrical Engineering department for their distinguished lectures on classical optics, ultrafast optics, and nonlinear optics. They helped me develop a comprehensive understanding of these fields. I also wish to thank Prof. Ryan D. McBride in the Nuclear Engineering department. He first introduced me to plasma physics and later served as my committee member. I hereby thank all my committee members for their tremendous efforts and valuable suggestions on this dissertation work.

I would like to thank my family for their unrelenting supports from the other hemispheres of Earth. Many thanks to my friends, Dr. Jing Li, Dr. Yizhou Zhu, and Dr. Qi Wen, who were always there, especially in stressful moments. I thank Lani P. Wang, who told me to be assertive and strong.

Last but not least, this work has been supported by the U.S. Office of Naval Research under Contract No. N00014-17-1-2705, as well as the Rackham Predoctoral Fellowship program from the University of Michigan.

TABLE OF CONTENTS

LIST OF FIGURES

LIST OF APPENDICES

LIST OF ABBREVIATIONS

AR Antireflection

CCD Charge-Coupled Device

CPA Chirped-Pulse Amplification

CPM Critical Phase-Matching

CPS Coherent Pulse Stacking

CEP Carrier-Envelope Phase

DFG Difference-Frequency Generation

FWHM Full Width at Half Maximum

FWM Four-Wave mixing

FOM Figure of Merit

GVD Group-Velocity Dispersion

GVM Group-Velocity Mismatch

ICCD Intensified CCD

LWIR Long-Wave Infrared

MIR Mid-Infrared

MISER Monolithic Isolated Single-mode End-pumped Ring

MWIR Mid-Wave Infrared

MOPA Master Oscillator Power Amplifier

NCPM Noncritical Phase Matching

NOPA Noncollinear Optical Parametric Amplification

NOPCPA Noncollinear Optical Parametric Chirped-Pulse Amplification

OPA Optical Parametric Amplification

OPCPA Optical Parametric Chirped-Pulse Amplification

OPO Optical Parametric Oscillation

OPG Optical Parametric Generation

OP Orientation-Patterned

OR Optical Rectification

PVWC Poynting Vector Walk-off Compensation

PPLN Periodically Poled Lithium Niobate

QPM Quasi-Phase-Matching

RMS Root-Mean-Square

SSFM Split-Step Fourier Method

SHG Second-Harmonic Generation

SFG Sum-Frequency Generation

SFM Self-Phase Modulation

SVEA Slowly-Varying Envelope Approximation

TPM Tangential Phase Matching

TPA Two-Photon Absorption

XFROG Cross-Correlation Frequency-Resolved Optical Gating

ABSTRACT

Intense ultrashort laser sources in the Long-Wave Infrared (LWIR) spectral range are needed to gain a deeper understanding of many laser-matter interaction processes in laser pulse filamentation, strong-field physics, and laser-driven particle acceleration. Ultrashort LWIR pulses are also valuable in supporting applications in molecular spectroscopy, such as the investigations of molecular dynamics. However, the lack of suitable broadband laser gain media prevents the generation of the intense ultrashort LWIR pulses directly from laser oscillators and amplifiers, with the gaseous CO_2 laser being the only exception. The high cost and footprint of the advanced terawatt power level CO_2 systems with relatively long picosecond pulse duration hinders their wide application.

Optical Parametric Chirped-Pulse Amplification (OPCPA) is the most promising method for intense few-cycle pulse generation in the LWIR range. OPCPA uses an instantaneous nonlinear optical process–Optical Parametric Amplification (OPA) in a Chirped-Pulse Amplification (CPA) system to boost the energy of broadband ultrashort pulses. Mid-Infrared (MIR) OPCPA has reached peak powers on the order of several gigawatts, but when extended to the LWIR regime using near-infrared pumping, less than gigawatt powers have been produced. Generating radiation in the LWIR range reduces the conversion efficiency due to unfavorably higher quantum defect and thus requires higher-energy, nanosecond MIR pump lasers. To address the needs of intense ultrashort LWIR pulses, it is proposed to develop a LWIR OPCPA

source driven by MIR Er:ZBLAN fiber lasers.

This dissertation presents a numerical evaluation of GaSe and orientation-patterned GaAs performances in a nanosecond OPCPA, following a theoretical description of three-wave parametric interactions. The construction and performance of a nanosecond surrogate pump, based on optical parametric oscillation and amplification in $KTiOAsO_4$ crystals, is then reported. It operates at a central wavelength of 2.73 µm and produces >10 mJ pulses of ∼1 ns pulse duration at a repetition rate of 10 Hz. The surrogate pump source not only enables the experimental evaluation of the OPCPA architecture but also supports the initial assessment of large-core Er:ZBLAN fiber amplifiers. The LWIR seed pulses generated via direct difference-frequency generation in an $AgGaS_2$ crystal are centered at 10.3 µm with 1.1-µm bandwidth. The nanosecond GaSe OPCPA is further analyzed numerically in a noncollinear geometry, followed by the design and construction of a small-scale noncollinear GaSe OPCPA using the custom-built surrogate pump and seed sources for proof-of-concept studies. A design of nanosecond-long stretcher and compressor is also included, and the construction of a prototype that accommodates the current LWIR seed source with limited bandwidth is discussed. Although the broadband gain is still under testing, a preliminary study of small-signal gain in GaSe has been completed by using a narrow-band CO_2 laser as the seed. Single-shot spectrometers and an autocorrelator have also been developed for characterization in the LWIR range. The development of the prototype paves the way to the first demonstration of a MIR pumped LWIR OPCPA. The prototype is aimed to reach the peak power comparable to what has been demonstrated in the MIR range to date and could be scaled to a high peak and average power in the future by pump technologies such as high-energy, coherently-combined MIR fiber laser.

CHAPTER 1

Introduction

Following the development of Q-switching and mode-locking, the invention of CPA technique in 1985 by Strickland and Mourou [1] has enabled a several orders of magnitude jump in laser pulse peak power. Introduction of titanium-doped sapphire (Ti:Al_2O_3) as gain medium in 1986 [2] enabled large gain bandwidth, which circumvents the need to use self-phase modulation to broaden the laser pulse spectrally. As a result, ultrashort optical pulses can be produced at high peak powers in such Ti:sapphire CPA systems. Nowadays, the optics community has developed up to 10-PW laser facilities that employ hybrid CPA and OPCPA techniques. Exawatt-class facilities are under development via either incoherent or coherent beam combination of multiple beams at a 10-PW scale. The focused intensity achieved is on the order of 10^{22} W/cm^2 and is predicted to reach up to 10^{23} W/cm^2 before encountering potential material challenges. Currently, the highest average power of 300 W can be delivered by a PW class laser system operating at 10 Hz [3]. Kilowatt to megawatt average power laser systems are envisioned in the future. The development of high-peak and high-average power laser systems is of significant importance for exploration of many real-world applications in medical, materials, and environmental science [3].

Most of the intense ultrashort lasers today operate at a wavelength of ∼1 µm, albeit many laser-matter interaction processes, such as laser pulse filamentation, strong-field physics and attoscience, and laser-driven particle acceleration, greatly benefit from

ultraintense laser pulses with a wavelength longer than 1 µm because of the well-known wavelength scaling rule of the ponderomotive energy. Due to the lack of available broadband laser gain media in the MIR spectral range from 3 µm to 30 µm, no direct femtosecond laser source exists above 3 µm. The TW-peak-power CO_2 gas laser deserves special mention, but it operates at a relatively long pulse duration of several ps and a maximum repetition rate of several Hz [4, 5]. To extend the high-peak and high-average power sources to the MIR range, parametric downconversion devices employing suitable non-oxide nonlinear crystals provide promising alternatives [6–8]. In this chapter, a wide variety of approaches for coherent MIR light generation are briefly introduced, and the current status of the intense CO_2 lasers and LWIR parametric devices are subsequently reviewed. The motivation and objectives of this dissertation are also presented.

1.1 Background

In 1964, L.V. Keldysh described atomic ionization as a process that depends on the laser intensity (I) and wavelength (λ). The ponderomotive energy (U_p) of a free electron's cycle-averaged quiver motion in an electromagnetic field is proportional to $I\lambda^2$. With the surge in development of the now-ubiquitous ultraintense (up to 10 PW) Ti:sapphire lasers operating at $\sim$1 µm, the intensity-dependent laser-matter interaction processes have undergone substantial experimental examination and validation. However, the wavelength-scaling laws still remain under systematic experimental investigation due to the technological limitations in the development of longer-λ high-power sources. Since $U_p \propto I\lambda^2$, λ is a more effective control parameter than I to maintain high U_p without reaching the ionization saturation with the increase of I. This makes even moderate-high-intensity long-λ light sources highly valuable for strong-field physics, attoscience [9], and laser-particle acceleration [10]. Similarly, the nonlinear filamentary

propagation of intense ultrashort laser pulses in air also favors longer λ for increasing the guided power in a single filament without the loss of beam continuity and spatial coherence. The critical power for Kerr self-focusing scales with λ^2, and both the filament waist and self-channeling range are proportional to λ [11]. Therefore, the development of the intense ultrafast long-λ sources is of significant interest. From the spectroscopic viewpoint, ultrafast sources are also highly valuable since the absorption fingerprints of many molecules lie in the long-λ MIR range, and field-resolved MIR spectroscopy could be pursued to obtained another dimension of information of the molecular structures and dynamics [12]. High spectral brightness and average power are also essential to the improvement of the signal-to-noise ratio in spectroscopy [13].

A wide array of approaches has been explored to generate coherent light in the MIR range [8]. MIR sources based on semiconductor technology, such as lead-salt diode lasers and quantum cascade lasers, are efficient direct optical energy generators that rely on inner-band/inner-sub-band transitions operating beyond 3 µm up to THz regime with broad tunability. Novel architectures of semiconductor MIR laser today could support multi-ps pulse generation, but they have low peak power on the order of W. Their intrinsic beam divergence and astigmatism are also concerns for a number of applications, which require compensation [14, 15].

MIR sources based on rare-earth ion doped/transition metal doped materials provide another efficient approach and rely on electronic/vibronic transitions operating at the shorter wavelength side of MIR regime, from 2–5 µm. Exciting developments have been reported in lasers employing Tm^{3+}-, Ho^{3+}-, and Er^{3+}-doped oxide/fluoride crystals and glass fibers since 1990s. Up to multi-tens of GW peak power has been achieved in Ho:YAG/Ho:YLF CPA systems generating 3 mJ of pulses at 5 kHz with a pulse duration of 530 fs [16], and 220 mJ of pulses at 100 Hz with a pulse duration of 16 ps [17]. High-power Ho:YLF lasers operating in the ps regime provide ideal pump sources for >4 µm OPCPA based on non-oxide crystals due to the reduced linear and

two-photon absorption and reduced photon ratio mismatch when pumping at ∼2 µm in comparison to ∼1-µm pumping [18, 19]. Er:ZBLAN fiber lasers operating around 3 µm have also been attracting considerable attention recently. Multi-kW 497-fs mode-locked pulses has been demonstrated [20], and ns operation up to 58 kW in Er:ZBLAN fiber amplifier has been explored [21]. In the past two decades, significant progress has been made in the development of Cr^{2+}- and Fe^{2+}-doped chalcogenide lasers. The construction of the 1-GW, 1-kHz, 2.5-µm Cr:ZnSe-based ultrafast CPA system provides an excellent example [22], whereas 4-µm Fe:ZnSe laser has achieved tens of MW power in the ns regime [23, 24] and 20 GW in fs regime [25].

The CO_2 laser is one of the earliest gas lasers invented in 1960s. It has vibrational-rotational transitions in the range of 9–11 µm, particularly at 10.6 µm. Pulse operation of CO_2 laser in the ps regime can be achieved by semiconductor switching [26], optical Kerr switching [27], direct mode-locking [28], or optical-free-induction-decay technique [29]. Combined with high-pressure CO_2 amplifiers, multi-TW peak power has been obtained in today's advanced CO_2 lasers [4, 5]. However, the repetition rate of such CO_2 lasers is limited by the electrical discharge pumping mechanism based on transversely excited atmospheric or radio frequency discharges to a few Hz. Recent progress on optical pumping technique provides a promising route to alleviate this limitation [30, 31].

Parametric downconversion devices based on nonlinear three-wave mixing have been spectacularly successful when attempting to access the MIR regime. New oxide and non-oxide materials have been synthesized and investigated over the past few decades. Generally, compared to the oxide crystals, the non-oxide crystals have a much higher nonlinear coefficient and larger transparency range in the longer wavelength side (>5 µm) of the MIR range, but suffer from more growth defects and corresponding residual losses due to the limited growth technology. For optically isotropic media with large nonlinear coefficients, the Quasi-Phase-Matching (QPM)

technique allows their application in downconversion devices. Few-hundreds of GW peak power and few-tens of W average power have been achieved in 3–4 µm few-cycle OPCPA using MgO:$LiNbO_3$, $KTiOAsO_4$ (KTA), and $LiNbO_3$ crystals [11,32,33]. Few-cycle OPA/OPCPAs with wavelength that extends beyond 5 µm are still limited in their peak power to ∼10 GW and in their average power to several W when using $ZnGeP_2$ (ZGP) and $AgGaS_2$ (AGS) crystals [34–36]. OPCPA based on the QPM technique can be operated around 3 µm with Periodically Poled Lithium Niobate (PPLN), but the peak power has been limited to below GW level [32, 37, 38].

The design and deployment of MIR sources also require detailed knowledge of molecular vibration absorption in atmosphere since the presence of water vapor, carbon dioxide, and the ozone layer strongly affect the transmittance [39, 40]. Figure 1.1 shows the spectral structure of the transmittance in the MIR range under different conditions. Curve (a) gives a 4.7-m transmittance experimentally measured in a typical laboratory environment (25° room temperature, 62% humidity) [39]. In comparison, the Earth's atmospheric transmittance at high altitude simulated with data from the ATRAN database [41] is shown in curve (b). ATRAN models the transmission by using the predicted water vapor overburden at the zenith. As can be seen, the Mid-Wave Infrared (MWIR) window from 3–5 µm and the LWIR window from 8–14 µm are separated by the 5–8 µm H_2O continuum, and the 2.5–3 µm H_2O band defines the short-wavelength boundary of the MWIR window. The boundary at the long-wavelength end of LWIR window is set by CO_2 absorption, and its strong absorption at ∼4.3 µm CO_2 divide the MWIR window into two narrower ones. A strong O_3 line around 9.6 µm in ATRAN simulation originates from absorption in the ozone layer at an altitude of ∼22 km, which is obviously not revealed in the laboratory data.

As has been discussed, impressive progress has been made in developing intense few-cycle sources in the MWIR range, while the LWIR regime is still a *hic sunt dracones* land for solid-state sources. Strong interest has been expressed in the

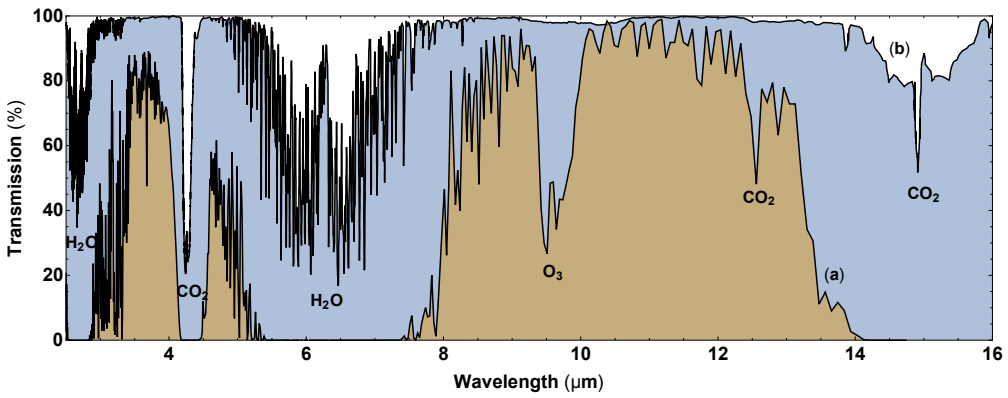

Figure 1.1: (a) Transmittance of Earth's atmosphere [41], and (b) transmission of air under laboratory conditions (25°, 62% humidity, 4.7 m) [39] in the spectral range of 2.5-16 μm.

scientific community to address the challenges of LWIR production, which motivates the focus of this dissertation.

1.2 State-of-the-art carbon dioxide laser

Conventional CO_2 lasers operating at atmospheric pressure are limited by the gain spectral profiles that are strongly modulated by vibrational-rotational transitions. To circumvent this limitation, gas pressures in the range of several times the atmospheric pressure have to be used in the CO_2 laser media, which provides the broadening of the rotational lines via particle collisions. A complete smoothing of the gain spectrum occurs at ∼25 atm, which is not applicable in a system with electrical discharge pumping. At a more realistic pressure of ∼10 atm, multi-ps pulse amplification can still be supported, but pulse splitting can occur due to the residual spectral modulation. The top and center plots in Figure 1.2 show the gain spectra of CO_2 at 1 bar and 10 bar, respectively [42]. As the pulses are amplified, such splitting can be mitigated at high laser intensities since the rotational lines can be broadened in the electric field of the laser pulse due to the ac Stark effect. Under such conditions, the extracted energy is distributed over decreasing number of pulses. The direct amplification developed

in the Neptune laboratory at the University of California, Los Angeles, presents an example of CO_2 amplifiers assisted by pressure broadening in the initial stage of amplification and field broadening in the final amplifier stage. The 10P vibrational branch was used. A 3-ps pulse train containing only 2–3 pulses has been obtained from its final large-aperture 3-pass amplifier operated at 2.5 atm. ∼45% of the energy was concentrated into the strongest pulse under a conservative estimate, which corresponds to a peak power of 15 TW [4].

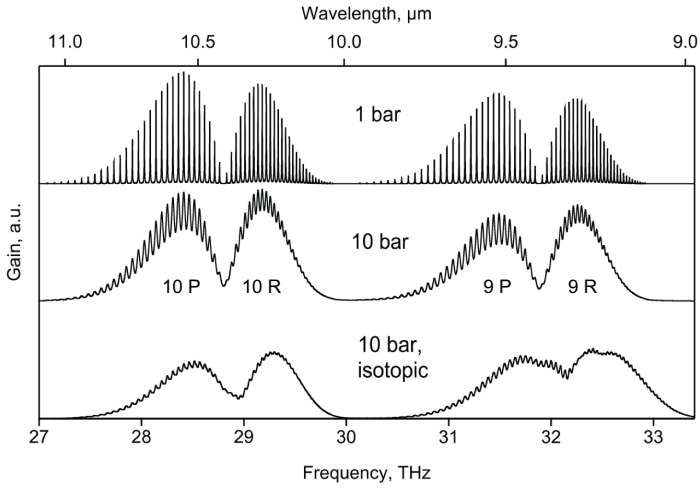

Figure 1.2: Gain spectra of CO_2 laser media at 1 bar and 10 bar compared with isotopically-enriched CO_2 at 10 bar [42].

The CPA approach has been adopted in the state-of-the-art CO_2 laser at the Brookhaven National Laboratory. This reduces the laser intensity of the pulses on the amplifier optics and allows the adoption of high-pressure CO_2 amplifiers with smaller apertures for the final stage. Additionally, the high-pressure amplifiers are filled with isotopically-enriched CO_2, such that a more homogeneous gain spectrum can be obtained as shown in the bottom plot in Figure 1.2. In such a high-pressure mixed-isotope amplifier, the smoothed spectrum of 10P vibrational branch is suitable for amplification of 3-ps pulses without pulse splitting, whereas the 9R branch has a wider bandwidth which could support amplification of 1.7 ps pulses at 9.2 μm in a

single pulse format. This configuration has delivered single 2-ps pulses with a peak power of 5 TW [5].

Implementation of the CPA technique eliminates the fundamental bottleneck to further increase the peak power of CO_2-amplifier-based LWIR lasers [5]. Scaling to larger active volumes for 100-J level output is readily achievable [4]. However, it is difficult to obtain a broader gain bandwidth for shorter pulse amplification since a stable electric discharge is hard to be maintained at pressures >10 atm. Additionally, the average power of the current CO_2 lasers is also limited by the electrical discharge pumping mechanism. Optical excitation is known as an alternative route, which could eliminate the limitations of the operating pressure and the achievable repetition rate. Historically, this concept was inhibited by the lack of a suitable pump laser in this spectral region. Recent progress in the development of J-class, ∼100-ns Fe:ZnSe lasers tunable around 4.3 µm significantly increases the feasibility of optically-pumped CO_2 laser [24]. Numerical simulations have shown that optically-pumped CO_2 amplifiers at 20 atm should be capable of amplifying ps pulses to GW peak power [30]. Experimental demonstration of this scheme is still in progress, but a very high gain coefficient of 30%/cm has already been observed in a 50-torr CO_2 medium optically pumped by a 4.3-µm Fe:ZnSe laser producing 40-ns pulses with ∼2 mJ of energy at a repetition rate of 10 Hz. A prediction has been made that ⩽10%/cm can still be obtained in 20-atm optically pumped CO_2 by increasing the pump energy, which is several times higher than that pumped by electric discharge [43]. Such high gain per unit length reduces the required length of the active media and thus minimizes the gain-narrowing effect, which is important for the amplification of single ps pulses.

The development of state-of-the-art CO_2 lasers contributes substantially to the delivery of LWIR capabilities for high-impact scientific research. It is presently the only kind of source that has reached terawatt-class peak power in the LWIR spectral regime. However, due to the inherent limitations of the CO_2 lasers, such as their

limited pulse duration to $\gtrsim$ps, the current limitation in repetition rate due to the discharge pumping mechanism, the large footprint and high cost of the advanced schemes, etc., there is a growing interest in parametric processes as an alternative for high-power few-cycle LWIR pulse generation.

1.3 Current status of long-wave infrared (LWIR) solid-state sources

At present, the primary approach to extend the operation to LWIR regime with all-solid-state technology is frequency downconversion employing non-oxide nonlinear crystals with extended transparency beyond 4 µm [6]. Such non-oxide crystals generally have smaller bandgap energies E_g when compared to the oxide crystals. Empirically, since the index of refraction depends on the material bandgap as $\sim {E_g}^{-1/4}$, non-oxide crystals have larger indices of refraction and correspondingly higher nonlinear coefficients based on Miller's rule. However, the small bandgap limits the pump photon energy to $\sim E_g/2$, such that the detrimental Two-Photon Absorption (TPA) can be avoided. As a result, it is difficult to pump most of the non-oxide crystals with 0.8-µm Ti:sapphire lasers or even the 1-µm Nd^{3+}/Yb^{3+}-doped lasers for direct conversion. Longer-wavelength pump sources, such as $Tm^{3+}/Ho^{3+}/Er^{3+}$-doped lasers or cascaded parametric conversion have to be used in these situations. Although it does not strictly lie in the LWIR regime, two Ho:YLF laser pumped OPCPA based on ZGP crystals has extended the operating wavelength to 5 µm [18, 34] and 7 µm [35, 44]. The 5-µm OPCPA has reached 12.5 GW, whereas the 7-µm OPCPA has enabled 4.0 GW peak power [17, 34]. The only GW-level LWIR parametric source has been developed to operate at a central wavelength of 8.9 µm with an average power of ~83 mW. The source is based on Difference-Frequency Generation (DFG) of two near-infrared fields generated in the primary Ti:sapphire laser-driven OPA stage based on β-BaB_2O_4

(BBO) crystals, which is tunable in the range of 5.3–8.9 µm [36]. The DFG is performed in a 10×10×1 mm^3 AGS crystal. Such an approach is simple to implement but at the expense of Carrier-Envelope Phase (CEP) stability of the generated LWIR pulses. Additionally, further energy scaling of such DFG/OPA is constrained because of the finite available crystal aperture and the limited interaction length due to temporal walk-off. Recent progress in the development of ternary chalcogenides such as $LiGaS_2$ (LGS), $LiInS_2$ (LIS), $LiGaSe_2$ (LGSe), and $LiInSe_2$ (LISe), etc. allows the 0.8/1-µm pumping without TPA, but at the expense of two orders of magnitude lower nonlinear coefficients. A 9-µm LGS-based OPCPA pumped by 1-µm Yb:YAG CPA system (10 kHz, 1 ps, 14 mJ) has been demonstrated. Due to the lack of thick crystals, two LGS crystals are cascaded in both the preamplification and the main amplification stages. This OPCPA has enabled generation and amplification of 142-fs pulses with ∼0.1 GW peak power and 140 mW average power [12]. This scheme is readily scalable to ∼0.7 GW with thicker Antireflection (AR)-coated LGS crystals, such that the amplification saturation could be reached and the Fresnel reflections from multiple uncoated crystal surfaces could be reduced [12]. Further scaling requires the deployment of higher energy pump pulses with longer pulse duration, such as the one demonstrated in a cryogenic Yb:YAG CPA (2 kHz, 15 ps, 32 mJ) [45]. The LGS-based OPCPA exhibits passive CEP stability as it is seeded by near-infrared supercontinuum generated with the same pump source.

Figure 1.3 summarizes the characteristics of current ultrashort LWIR parametric sources with peak power from 0.01 GW to 1 TW. For comparison, parametric sources operating at central wavelengths in the range of 3–8 µm covering the MWIR window are also included. The diameter of the circles is logarithmically proportional to the average power of the sources. As can be seen in the figure, most of the sources are in the MWIR window, and their peak and average power vary significantly. The maximum peak and average power have reached 284 GW [46] and 11.5 W [38], respectively, both operating

at ∼3 µm. In general, generating radiation at an increasingly longer wavelength suffers from unfavorably higher quantum defects, which limits the conversion efficiency. The two emerging LWIR sources [12, 36] discussed earlier operate at a shorter-wavelength region of the LWIR window and have not achieved peak powers beyond 1 GW. Due to the high repetition rate, the average power of the two sources is on the order of ∼100 mW. Currently, only the LGS-based OPCPA provides CEP stability, whereas the AGS-based DFG source is CEP-unstable, which is indicated in Figure 1.3 as a pattern-filled circle.

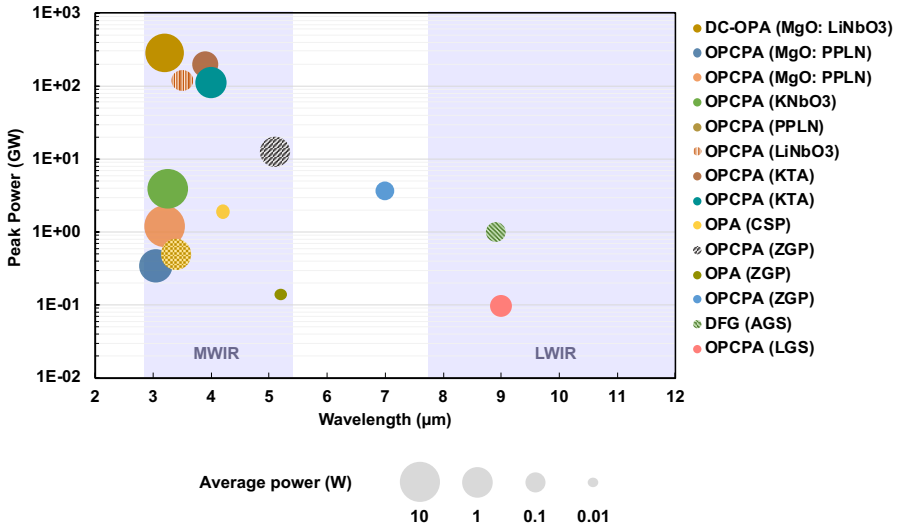

Figure 1.3: Performance of current ultrashort solid-state parametric MWIR-LWIR sources [11, 12, 17, 32–34, 36–38, 46–50]. The diameter of each circle is logarithmically proportional to average power. The pattern-filled circles represent sources that are CEP-unstable.

The previous discussion summarizes a handful of ultrashort LWIR parametric sources that are able to support relatively high peak power (>0.1 GW) for applications in strong-field physics and laser-pulse filamentation. There are numerous low-energy sources in the LWIR region designed for spectroscopy applications, which are capable of operating at a very high repetition rate (>10 MHz) based on mode-locked thin-disk pump lasers. Multi-octave spectra have been generated with a Fourier limit equivalent to few-cycle LWIR pulses. The pulse energies are typically on the order of nJ [13, 51, 52].

Examples include a 24-mW, 9.5-µm intrapulse DFG in GaSe driven by a 77 MHz, 2-µm Kerr-lens mode-locked Ho:YAG thin-disk oscillator [51], a 100-MHz, 100-mW, 11.5-µm intrapulse DFG [13], and a 37.5-MHz, 1.3-W, 8.5-µm OPA [52], both in LGS crystals pumped by 1-µm Kerr-lens mode-locked Yb:YAG thin-disk oscillator. A source based on DFG in GaSe by mixing the fundamental and Raman shifted pulses from the 1.55-µm mode-locked Er:fiber oscillator presents another approach to the production of broadband LWIR pulses at a high repetition rate of 250 MHz. Wide tunability in the range of 8–14 µwas achieved with an average power of ∼1 mW at 10 µm [53]. The DFG driven by synchronously-pumped Optical Parametric Oscillation (OPO) in $AgGaSe_2$ (AGSe) [54]/$HgGa_2S_4$ (HGS) [55] crystals has been demonstrated at a repetition rate of 53 MHz/80MHz with fs pulse durations. The source is tunable in the range of 5–17 µm/4–12 µm with average power of ∼10 mW at 10 µm [54, 55]. Pumped by a 2.5-µm mode-locked Cr^{2+}:ZnS laser, the intrapulse DFG has reached 150 mW in ZGP in the spectral range of 5.8–12.5 µm [56]. Implementations using Tm:fiber CPA operating ∼2 µm for pumping intrapulse DFG in GaSe have been demonstrated [57, 58]. Generated pulses span the wavelength range of 6–18 µm up to 0.5 W average power at a repetition rate of 50 MHz [57]. Operation at a moderate-high repetition rate of 1.25 MHz has also been reported to enable average power of 450 mW with a spectrum covering 3.7–18 µm [58]. There are also many low-repetition-rate (<10 kHz), low-energy demonstrations mainly via DFG/intrapulse DFG. Cascaded conversion [59–62] that adopts intermediate Optical Parametric Generation (OPG)/OPA/OPCPA stages pumped by a Ti:sapphire laser is the main approach, and direct conversion [63–65] driven by dual-wavelength Ti:sapphire systems has also been explored. Nonlinear media include AGS [60–63], GaSe [65], LGS [59], and HGS [61] crystals. It should be noted that these low-energy ultrashort LWIR sources are highly valuable as potential front-ends for high-energy OPA/OPCPA. In addition to frequency downconversion, supercontinuum generation in chalcogenide

fibers [66–68] and bulk materials [69–72] provides another useful tool for spectroscopy. It is also frequently adopted for seeding the OPA/OPCPA. However, the strongly nonlinear nature of supercontinuum generation complicates the pulse compression.

1.4 Motivation

Self-channeling of intense laser pulses in the atmosphere remains of significant interest over the past 20 years with the surge in development of the now ubiquitous Ti:sapphire lasers [73, 74]. Laser-pulse filamentation is capable of transporting high-energy beams over long distances with minimal diffraction losses due the dynamic equilibrium between the Kerr self-focusing, the defocusing in the laser plasma, and the diffractive divergence. Extensive theoretical and experimental studies of the filamentation involving complex nonlinear wave dynamics have been performed, and a wide variety of applications such as atmospheric remote sensing, free-space communication, supercontinuum generation, etc. have been suggested [75]. To initiate filamentation, it is required to reach the critical peak power (P_{cr}) for Kerr self-focusing. Intensity scaling to well beyond critical power unavoidably breaks up the beam into multiple small-scale filaments, each containing a power on the order of P_{cr}. In order to increase both the guided power and transverse dimension of a filament without breaking its spatial coherence, wavelength scaling can be used as the P_{cr} is proportional to the laser wavelength squared. Based on the numerical simulations, MIR filaments are regulated by new collapse-arresting mechanisms via carrier wave self-steepening and higher harmonic walk-off that are different than plasma defocusing in the conventional visible-to-near-infrared filaments. They feature a much longer and wider filamentary structure, significantly lower ionization losses, and the ability to propagate over a long distance with multiple TW of power contained in a single solitonic hotspot [76–78]. Between the two prominent atmospheric transmission windows, the LWIR window has shown enhanced propagation

of high-energy ultrashort pulses in fog and clouds along with reduced perturbation from atmospheric turbulence [79]. Experimental demonstrations currently lag behind the simulations due to the technological challenges in the development of intense ultrashort long-wavelength sources. Until recently, most of the atmospheric laser-induced filamentation experiments have been limited to the visible or near-infrared range. Only a few implementations have been experimentally demonstrated in ambient air [11, 80–82]. The first MIR filamentation study was enabled by a 3.9-µm KTA OPCPA generating 200 GW, 100 fs pulses. The experiment has produced unique results such as the generation of multiple odd-order harmonics and strong plasma refraction [11, 80]. Complex off-axial beam dynamics of the MIR filaments have also been analyzed in the following angle-resolved spectral analysis [81]. Supported by the state-of-the-art TW-class ps CO_2 lasers, a self-guided single centimeter-scale-diameter megafilament containing ∼1 TW over 20 Rayleigh lengths in air has been demonstrated with similar harmonic generation properties [82].

Precise knowledge of nonlinear refractive index n_2 of air provides a fundamental basis for the understanding of high-intensity light-matter interactions such as filamentation. Benefit from the recent progress in the development of high-power CO_2 laser, the measurement of n_2 value of air has been performed at 10 µm using four-wave mixing of two rotational lines from a 200 ps CO_2 laser pulse [83, 84]. The long pulse width and the time-integrated measurement prevented the separation of the electronic and rotational contributions. Based on an ultrafast fs DFG source, time-resolved measurement of the nonlinear response of major air constituents is enabled at elevated pressure in the LWIR range via supercontinuum spectral interferometry [85]. The electronic nonlinear indices are measured in this study, whereas the rotational responses are shadowed due to the collisional dephasing at high pressure. Such problem may be alleviated via the development of high-power ultrafast LWIR sources.

The direct impetus for this dissertation is the intent to support the new regimes

of laser-pulse filamentation and to explore the air nonlinearities in the LWIR spectral range via more compact high-power solid-state sources of ultrashort LWIR pulses. As has been discussed in Section 1.3, much effort has been committed to source development in the MWIR range, which has enabled peak powers of up to several hundreds of GW. Because of the decreasing conversion efficiency when extending the operation to the LWIR range due to the Manley–Rowe relations, higher-energy MIR pump lasers are required. The central objective of this dissertation research is to explore the potential for generating few-cycle TW pulses in the LWIR regime via OPCPA pumped by high-energy, nanosecond 2.75-µm pulses that can be produced by Er:ZBLAN fiber lasers employing the Coherent Pulse Stacking (CPS) technique. A small-scale prototype will be developed using the custom-built surrogate pump and seed sources for a proof-of-concept demonstration. The demonstration aims to reach the peak power of several tens of GW at a central wavelength of 10 µm. The developed scheme should be scalable to a high peak and average power when using a high-energy, coherently combined Er:ZBLAN fiber pump laser.

CHAPTER 2

Optical Parametric Interactions

Optical frequency downconversion is one of the second-order nonlinear optical wave interaction processes (three-wave interactions) that occurs in noncentrosymmetric crystals. These nonlinear processes were not revealed until the demonstration of the first working laser in the early 1960s, such that sufficient intense optical field was available for the modification of the optical properties of a material system [86]. The first experimentally observed nonlinear optical effect was the second-harmonic generation in a quartz crystal driven by a ruby laser, which is often viewed as the beginning of the new era of nonlinear optics [87]. Other second-order nonlinear processes such as Sum-Frequency Generation (SFG), DFG, and Optical Rectification (OR) have also been investigated and analyzed since, and their technological significance mainly lies in the generation of coherent radiation at new frequencies from existing lasers [88]. Although the third-order nonlinear phenomena such as self-focusing and Self-Phase Modulation (SFM) are also important processes in ultrafast optics, the second-order nonlinear processes present the primary focus of this chapter.

The nonlinear response of a medium is described by the constitutive equations, and the nonlinear modification of the optical fields within the medium is governed by Maxwell's equations [89]. While the full microscopic expression of nonlinear optical susceptibilities via quantum mechanics is available, classical interpretation through an anharmonic oscillator is often sufficient and more illustrative [86, 88–90]. In this

chapter, the classical treatment of parametric interactions is presented with the plane wave assumption in an ideal medium. The phase-matching techniques that enable efficient frequency conversion are described. Other relevant effects, including linear absorption, crystal damage, birefringent walk-off, and group velocity mismatch, are also introduced. The SI system of units is used in the following description.

2.1 Wave propagation in nonlinear media

Derived from Maxwell's equations and constitutive relations assuming homogeneous media with no free charge, no current density, and no macroscopic magnetization, the general form of the wave equation that describes the propagation of the vector electric field wave $\tilde{\boldsymbol{E}}$ in a medium can be written as

$$\nabla^2\tilde{\boldsymbol{E}}(\boldsymbol{r},t)-\frac{1}{c^2}\frac{\partial^2\tilde{\boldsymbol{E}}(\boldsymbol{r},t)}{\partial^2 t}=\mu_0\frac{\partial^2\tilde{\boldsymbol{P}}(\boldsymbol{r},t)}{\partial^2 t}, \tag{2.1}$$

where μ_0 is the permeability of free space and c is the speed of light. The electric polarization in dielectric media $\tilde{\boldsymbol{P}}$ can be expressed as a power series in the electric field:

$$\begin{aligned}
\tilde{\boldsymbol{P}}(\boldsymbol{r},t) &= \tilde{\boldsymbol{P}}^{L}(\boldsymbol{r},t)+\tilde{\boldsymbol{P}}^{NL}(\boldsymbol{r},t)\\
&= \varepsilon_0\int_{-\infty}^{\infty}\boldsymbol{\chi}^{(1)}(\boldsymbol{r}-\boldsymbol{r'},t-t')\cdot\tilde{\boldsymbol{E}}(\boldsymbol{r'},t')d\boldsymbol{r'}dt'\\
&+\varepsilon_0\int_{-\infty}^{\infty}\int_{-\infty}^{\infty}\boldsymbol{\chi}^{(2)}(\boldsymbol{r}-\boldsymbol{r'},t-t';\boldsymbol{r}-\boldsymbol{r''},t-t'')\,:\,\tilde{\boldsymbol{E}}(\boldsymbol{r'},t')\tilde{\boldsymbol{E}}(\boldsymbol{r''},t'')d\boldsymbol{r'}dt'd\boldsymbol{r''}dt''\\
&+\varepsilon_0\int_{-\infty}^{\infty}\int_{-\infty}^{\infty}\int_{-\infty}^{\infty}\boldsymbol{\chi}^{(3)}(\boldsymbol{r}-\boldsymbol{r'},t-t';\boldsymbol{r}-\boldsymbol{r''},t-t'';\boldsymbol{r}-\boldsymbol{r'''},t-t''')\,\vdots\,\tilde{\boldsymbol{E}}(\boldsymbol{r'},t')\\
&\times\tilde{\boldsymbol{E}}(\boldsymbol{r''},t'')\tilde{\boldsymbol{E}}(\boldsymbol{r'''},t''')d\boldsymbol{r'}dt'd\boldsymbol{r''}dt''d\boldsymbol{r'''}dt'''\\
&+\cdots,
\end{aligned} \tag{2.2}$$

where ε_0 is the permittivity of free space, $\boldsymbol{\chi}^{(1)}$ is the linear susceptibility tensor that contributes to the linear polarization $\tilde{\boldsymbol{P}}^L$, and $\boldsymbol{\chi}^{(2)}$ and $\boldsymbol{\chi}^{(3)}$ are the second and third order susceptibility tensors, respectively, that contribute to major part of the nonlinear polarization $\tilde{\boldsymbol{P}}^{NL}$. In nonresonant situations, $|P^{(n+1)}/P^{(n)}| \sim |E/E_{at}|$ generally, where $P^{(n)}$ is the strength of nth order polarization and E_{at} is the characteristic atomic electric field strength of $\sim 5.14 \times 10^{11}$ V/cm. For nonlinear interactions in the nanosecond regime, third and higher order effects can usually be neglected at typical intensities below 1 GW/cm^2 ($E < 8.7 \times 10^7$ V/cm). With further assumptions of local and instantaneous response, Equation (2.2) can be simplified to

$$\tilde{\boldsymbol{P}}(\boldsymbol{r},t) = \varepsilon_0 \boldsymbol{\chi}^{(1)} \cdot \tilde{\boldsymbol{E}}(\boldsymbol{r},t) + \varepsilon_0 \boldsymbol{\chi}^{(2)} : \tilde{\boldsymbol{E}}(\boldsymbol{r},t)\tilde{\boldsymbol{E}}(\boldsymbol{r},t), \tag{2.3}$$

where

$$\boldsymbol{\chi}^{(1)}(\boldsymbol{r}-\boldsymbol{r'},t-t') = \boldsymbol{\chi}^{(1)}\delta(\boldsymbol{r}-\boldsymbol{r'})\delta(t-t'), \tag{2.4a}$$

$$\boldsymbol{\chi}^{(2)}(\boldsymbol{r}-\boldsymbol{r'},t-t';\boldsymbol{r}-\boldsymbol{r''},t-t'') = \boldsymbol{\chi}^{(2)}\delta(\boldsymbol{r}-\boldsymbol{r'})\delta(t-t')\delta(\boldsymbol{r}-\boldsymbol{r''})\delta(t-t''). \tag{2.4b}$$

Therefore, Equation (2.1) can be rewritten as

$$\nabla^2 \tilde{\boldsymbol{E}}(\boldsymbol{r},t) - \frac{n^2}{c^2}\frac{\partial^2 \tilde{\boldsymbol{E}}(\boldsymbol{r},t)}{\partial^2 t} = \mu_0 \frac{\partial^2 \tilde{\boldsymbol{P}}^{(2)}(\boldsymbol{r},t)}{\partial^2 t}, \tag{2.5}$$

where refractive index $n = \sqrt{1+\chi^{(1)}}$ for isotropic media or $n = \sqrt{1+\chi_{ii}^{(1)}}(i = x, y, z)$ as eigen-refractive indices for anisotropic media. The equation is recognized as inhomogeneous wave equation in which the time-varying nonlinear polarization acts as a source term for driving the electromagnetic field.

The general form of the electric field of the optical wave and polarization field of material can be written as

$$\tilde{\boldsymbol{E}}(\boldsymbol{r},t) = \boldsymbol{E}(\boldsymbol{r})e^{-i\omega t} + c.c., \tag{2.6a}$$

$$\tilde{\boldsymbol{P}}^{(2)}(\boldsymbol{r},t) = \boldsymbol{P}^{(2)}(\boldsymbol{r})e^{-i\omega t} + c.c., \tag{2.6b}$$

where ω is the circular frequency of the rapidly oscillating field. $\boldsymbol{E}$ and $\boldsymbol{P}^{(2)}$ are the slowly varying complex field amplitudes, which can be treated as quasi-cw since the electronic and ionic response of the medium is much faster than the rise time of pulses in the nanosecond regime. Inserting them into Equation (2.5) results in the time-independent wave equation:

$$\nabla^2\boldsymbol{E}(\boldsymbol{r}) + \frac{\omega^2 n^2(\omega)}{c^2}\boldsymbol{E}(\boldsymbol{r}) = -\mu_0\omega^2\boldsymbol{P}^{(2)}(\boldsymbol{r}). \tag{2.7}$$

2.2 Coupled wave equations for difference-frequency generation

The total field in dielectric medium can be considered to be a superposition of monochromatic/quasi-monochromatic waves, which can be written as

$$\tilde{\boldsymbol{E}}(\boldsymbol{r},t) = \sum_n \boldsymbol{E}_n(\boldsymbol{r})e^{-i\omega_n t} + c.c., \tag{2.8a}$$

where $\boldsymbol{E}_n$ is the nth component of the wave with a carrier frequency ω_n. The nonlinear polarization can be decomposed in the same way when it presents only a small perturbation to the total polarization. The nonlinear polarization can be written as

$$\tilde{\boldsymbol{P}}^{(2)}(\boldsymbol{r},t) = \sum_n \boldsymbol{P}_n^{(2)}(\boldsymbol{r})e^{-i\omega_n t} + c.c., \tag{2.8b}$$

where $\boldsymbol{P}_n^{(2)}$ is the nth component of the nonlinear polarization oscillating at ω_n. Assuming infinite plane waves propagating collinearly along z-axis in the laboratory coordinate system, Equation (2.7) can be simplified and decomposed into Fourier

components:

$$\frac{d^2\boldsymbol{E}_n(z)}{dz^2} + \frac{\omega_n^2 n^2(\omega_n)}{c^2}\boldsymbol{E}_n(z) = -\mu_0\omega_n^2\boldsymbol{P}_n^{(2)}(z). \tag{2.9}$$

The electric field amplitude can be written as

$$\boldsymbol{E}_n(z) = \hat{e}_n A_n(z) e^{ik_n z} + c.c., \tag{2.10}$$

where $\hat{e}$ is a unit vector of the wave polarization, A is the field amplitude, and k is the wavenumber. Substituting into Equation (2.9) and applying the Slowly-Varying Envelope Approximation (SVEA) ($|d^2A/dz^2| << |k\ dA/dz|$), the wave equations take a form of

$$2ik_n\frac{dA_n}{dz} = -\mu_0\omega_n^2 P_n^{(2)} e^{-ik_n z}. \tag{2.11}$$

In the Fourier domain, the second-order polarization induced in the presence of two interacting fields at ω_l and ω_m can be expressed as

$$\begin{aligned} P^{(2)} &= \varepsilon_0\chi^{(2)}_{eff,SHG}A_l^2 e^{2ik_l z} + c.c. \\ &+ \varepsilon_0\chi^{(2)}_{eff,SHG}A_m^2 e^{2ik_m z} + c.c. \\ &+ 2\varepsilon_0\chi^{(2)}_{eff,SFG}A_l A_m e^{i(k_l+k_m)z} + c.c. \\ &+ 2\varepsilon_0\chi^{(2)}_{eff,DFG}A_l A_m^* e^{i(k_l-k_m)z} + c.c. \\ &+ 2\varepsilon_0\chi^{(2)}_{eff,OR}(A_l A_l^* + A_m A_m^*), \end{aligned} \tag{2.12}$$

where the first two terms represent the Second-Harmonic Generation (SHG), and the subsequent terms represent SFG, DFG, and OR, respectively. The DFG component at frequency $\omega_n = \omega_l - \omega_m$ can then be obtained as

$$P_n^{(2)} = 4\varepsilon_0 d^{(2)}_{eff} A_l A_m^* e^{i(k_l-k_m)z}, \tag{2.13}$$

where the effective value of d-coefficient of DFG is

$$d_{eff}^{(2)} = \frac{1}{2}\,\chi_{eff,DFG}^{(2)} = \frac{1}{2}\,\hat{e}_n \cdot \boldsymbol{\chi}^{(\mathbf{2})}(\omega_n;\omega_l,-\omega_m) : \hat{e}_l\hat{e}_m^*. \tag{2.14}$$

Substituting Equation (2.13) and (2.14) into Equation (2.11), the wave equation can be rewritten as

$$\frac{dA_n}{dz} = i\frac{2\omega_n d_{eff}^{(2)}}{n_n c}A_l A_m^* e^{i\Delta kz}, \tag{2.15}$$

where $\Delta k = k_l - k_m - k_n$ is the wavevector mismatch. This equation is also known as the coupled-amplitude wave equation. The change of the amplitude of ω_n wave depends on the coupling of the ω_l and ω_m waves through the nonlinear polarization with a coupling coefficient of d_{eff}. Analogous coupled wave equations for ω_l and ω_m waves can also be derived. Note that coupling coefficients remain the same as d_{eff} by using full permutation symmetry, assuming the medium is lossless. Usually, the ω_l, ω_m, and ω_n waves in DFG processes are referred to as the pump (ω_p), signal (ω_s), and idler (ω_i) waves. The complete set of coupled wave equations for DFG process is then

$$\frac{dA_s}{dz} = i\frac{2\omega_s d_{eff}}{n_s c}A_p A_i^* e^{i\Delta kz} \tag{2.16a}$$

$$\frac{dA_i}{dz} = i\frac{2\omega_i d_{eff}}{n_i c}A_p A_s^* e^{i\Delta kz} \tag{2.16b}$$

$$\frac{dA_p}{dz} = i\frac{2\omega_p d_{eff}}{n_p c}A_i A_s e^{-i\Delta kz}, \tag{2.16c}$$

where $\Delta k = k_p - k_s - k_i$. The Manley-Rowe relation can be readily derived from the coupled wave equations as

$$\frac{d}{dz}\left(\frac{I_s}{\omega_s}\right) = \frac{d}{dz}\left(\frac{I_i}{\omega_i}\right) = -\frac{d}{dz}\left(\frac{I_p}{\omega_p}\right), \tag{2.17}$$

where $I = 2n\varepsilon_0 cAA^*$ is the wave intensity, and the quantity I/ω is proportional to the photons per unit area per unit time. The relation indicates that the creation rate

of the signal and idler photons is equal to the destruction rate of the pump photons. Alternatively, a pump photon is annihilated and splits into a signal and an idler photon in the DFG processes. This is consistent with quantum-mechanical interpretation.

Assuming negligible pump depletion ($A_p = const$), the analytical solution of coupled wave equations has the form [86]

$$A_s(z) = \left[A_s(0)\left(\cosh\ gz - \frac{i\Delta k}{2g}\sinh\ gz\right) + \frac{\kappa_s}{g}A_i^*(0)\sinh\ gz\right]e^{i\Delta kz/2}, \tag{2.18a}$$

$$A_i(z) = \left[A_i(0)\left(\cosh\ gz - \frac{i\Delta k}{2g}\sinh\ gz\right) + \frac{\kappa_i}{g}A_s^*(0)\sinh\ gz\right]e^{i\Delta kz/2}, \tag{2.18b}$$

where

$$g = [\kappa_s\kappa_i^* - (\Delta k/2)^2]^{1/2}, \tag{2.19a}$$

$$\kappa_{s,i} = i\frac{2\omega_{s,i}d_{eff}}{n_{s,i}c}A_p. \tag{2.19b}$$

In the absence of idler wave ($A_i(0) = 0$), the solution reduces to

$$A_s(z) = A_s(0)\left(\cosh\ gz - \frac{i\Delta k}{2g}\sinh\ gz\right)e^{i\Delta kz/2}, \tag{2.20a}$$

$$A_i(z) = \frac{\kappa_i}{g}A_s^*(0)\sinh\ gz\ e^{i\Delta kz/2}. \tag{2.20b}$$

The axial evolution of $|A_s|$ and $|A_i|$ is shown qualitatively in Figure 2.1 with different degree of wavevector mismatch. In the case of $\Delta k = 0$, both the signal and idler fields experience monotonic increase, and their growth approaches e^{gz} asymptotically for large z. The field growth decreases as Δk increases, and oscillation occurs for $\Delta k > 2\kappa_s\kappa_i^*$. It is clear that phase matching is important for efficient DFG, which is discussed in greater detail in Section 2.3. It is interesting to note that the solution of A_s retains its initial phase in phase-matched interactions, and the signal field exhibits high-fidelity amplification. However, the generated idler wave A_i acquires a phase that depends both on the pump and the signal, such that the idler phase aberration

is unavoidable.

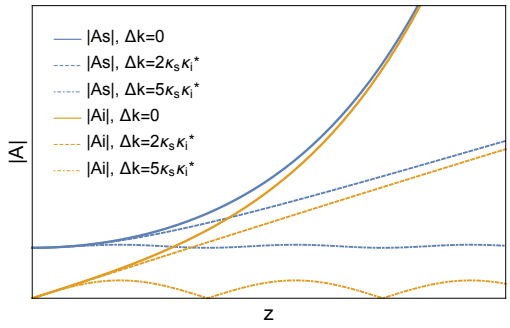

Figure 2.1: $|As|$ and $|Ai|$ as a function of position in a nonlinear medium for DFG with different degrees of phase mismatch Δk.

2.3 Phase matching

The phase mismatch factor $\text{sinc}^2(\Delta kz/2)$ governs the efficiency of the frequency conversion process. As Δkz increases, the efficiency decreases with a certain degree of oscillation. The coherence length is defined as

$$L_{coh} = \frac{\pi}{\Delta k} \tag{2.21}$$

and represents the distance over which the output waves are in phase with the polarization, such that the pump energy can be transferred to the signal and idler. As the waves propagate, the phase relationship changes due to unequal phase velocities. The energy transfer becomes less efficient or even reverses, such that the energy flows back from the signal and idler waves to the pump wave as their relative phase changes. In the absence of phase matching, the energy flows back and forth with a period of $2L_{coh}$. An example of such a case can be seen qualitatively in Figure 2.1. For efficient frequency conversion to occur, it is important that the perfect phase-matching

condition ($\Delta k = 0$) is satisfied. The phase-matching condition can be written as

$$k_p - k_s = k_i. \tag{2.22}$$

Since the photon momentum $p = \hbar k$, Equation (2.22) indicates conservation of photon momentum. By using $k = n\omega/c$, an equivalent form of the above equation can also be expressed as

$$n_p - n_s = (n_i - n_s)\frac{\omega_i}{\omega_p}. \tag{2.23}$$

This condition cannot be satisfied in normally dispersive materials, since $n_p > n_s > n_i$ assuming $\omega_p > \omega_s > \omega_i$. To overcome this limitation, birefringence can be used to compensate for chromatic dispersion. For crystals that do not display birefringence (*i.e.* crystals belong to cubic crystal systems), phase matching cannot be achieved, and the QPM technique can be used instead.

In anisotropic media, there exist two orthogonally, linearly polarized eigenwaves that propagate with their polarization unchanged in a given direction. The two eigenwaves are called ordinary and extraordinary waves and have well-defined eigen-phase-velocities or, equivalently, eigenindices of refraction. In the case of uniaxial crystals (*e.g.* GaSe), the ordinary wave sees a constant index of refraction n_o that is independent of its propagation direction, whereas the normal index $n_e(\theta)$ seen by the extraordinary wave is angularly dependent and is in the range between n_o for $\theta = 0°$ and n_E for $\theta = 90°$, with θ being the angle between the propagation direction and the principal optical axis of the crystal. The principal optical axis is commonly designated as the Z-axis in an orthogonal crystallo-physical frame, which is different than the laboratory frame. The index of the extraordinary wave is

$$\frac{1}{n_e^2(\theta)} = \frac{\cos^2\theta}{n_o^2} + \frac{\sin^2\theta}{n_E^2}. \tag{2.24}$$

For $n_o < n_e$, the crystal is called positive uniaxial. The crystal is negative uniaxial when $n_e < n_o$. In order to achieve phase matching using birefringent crystals, the polarizations of the three waves in DFG, and thus their refractive indices, must be carefully controlled. The pump wave is usually polarized in the direction that gives the smaller one between the two normal indices. The signal and idler waves can be polarized in the same direction with the larger index (*i.e.* oo-e for positive uniaxial or ee-o for negative uniaxial), or polarized orthogonally (*i.e.* eo-o/oe-o for positive uniaxial, eo-e/oe-e for negative uniaxial). The formal case is referred to as type-I phase matching, while the latter case is called type-II phase matching. The phase-matching condition can be implemented by adjusting the orientation angle of the crystal in the Critical Phase-Matching (CPM) method, so that the waves can propagate at a phase-matching angle θ_{pm} in the crystal. Mathematically, θ_{pm} can be determined from Equation (2.22). As an example, the explicit formula for type-II (oe-e) phase matching is [88]

$$\frac{n_{o,p}}{\sqrt{1+(\frac{n_{o,p}^2}{n_{e,p}^2}-1)\sin^2\theta_{pm}}} - \frac{(\lambda_p/\lambda_i)\, n_{o,i}}{\sqrt{1+\left(\frac{n_{o,i}^2}{n_{e,i}^2}-1\right)\sin^2\theta_{pm}}} = (\lambda_p/\lambda_s) n_{o,s}. \tag{2.25}$$

Experimentally, θ_{pm} can be found by maximizing the output signal and idler wave energy. However, in the CPM method, the Poynting walk-off effect is present for extraordinary waves propagating at angle other than 0° and 90°, which limits the conversion efficiency. To circumvent this effect, it is sometimes possible to achieve the phase-matching condition at $\theta = 90°$ by adjusting the temperature of the crystal, in which the amount of birefringence is strongly temperature-dependent. This kind of method is known as Noncritical Phase Matching (NCPM). Due to the narrow temperature bandwidth, the application of NCPM at high average powers is limited.

In the case of biaxial crystals (*e.g.* KTA), the phase-matching direction depends on both the polar angle θ with respect to Z-axis and the azimuthal angle ϕ with respect

to X-axis in the crystallo-physical frame. The two eigen-indices are determined by solving the Fresnel equation:

$$\frac{\sin^2\theta\cos^2\phi}{n^{-2}-n_X^{-2}}+\frac{\sin^2\theta\sin^2\phi}{n^{-2}-n_Y^{-2}}+\frac{\cos^2\theta}{n^{-2}-n_Z^{-2}}=0. \tag{2.26}$$

The phase-matching angle in a biaxial crystal can then be determined accordingly. For example, the phase-matching angle for type-II (eo-o) interaction propagating in the principal plane of XZ can be expressed as [88]

$$\tan^2\theta_{pm}=\frac{1-T}{T-Z}, \tag{2.27}$$

where

$$T=\frac{A^2}{(C-B)^2}, Z=\frac{A^2}{D^2}, \tag{2.28a}$$

$$A=\frac{n_{X,i}}{\lambda_i}, B=\frac{n_{Y,s}}{\lambda_s}, C=\frac{n_{Y,p}}{\lambda_p}, F=\frac{n_{Z,i}}{\lambda_i}. \tag{2.28b}$$

For an isotropic medium, QPM permits net field growth in DFG by changing the sign of nonlinear coefficient once every coherence length, such that the nonlinear polarization wave is shifted by π each coherence length. QPM allows the use of the larger diagonal terms of nonlinear susceptibility and thus presents higher d_{eff} comparing to birefringent phase matching. In practice, QPM is realized by electric field poling of ferroelectric materials (*e.g.* PPLN), whereas in non-ferroelectric materials epitaxial growth of Orientation-Patterned (OP) structures with lithographically controlled patterns can be used (*e.g.* OP-GaAs). The phase-matching condition and the nonlinear coefficient for QPM through the first order grating is

$$k_s+k_i-k_P=\pi/L_c, \tag{2.29a}$$

$$d_Q=(2/\pi)d_{eff}. \tag{2.29b}$$

2.4 Optical parametric amplification and oscillation

Since the signal wave is amplified in the DFG process, this type of nonlinear interaction is also known as OPA. The signal gain can be derived from Equation (2.20) as

$$G = 1 + \kappa_s \kappa_i^* \frac{\sinh^2 gL}{g^2}, \tag{2.30}$$

where L is the crystal length. In the limit of small gain ($\Delta k/2 \gg \sqrt{\kappa_s \kappa_i^*}$), the equation reduces to

$$G = 1 + \kappa_s \kappa_i^* L^2 \mathrm{sinc}^2(\Delta k L/2). \tag{2.31}$$

For perfect phase matching, the small signal gain further simplified as

$$G \simeq \kappa_s \kappa_i^* L^2. \tag{2.32}$$

In the limit of high gain ($\Delta k/2 \ll \sqrt{\kappa_s \kappa_i^*}$), Equation (2.30) reduces to

$$G \simeq \frac{1}{4} e^{2gL}. \tag{2.33}$$

The general solution with pump depletion also exists as a Jacobi elliptic sine function [91, 92], and can be written as

$$G = 1 + \frac{\lambda_p}{\lambda_s} \frac{I_p}{I_s} \left[1 - \mathrm{sn}^2 \left(N_0 gL - \frac{K(N_0)}{\sqrt{N_0}}, N_0 \right) \right] \mathrm{sinc}^2(\Delta k L/2), \tag{2.34}$$

where K is the complete elliptic integral of the first kind, and N_0 takes the form of

$$N_0 = \left(1 + \frac{\lambda_s}{\lambda_p} \frac{I_s}{I_p} \right)^{-1}. \tag{2.35}$$

By providing positive feedback to the signal via a resonator, oscillation occurs when the parametric gain exceeds its optical loss, which is known as the OPO. The OPO produces coherent radiation similar to a laser. Unlike the laser, however, the signal and idler waves are only amplified when traveling in the same direction as the pump wave, while in the reverse direction, the interacting waves are not phase-matched. The OPOs can be classified into two types. If the end mirrors of the OPO are highly reflecting at both signal and idler waves, the OPO is a doubly resonant OPO. If only one of the waves is circulating in the resonator, the device is a singly resonant OPO. The threshold condition for OPO is

$$A_{s,i}(0) = A_{s,i}(L)(1 - l_{s,i}), \tag{2.36}$$

where $l_{s,i}$ are the fractional amplitude loss per pass for signal and idler wave. The fractional loss can be written as

$$l_{s,i} = 1 - R_{s,i}e^{-\alpha_{s,i}L}, \tag{2.37}$$

where $R_{s,i}$ and $\alpha_{s,i}$ are the mirror reflectivities and the linear absorption coefficient of the crystal at the signal and idler frequencies, respectively. The minimum oscillation threshold (when $\Delta k = 0$) of an OPO is

$$\cosh gL = 1 + \frac{l_s l_i}{2 - l_s - l_i}. \tag{2.38}$$

Taking the low-loss limit for both signal and idler wave ($l_{s,i} \ll 1$) for doubly resonant OPO, the threshold condition can be reduced to

$$(gL)^2_{th} = l_s l_i. \tag{2.39}$$

In the case of singly resonant OPO, the condition becomes

$$(gL)_{th}^2 = 2l_s, \tag{2.40}$$

assuming no feedback for the idler ($l_i = 1$). The oscillation threshold for the doubly resonant OPO is smaller than that of the singly resonant OPO by a factor of $\sqrt{2/l_i}$. However, doubly resonant OPOs experience mode hops due to the small cavity length change caused by temperature fluctuation or acoustic vibrations. Singly resonant OPO is generally favored for pulse operation since it exhibits better stability in terms of output power and operating frequency. The threshold pump power for singly resonant OPO is [88]

$$P_{th,p} = \frac{\varepsilon_0 n_s^2 n_p c \lambda_p^2 A_b l_s}{\pi^2 d_{eff}^2 L^2 (1 - \delta^2)}, \tag{2.41}$$

where $0 \leq \delta \leq 1$ is the degeneracy factor, with $\delta = 0$ corresponding to the degenerate point, and A_b is the beam area. The conversion efficiency η can be expressed as [88]

$$\eta = \sin^2 \Gamma, \frac{\sin^2 \Gamma}{\Gamma^2} = \frac{1}{N}, N = \frac{P_p}{P_{th,p}}, \tag{2.42}$$

where P_p is the input pump power.

For a pulsed OPO, the finite rise time exists for amplifying the quantum noise (*i.e.* spontaneous parametric fluorescence) to a steady-state signal power, since multiple round-trips are required to reach the oscillation threshold. A simple expression of such build-up time assuming step input pump is [88]

$$\tau_b = \frac{l_c/c}{l_s(N-1)}, \tag{2.43}$$

where l_c is the cavity length.

2.5 Other design considerations

2.5.1 Absorption

Linear absorption is an important factor that limits the signal gain and the conversion efficiency of parametric processes. This is especially true for parametric oscillation since multiple passes are needed through the crystal. Additionally, TPA presents another detrimental loss mechanism, especially in the MIR regime, since the added energy of two pump photons ($\sim 2.5\ eV$ at 1 µm) can easily exceed the small bandgap of semiconductors that are usually as nonlinear media. Due to the absorption, heating might detune the parametric processes from perfect phase matching and thus limit the operation in conditions of high average power. Absorption can be accounted for as

$$\frac{dI}{dz} = -\alpha I - \beta I^2, \tag{2.44}$$

where α and β are the linear and the TPA absorption coefficients, respectively. The linear absorption effect may include scattering and Fresnel reflection losses. Scattering depends on the crystal quality, while the reflection losses can be alleviated by the use of AR coatings. To reduce the TPA, pump lasers with longer wavelengths are highly valuable.

2.5.2 Laser-induced damage

Since high-intensity laser pulses are used in parametric interactions, laser-induced damage is another limiting factor that constrains the maximum pump intensity applied and thus the available parametric gain. For pulses longer than a few tens of picoseconds, the damage is generally induced by heat deposition, resulting in the melting and boiling of the dielectric material [93]. In this regime, the damage threshold fluence has a $\tau^{1/2}$ dependence on the pulse duration τ. For shorter pulses, the damage mechanism

transitions to an ablative regime dominated by collisional and multiphoton ionization and plasma formation [93, 94]. The damage threshold fluence in this regime continues to decrease with decreasing τ, but departs from the $\tau^{1/2}$ dependence at a slower rate. Such pulse duration dependence of damage threshold can be theoretically modeled in a good quantitative agreement with the experimental results obtained using large bandgap materials with 0.5 and 1 µm lasers [93, 94].

In the short-pulse regime, experimental and theoretical studies of the wavelength dependence of the laser-induced damage threshold have also been performed in the near-ultraviolet to near-infrared spectral range [95] and in the MIR range [96] using materials with a wide range of bandgaps. In the near-ultraviolet to near-infrared region, the damage threshold decreases generally as the laser wavelength/bandgap decreases with no explicit expressions available for the wavelength and bandgap scaling [95]. In the MIR region, the breakdown process is significantly different since the multiphoton ionization is strongly suppressed, and tunnel ionization alone is sufficient to induce breakdown. For wide-bandgap materials, the damage threshold decreases with the increase of laser wavelength, whereas it is independent of wavelength for narrow-bandgap materials [96]. In addition to such systematic parametric studies, damage threshold values have been reported in many experiments under various laser conditions and in various crystals, which are typically very different from each other. Even with similar experimental conditions, the reported values vary significantly. This is largely due to the differences in damage test procedures, damage criteria and detection methods, laser stability, and crystal quality [95].

2.5.3 Poynting walk-off

As discussed in Section 2.3, Poynting walk-off (spatial walk-off) is a limiting effect in CPM. The Poynting vector is defined as

$$\boldsymbol{S} = \boldsymbol{E} \times \boldsymbol{H} \tag{2.45}$$

and represents the directional energy flux of an electromagnetic field. It will drift away from the wave vector $\boldsymbol{k}$ of an extraordinary wave propagating at some angle θ with respect to the optic axis in anisotropic media. The walk-off angle ρ between $\boldsymbol{S}$ and $\boldsymbol{k}$ in a uniaxial crystal can be expressed as

$$\tan\rho = \frac{\sin\theta\cos\theta(n_o^2 - n_E^2)}{n_E^2\cos^2\theta + n_o^2\sin^2\theta}. \tag{2.46}$$

For positive uniaxial crystals, $\boldsymbol{S}$ lies between $\boldsymbol{k}$ and the optical axis. For negative uniaxial crystals, $\boldsymbol{k}$ lies between $\boldsymbol{S}$ and the optical axis. The Poynting walk-off effect reduces spatial overlap of the interacting beams, limits the interaction length of parametric processes, and thus poses constraints on the conversion efficiency. The profile of the product beam may be broadened, and the beam quality may be reduced. The walk-off in CPM becomes less important when using larger diameter beams. In NCPM, where $\theta = 90°$, the walk-off angle vanishes. In QPM, walk-off is eliminated since all interacting waves propagate with the same polarization.

2.5.4 Beam diffraction

Beam diffraction cannot be ignored when beam sizes get smaller. Within the paraxial approximation, a diverging/converging beam can be thought of as a superposition of plane waves traveling with slightly different spatial angular frequencies $\boldsymbol{k}$. The phase-matching condition down breaks when the beam divergence angle is comparable

to or even larger than the angular bandwidth of the parametric processes, such that the conversion efficiency drops as a result. The angular bandwidth can be given as

$$\Delta\theta = \frac{2\Delta k_{1/2}}{\gamma}, \tag{2.47}$$

where γ is the coefficient of first order Taylor expansion of Δk. As an example, γ for type-II phase matching is [88]

$$\gamma_{oe-o} = \pi \frac{n_{e,i}^3}{\lambda_i} \frac{n_{o,i}^2 - n_{e,i}^2}{n_{o,i}^2 n_{e,i}^2} \sin 2\theta_{pm}, \tag{2.48a}$$

$$\gamma_{oe-e} = \pi \left(\frac{n_{e,i}^3}{\lambda_i} \frac{n_{e,i}^2 - n_{o,i}^2}{n_{e,i}^2 n_{o,i}^2} - \frac{n_{e,p}^3}{\lambda_p} \frac{n_{e,p}^2 - n_{o,p}^2}{n_{e,p}^2 n_{o,p}^2} \right) \sin 2\theta_{pm}. \tag{2.48b}$$

2.5.5 Group velocity mismatch

Pulse propagation effects become important in parametric interactions involving ultrashort pulses propagating at different group velocities. Time-dependent coupled wave equations are needed to describe such non-stationary pulse propagation and interactions, as the quasi-cw approximation is no longer appropriate. However, solving such equations analytically is challenging and nontrivial, even with assumptions such as the non-depleted pump. The pulse-splitting length and the phase-matching bandwidth are introduced instead as two important concepts that help to understand the broadband parametric processes [7, 97, 98]. The pulse-splitting length accounts for the temporal walk-off of the signal/idler pulse from the pump pulse and is defined as

$$l_{jp} = \frac{\tau}{\delta_{jp}}, \ j = s, i \tag{2.49}$$

where $\delta_{jp} = 1/v_{g,j} - 1/v_{g,p}$ is the Group-Velocity Mismatch (GVM) between the signal/idler and the pump and $v_g = c/(n - \lambda dn/d\lambda)$ is the group velocity of the interacting waves. In the case of $\delta_{sp}\delta_{ip} > 0$ when the signal/idler pulses walk away

from the pump in the same direction, the pulse-splitting length represents the maximum interaction length, and the conversion efficiency is severely constrained. In the opposite case, when $\delta_{sp}\delta_{ip} < 0$, the interaction can well exceed the pulse-splitting length, and the energy extraction from the pump becomes significantly more efficient.

In the large gain limit, the wave vector mismatch that results in a gain of half of its maximum value (when $\Delta k = 0$) is given by

$$\Delta k_{1/2} \simeq \pm 2(\ln 2)^{1/2}(\sqrt{\kappa_s \kappa_i^*}/L)^{1/2}. \tag{2.50}$$

The phase-matching bandwidth can then be obtained using the first order expansion of the time-dependent phase mismatch as

$$\Delta\nu = \frac{\Delta k_{1/2}}{\pi}\frac{1}{|\delta_{si}|}, \tag{2.51}$$

where $\delta_{si} = 1/v_{g,s} - 1/v_{g,i}$ is the GVM between the signal and the idler. The gain bandwidth is reduced significantly when large GVM exists. It is clear that the broadest gain bandwidth is achieved when signal and idler propagate with matched group velocity, or in a special case when parametric devices operate at degeneracy in type-I phase matching. When $v_{g,s} = v_{g,i}$, Equation (2.51) loses validity and a second-order expansion of Δk involving Group-Velocity Dispersion (GVD) of the signal and idler pulses must be used to determine the gain bandwidth.

It has been shown that GVM can be neglected if the pulse duration is approximately three times the group time difference in the crystal [99]. Generally, GVM effects start to play a role for pulse durations less than ∼1 ps in the MIR region. Higher-order effects such as GVD are not revealed until the pulse duration is less than ∼100 fs [7].

2.5.6 Back conversion

As discussed in Section 2.3, back conversion occurs at L_c when Δk exceeds a certain value. In the case of perfect phase matching, back conversion can also occur when the pump wave is depleted during the parametric interactions. It has been found theoretically that there is a nonlinear phase jump of π associated with the depletion of one interacting wave, such that the energy flow reverses periodically [100]. Back conversion sets an upper limit to the interaction length of the parametric process and thus limits its conversion efficiency. Additionally, it can distort beam quality and spectral gain profile, and ultimately limit the performance of parametric devices. To suppress the backconversion and improve the conversion efficiency, it is helpful for the idler wave to be consumed by absorber [101], coupled out between parametric stages [102], or subjected to cascaded parametric processes [103, 104]. In most situations, it is desirable to choose an optimum crystal length that is equal to the distance in the crystal where the back conversion begins to occur. By careful design, a certain degree of back conversion could be beneficial. It has been shown that a trade-off between spectral bandwidth/beam quality and conversion efficiency can be made to provide an extra control [105, 106].

CHAPTER 3

Modeling of LWIR Optical Parametric Chirped-pulse Amplification

Modeling is the crucial first step in the development and optimization of OPCPA. Generally, modeling involves numerically solving the standard differential coupled wave equations for three-wave mixing via the split-step Fourier approach. To date, only a few simulations have been devoted to answering the question of whether and how the OPCPA technique could be applied to high-peak-power few-cycle pulse generation in the LWIR spectral range [107, 108]. Voronin *et al.* [107] analyzed broadband LWIR OPCPA in ZGP/GaSe/AGSe crystals in various collinear phase-matching geometries. These OPCPA schemes have been designed to be driven at ∼2 µm with energies of up to ∼0.5 J in 100 ps pulse duration. Such high pulse energies are only attainable from nanosecond Q-switched Ho:YLF/Ho:YAG lasers. Simulations show that OPCPA could amplify 80-pJ seed to tens of mJ-level within three stages at relatively low pump intensity of <240 MW/cm^2. Specifically, the simulation shows that up to 113 GW of peak power in 255 fs transform-limited pulse could be achieved at a central wavelength of 10.3 µm from the GaSe (oo-e) OPCPA, whereas the AGSe (oo-e/eo-e) OPCPA could produce a maximum of 77 GW/80 GW in 260 fs transform-limited pulses but at a longer central wavelength of 14.3 µm/16.0 µm. Due to the limited transmission window and narrow gain bandwidth in the LWIR range, ZGP OPCPA is only evaluated at a central wavelength of $\lesssim$8 µm with up to 140 GW in 260 fs transform-limited pulse. Yin

et al. [108] have shown that dual-chirped OPA (a variant of OPCPA pumped by chirped pulses) in ZGP is also a promising approach for amplification in the 4.5–10.5 µm range, supporting TW sub-cycle pulse generation. The proposed scheme is designed to use a 10-ps negatively chirped pump pulse at a central wavelength of 2.4 µm from a multi-pass Cr:ZnSe/ZnS CPA. Compared to OPCPA in ZGP pumped by 2-µm 10-ps Ho:YLF laser under the same conditions (a pump intensity of 20 GW/cm^2, a pump-to-signal ratio of 10^4, a crystal length of ∼0.7 mm, etc.), dual-chirped OPA exhibits extended gain bandwidth at shorter wavelengths and, simultaneously, higher conversion efficiency due to the favorable combination of pump and signal wavelengths and tailored phase matching. Additionally, the gain bandwidth and the conversion efficiency of dual-chirped OPA show weak dependence on the pump-to-signal energy ratio and pump intensity, whereas higher seed energy and pump intensity are more favored in OPCPA.

In this chapter, we systematically consider non-oxide crystals by analyzing different phase-matching geometries, demonstrating the feasibility of the proposed 2.75-µm driven LWIR OPCPA in individual nonlinear materials via numerical simulations based on coupled wave equations.

3.1 Optical parametric chirped-pulse amplification (OPCPA)

Direct amplification of ultrashort pulses is fundamentally limited by nonlinear effects and even catastrophic optical damage governed by the nonlinear component of refractive index n_2 due to the optical Kerr effect. CPA in laser amplifiers has been widely adopted in high-peak-power lasers to circumvent the detrimental effects in the amplification of ultrashort pulses in solid-state media. In CPA, ultrashort seed pulses are chirped and temporally stretched to much longer durations by introducing large,

well-characterized dispersion via a stretcher before passing through amplifiers. The amplified pulses are then compressed via a compressor by applying reverse dispersion that matches the amount introduced by the stretcher and may also compensate for the dispersion introduced by the amplifier. The conjugate pair of stretcher and compressor is usually implemented using diffraction gratings for large ($\sim 10^3$-10^4), high-fidelity stretching ratios in high-peak-power CPA systems. OPCPA applies the CPA scheme to OPAs based on nonlinear parametric processes instead of laser amplifiers, with an intent to effectively transfer the long-pulse pump energy to the stretched signal. This is necessary since OPA is a nearly instantaneous process. Figure 3.1 illustrates the principle of the OPCPA technique. In 1992, the first experimental demonstration of OPCPA was accomplished by Dubietis *et al.* in a BBO crystal with ~0.9 GW of output power [109]. The first TW-level OPCPA was built by Ross *et al.* in 2000 using KH_2PO_4 (KDP) as the output crystal [110]. With the discovery and application of ultra-broadband KD_2PO_4 (DKDP) crystal, TW-level OPCPA was demonstrated in the following decade [111, 112]. Nowadays, PW-class hybrid/all-OPCPA platforms have been constructed worldwide to support diverse applications in the near-infrared region. EW-scale facilities have been proposed that employ coherent pulse combination [3]. Progress is also encouraging in the MIR region, but the LWIR OPCPA sources are still well below the TW peak power level (see Section 1.3).

When compared to CPA based on laser amplifiers, advantages of OPCPA include high single-pass parametric gain, ultrabroad gain bandwidth, reduced nonlinear phase accumulation, weak thermal load, wide spectral tunability, and no amplified spontaneous emission except for much weaker parametric fluorescence. If large-aperture nonlinear media are available, OPCPA allows scaling of ultrashort pulses to a high peak and average power with high prepulse contrast. Due to the nature of the OPA processes, a good spatial and temporal overlap between the pump and the signal are needed for efficient amplification of the signal with high fidelity, in addition

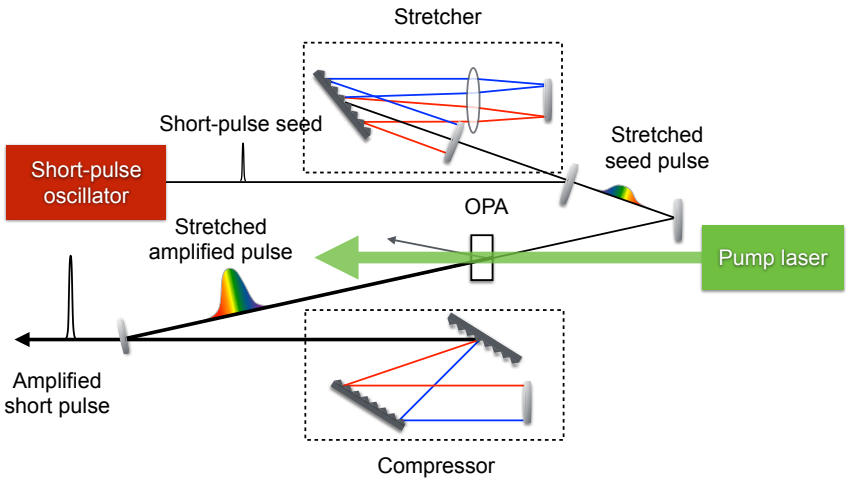

Figure 3.1: Principle of optical parametric chirped-pulse amplification (OPCPA). Adapted from [113].

to the phase-matching requirement. Therefore, OPCPA demands careful analysis of phase-matching conditions, high pump beam quality, and precise timing. The phase-matching geometries will be analyzed in the following sections, while the other considerations will be addressed in the next chapter.

3.2 Nonlinear non-oxide crystal

Nonlinear optical crystal is a key component of optical parametric devices. To meet the desired performance of the LWIR OPCPA, transparency, nonlinearity, damage threshold, phase-matching ability, and other crystal characteristics are important engineering considerations. Traditional oxide crystals are not transparent beyond 4–5 µm due to the onset of multiphoton absorption; therefore, non-oxide materials have to be used for frequency conversion to the LWIR spectral range [7]. As stated in Section 1.3, because of the detrimental TPA, longer wavelength pumping is usually required for non-oxide nonlinear crystals. Generally, since the non-oxide crystals have a smaller bandgap than oxide crystals, most of the non-oxide crystals also have a higher index of refraction and nonlinearity.

For effective comparison of performance between different nonlinear crystals, nonlinear Figure of Merit (FOM), defined as d_{eff}^2/n^3, is commonly adopted instead of simply using d_{eff}. This is because it better represents the parametric gain coefficient ($\sqrt{\kappa_s \kappa_i^*}$) that eventually determines the conversion efficiency of the parametric processes [7]. Figure 3.2 shows the FOM as a function of transparency range for various non-oxide crystals with birefringent/quasi-phase-matching capability [7, 114]. It should be noted that only $\sim 1/3$ of the listed materials are commercially available.

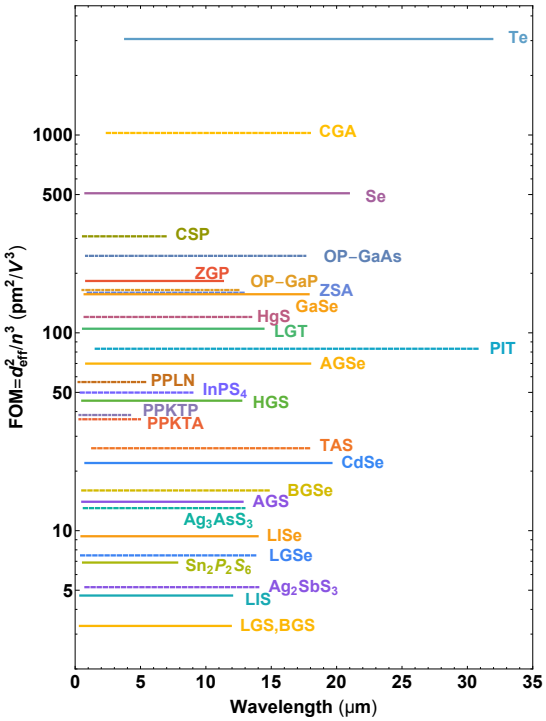

Figure 3.2: FOM of non-oxide nonlinear crystals. Adapted from [7, 114].

Among the most widely used birefringent non-oxide crystals, ZGP has the highest FOM, but also has the upper cutoff wavelength of ~8.5 μm. GaSe has large FOM and is not constrained by transparency, but it is soft and cleaving, and it cannot be polished and coated at arbitrary angles – it is only available as the z-cut. Fortunately, due to its large birefringence, most of the interactions can be realized by using z-cut since the internal phase-matching angles in GaSe are small. AGSe and AGS have modest FOM and are transparent beyond the LWIR window. However, they have notably poor

thermal conductivity and anisotropic thermal expansion. HGS exhibits intermediate FOM and a transparency window comparable to AGSe and AGS; however, it is difficult to grow in large size for energy scaling. The LGS family is newly developed and allows LWIR operation but has the lowest FOM among all of the aforementioned crystals. LGS is valuable because of its compatibility with the 0.8/1-µm pumping. Isotropic semiconductors with cubic structure, such as GaAs and GaP, have very large nonlinear coefficients, wide transparency, good thermal conductivity, high purity, and low loss. These materials cannot be birefringently phase-matched but can be quasi-phase-matched using orientation-patterning techniques. Compared to OP-GaP, OP-GaAs is superior in both FOM and transparency. OP-GaP is not considered for the same reason as ZGP since they have a similar cutoff at longer wavelengths. Therefore, GaSe, AGSe, and OP-GaAs are the three crystals preliminarily selected, primarily based on their FOM>∼50 and extended transparency in the LWIR window. Additionally, since the future high-energy Er:ZBLAN coherently pulse stacked fiber laser operating ∼2.75 µm could provide promising MIR pumping for LWIR OPCPA (see Chapter 4), capabilities that they can be phase-matched for converting the 2.75-µm pump to the LWIR range, and they are free of TPA when the 2.75-µm pump is to be used are also important considerations.

Figure 3.3a compares the absorption coefficient of the three selected crystals in more detail [115]. Among the three, AGSe has the widest transparency from 0.8–18 µm. OP-GaAs and GaSe show comparable transparency window from 2–12 µm; however, higher residual loss of 0.1 cm^{-1} in GaSe exists at the pump wavelength of 2.75 µm. Figure 3.3b summarizes the damage threshold intensity of the three crystals reported in the literature [116–129]. Damage threshold limits the maximum pump intensity that could be applied to the crystal and thus constraints the parametric gain. Since the damage thresholds were measured in diverse experimental conditions (*e.g.*, laser wavelength, pulse duration, crystal quality, *etc.*) and with different test procedures,

the reported values vary significantly. The damage threshold intensities are rescaled based on the $\tau^{-1/2}$ dependence as has been discussed in Section 2.5.2, conservatively assuming a negligible wavelength dependence when extended to the LWIR range. The impacts of other experimental conditions are unclear, and thus they are not considered in the rescaling summarized in Figure 3.3b.

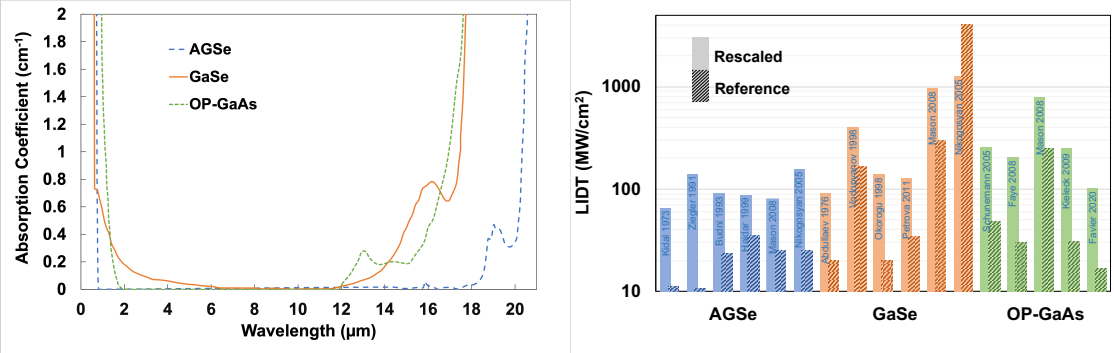

(a) (b)

Figure 3.3: (a) Absorption coefficient [115] and (b) damage threshold [116–129] of AGSe, GaSe and OP-GaAs crystals.

3.3 Phase-matching condition

Different phase-matching geometries for converting the 2.75-μm pump to the LWIR signal at a central wavelength of 10 μm are shown in Figure 3.4 for AGSe, GaSe, and OP-GaAs with crystal length of 5 mm. Two different type-II (eo-e and oo-e) phase-matching geometries can be achieved in AGSe, as shown in Figure 3.4a–3.4b. The oo-e process in AGSe gives broader bandwidth at a phase-matching angle of 41.0°. For GaSe, two type-II (eo-e and oo-e) and a type-I (oe-e) phase-matching angles are available as shown in Figure 3.4c–3.4e. The broadest bandwidth among the three phase-matching conditions in GaSe exists in the eo-e case at a phase-matching angle of 12.8°. Figure 3.4f shows the phase-matching efficiency in OP-GaAs via QPM with the domain period Λ of 133.6 μm. It is clear that the broadest phase-matching among the three selected crystals is available from OP-GaAs pumped at 2.75 μm.

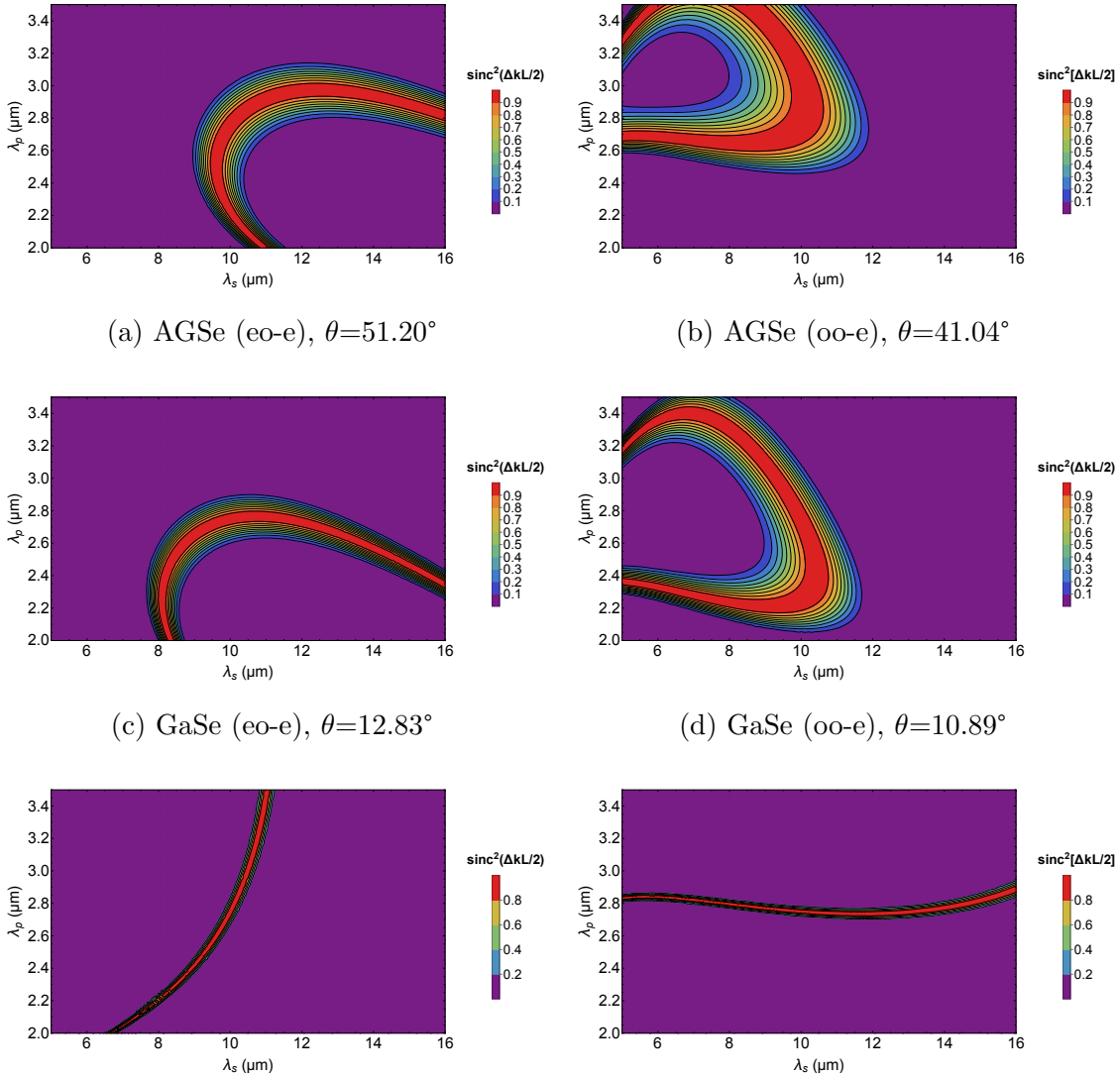

(a) AGSe (eo-e), θ=51.20°

(b) AGSe (oo-e), θ=41.04°

(c) GaSe (eo-e), θ=12.83°

(d) GaSe (oo-e), θ=10.89°

(e) GaSe (oe-e), θ=21.30°

(f) OP-GaAs, Λ=133.56 μm

Figure 3.4: The phase-matching efficiency as a function of pump and signal wavelength for the selected nonlinear crystals with different types of phase-matching configuration at room temperature. The crystal lengths are set to 5 mm.

To account for both the gain and the gain bandwidth of each crystal, a different FOM, defined as $(gL)^2 sinc^2(\Delta kL/2)$, is introduced for comparison among the three selected crystals pumped at their reported damage threshold, which is shown in Figure 3.5a. To give the same gain of 1000 at 10 µm, the crystal length of AGSe, GaSe, and OP-GaAs are set to 26.9 mm, 5 mm, and 6 mm, respectively. As shown in Figure 3.5a, GaSe and OP-GaAs show much broader gain bandwidth, whereas AGSe does not have a broad phase-matching ability at 10 µm. This is because AGSe has the lowest nonlinearity and damage threshold, and thus requires a substantially longer crystal for the same gain, which reduces the gain bandwidth accordingly. OP-GaAs exhibits the broadest bandwidth among the three selected crystals and is most suitable for the LWIR OPCPA development. However, OP-GaAs requires more advanced crystal growth techniques, and bulk OP-GaAs is commercially available only from BAE Systems. GaSe is available from multiple vendors such as Eksma Optics, MolTech GmbH, *etc.*, but cannot be easily customized in terms of crystal cut and AR coating.

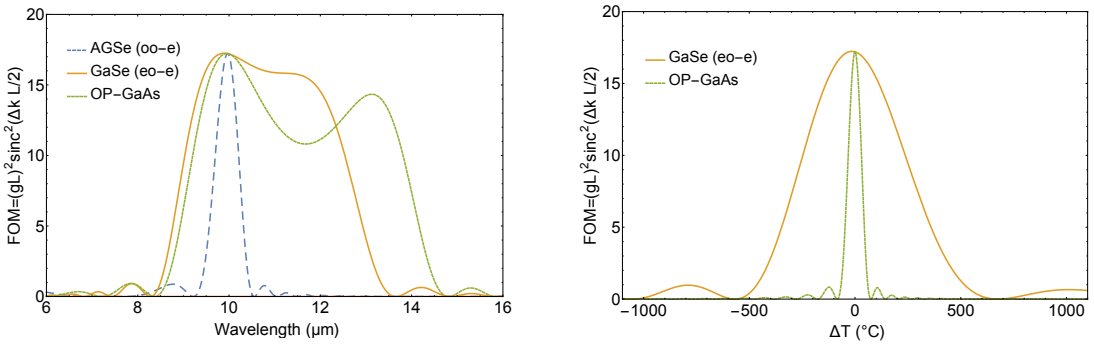

Figure 3.5: (a) FOM of AGS, GaSe and OP-GaAs crystals based on both the gain and the gain bandwidth at room temperature, and (b) temperature dependence of FOM of GaSe and OP-GaAs at a central wavelength of 10 µm. The applied pump intensity is at the damage threshold of each crystal. The crystal length of each crystal is chosen to give a gain of 10^3 at 10 µm.

In addition, temperature detuning ΔT of the FOM of GaSe and OP-GaAs at a central wavelength of 10 µm is also analyzed, as shown in Figure 3.5b, which is due

to temperature-induced phase mismatch as a result of the thermo-optic dispersion of the refractive index. The room temperature corresponds to $\Delta T = 0°$. GaSe shows a temperature bandwidth of 547.1°C, allowing for high-temperature gradient. While the temperature bandwidth of OP-GaAs is much narrower than that of GaSe, it is still considerable at 70.8°C.

3.4 Numerical Model

The model developed for the LWIR OPCPA analysis is based on the standard coupled differential equations for three-wave mixing under the SVEA Equation (2.16). Split-Step Fourier Method (SSFM) is adopted in the simulation. Figure 3.6 shows the schematic of the simulation based on SSFM [130]. The crystal is divided into segments with a length of dz, which possess alternatively only the nonlinear properties or only the linear properties. The nonlinear mixing and dispersion can thus be treated separately in the time and the spectral domains via Fourier/inverse Fourier transforms. This one-dimensional model assumes collinear interactions with infinite plane waves in lossless gain media. The spatial effects (birefringence walk-off and beam diffraction) are not considered in the model, whereas the dispersion and group velocity effects are accounted to all orders. The optical Kerr effect (self-focusing and self-phase modulation) is also not included in the model.

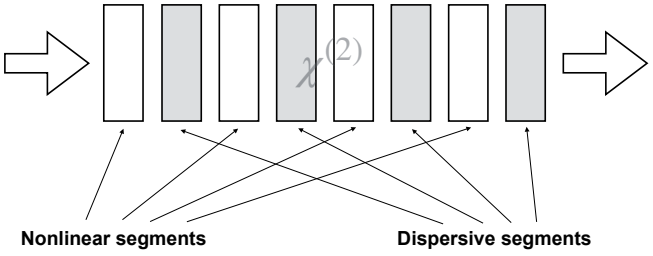

Figure 3.6: Schematic of modeling approach based on the split-step method. Adapted from [130].

Specifically, in the temporal domain where nonlinear mixing is treated, the complex amplitude $A_{i,s,p}(t)$ experiences a change of $dA_{i,s,p}(t)$ over dz, which can be written as

$$dA_s(t) = i\frac{2\omega_s d_{eff}}{n_s c}A_p(t)A_i^*(t)dz, \tag{3.1a}$$

$$dA_i(t) = i\frac{2\omega_i d_{eff}}{n_i c}A_p(t)A_s^*(t)dz, \tag{3.1b}$$

$$dA_p(t) = i\frac{2\omega_p d_{eff}}{n_p c}A_i(t)A_s(t)dz. \tag{3.1c}$$

After each step of numerical integration in the time domain, a spectral phase is applied to the field $A_{i,s,p}(\omega)$ in the spectral domain, where dispersion is introduced. The spectral phase of the fields at each step is

$$A_{i,s,p}(\omega) \rightarrow A_{i,s,p}(\omega)e^{ik_{i,s,p}dz}, \tag{3.2}$$

where

$$A_{i,s,p}(\omega) = \mathcal{F}[A_{i,s,p}(t)]. \tag{3.3}$$

These steps are repeated segment by segment over the entire length of the nonlinear media.

The OPCPA simulation uses broadband linearly chirped seed (signal) at a central wavelength of 10 µm with Full Width at Half Maximum (FWHM) spectral bandwidth of 4 µm. Figure 3.7a shows the input seed spectrum with a Gaussian profile, as well as the quadratic spectral phase applied. The seed is stretched to 1 ns (FWHM) with a chirp of 0.25 ps/nm. Figure 3.7b shows the temporal profile of the corresponding stretched seed pulse. The input pump is defined as monochromatic at 2.75 µm with 10-ns pulse duration. There is no incident idler, which should be centered at a wavelength of 3.79 µm when generated in the mixing process. The applied pump intensity is 1 GW/cm^2, and the pump-to-signal ratio is 10^5.

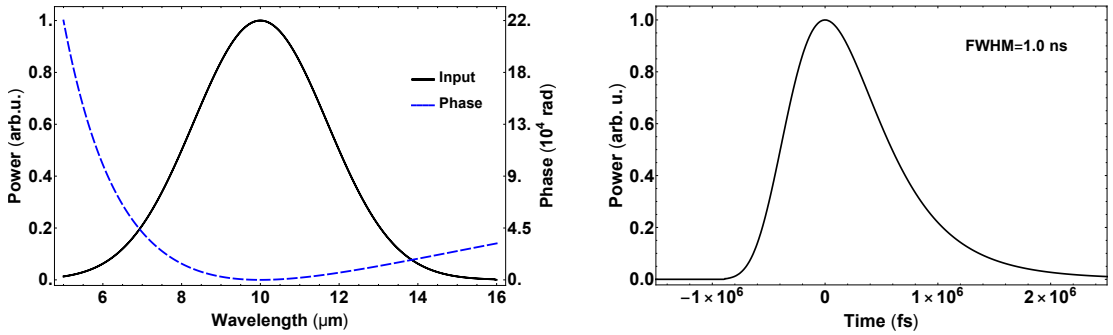

(a) (b)

Figure 3.7: (a) Input signal spectrum and applied quadratic spectrum phase to OPCPA modeling, and (b) its corresponding stretched signal pulse profile.

3.5 Simulation results

The simulation results are presented in terms of spectral bandwidth, spectral phase, transform-limited pulse duration, spectral gain at different seed levels, and crystal temperature. Large spectral bandwidth is an intrinsic characteristic of femtosecond pulse amplification. The spectral phase gained through OPA, although fairly small, is also important since transform-limited pulse can only be obtained if the phase is compensated. The calculation of gain spectra with different seed energies can help determine the optimal crystal length, whereas gain spectra at different crystal temperatures allow the evaluation of the OPCPA performance at high average power. In the following sections, the OPCPA analysis is performed in GaSe and OP-GaAs crystals using CPM and QPM, respectively.

3.5.1 OPCPA in GaSe

For collinear type-II (eo-e) phase-matching in GaSe, the wavenumbers of the signal (e), idler (o), and pump (e) can be expressed as

$$k_s = \frac{2\pi n_e^s(\theta)}{\lambda_s}, \tag{3.4a}$$

$$k_i = 2\pi n_o^i(\frac{1}{\lambda_p} - \frac{1}{\lambda_s}), \tag{3.4b}$$

$$k_p = \frac{2\pi n_e^p(\theta)}{\lambda_p}. \tag{3.4c}$$

The corresponding effective nonlinear coefficient is [131]

$$d_{eff} = d_{22}\cos^2(\theta)\cos(3\phi), \tag{3.5}$$

where $d_{22} = d_{yyy} = 56.9$ pm/V. Figure 3.8a shows the index of refraction of GaSe derived from Sellmeier equations at room temperature [132]. As can be seen in Figure 3.8b, the phase-matching angle for converting the 2.75-µm pump to the LWIR signal at a central wavelength of 10 µm is θ =12.8°. To maximize d_{eff}, the azimuthal angle could be set to ϕ =0°, ±60°, and ±120°, such that $|\cos(3\phi)| = 1$. As a result, d_{eff} of GaSe used in the simulation is 52.4 pm/V and the step dz is set to 1 µm.

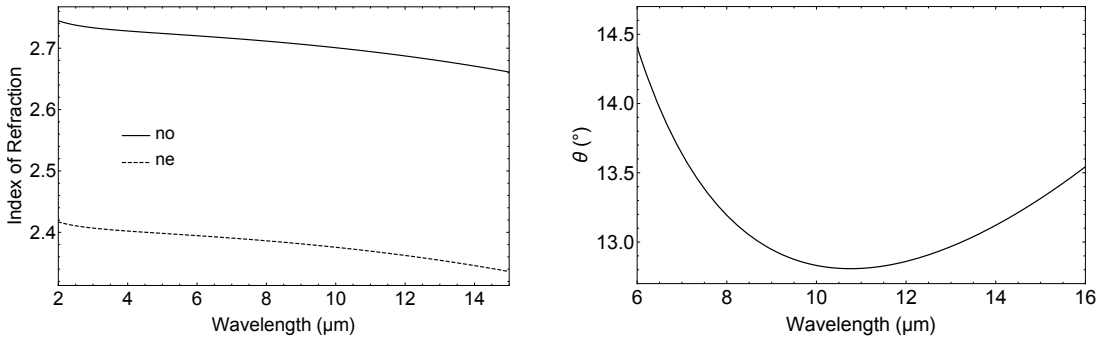

(a) (b)

Figure 3.8: (a) Index of refraction of GaSe at room temperature [132], (b) type-II (eo-e) room-temperature phase-matching curve of GaSe at a pump wavelength of 2.75 µm.

The gain spectra of GaSe OPCPA are simulated for various crystal lengths at a 1 GW/cm^2 pump intensity and 10^5 pump-to-signal ratio. As shown in Figure 3.9a, the spectrum exhibits increased distortion when the crystal length is longer than 6 mm, which is due to the back conversion of the signal to the pump starting from the center wavelength of 10 µm. At a length of 6 mm, a high gain of 3.5×10^4 can be obtained.

However, parametric fluorescence will be significant at such a high gain. Based on empirical experimental results, the gain should be kept below several thousands per amplification stage to avoid strong parametric fluorescence. A 5-mm long GaSe crystal could be used to produce a moderately high gain.

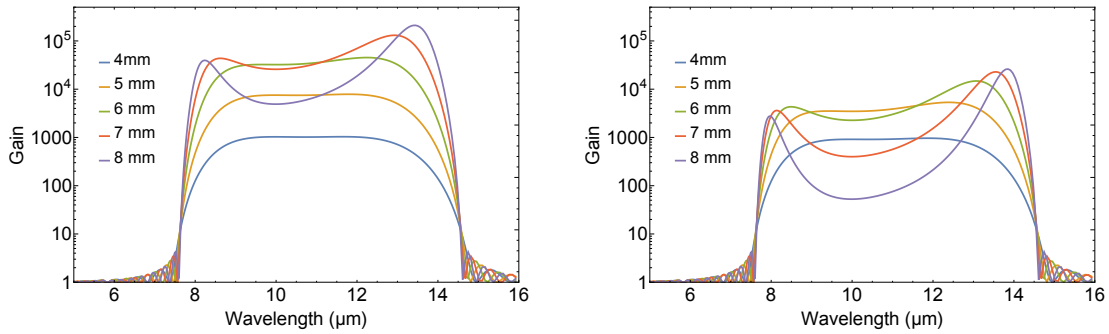

(a) (b)

Figure 3.9: Gain spectra of GaSe OPCPA in collinear geometry with different crystal lengths at room temperature. The pump-to-signal ratio used is (a) 10^5, and (b) 10^4. The pump intensity is kept at 1 GW/cm^2.

If higher seed energy is available, for example, the pump-to-signal ratio is set to 10^4, a length greater than 5 mm is unfavorable since the spectral distortion begins to appear beyond that point, and the gain near the central wavelength starts to decrease due to back conversion. Figure 3.9b shows the gain spectrum of GaSe OPCPA with various crystal lengths at a pump intensity of 1 GW/cm^2 and a pump-to-signal ratio of 10^4. For pump energy on the order of 10 mJ, a pump-to-signal ratio of $10^{4–5}$ corresponds to a seed energy level of 0.1–1 μJ, which is within the targeted range of the LWIR seed source (see Section 5.5).

Figure 3.10a shows output amplified signal spectrum and its spectral phase of the OPCPA in 5-mm GaSe at 1 GW/cm^2 pump intensity and 10^5 pump-to-signal ratio. For comparison, the input signal spectrum is also plotted. The amplified signal spectrum, spanning from 8 μm to 14 μm, is narrowed, but can still support 2-cycle transform-limited pulses (66.7 fs), as can be seen in Figure 3.10b. A small phase variation of $\pi/2$ across the gain spectrum is acquired due to the wave vector

mismatch among different spectral components of the signal, idler, and pump waves. The gain spectrum of 5-mm GaSe OPCPA is shown in linear scale in Figure 3.11a at a 1 GW/cm^2 pump intensity and 10^5 pump-to-signal ratio. The gain profile is centered at ∼11 µm with a FWHM gain bandwidth of 4.5 µm. The gain, in this case, is ∼8000.

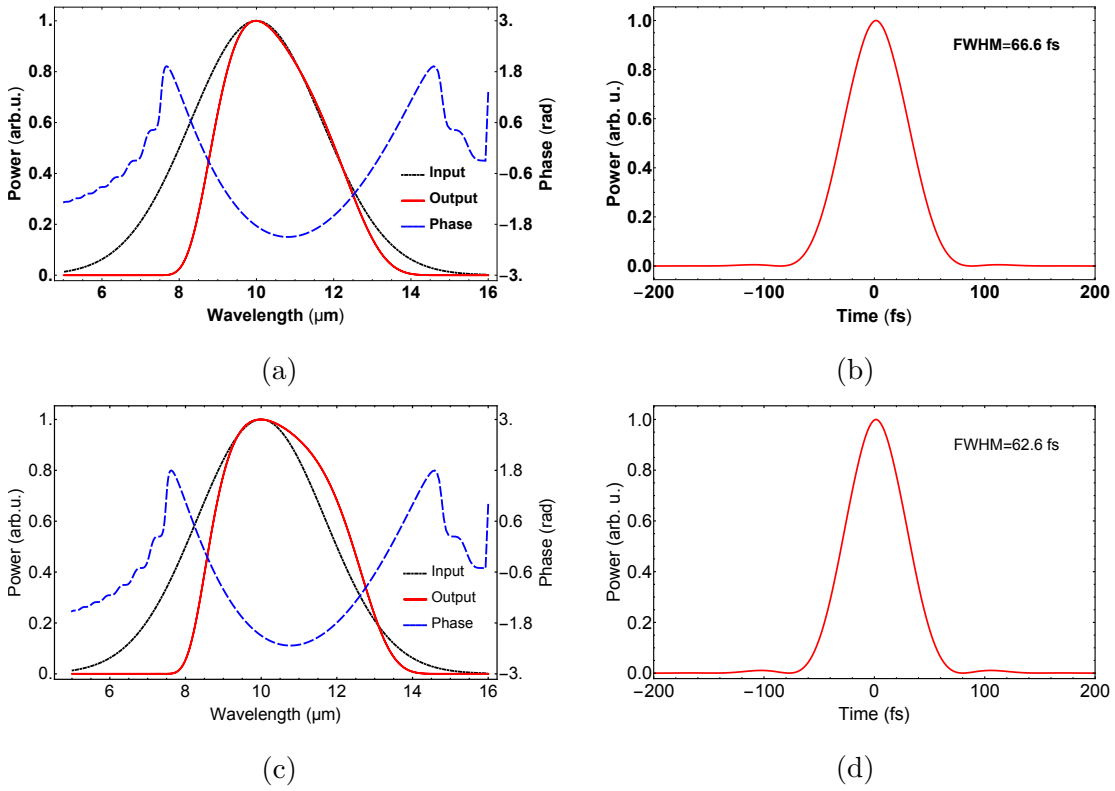

Figure 3.10: (a) and (c) Output signal spectrum and spectral phase of GaSe OPCPA in collinear geometry, (b) and (d) Fourier transform of the spectrum assuming phase has been compensated. The pump-to-signal ratio is set to 10^5 in (a) and (b), and 10^4 in (c) and (d). The crystal length is 5 mm, the pump intensity is 1 GW/cm^2, and the crystal is set to room temperature.

For 10^4 pump-to-signal ratio and 1 GW/cm^2 pump intensity, the amplified signal spectrum and the imparted phase is shown in Figure 3.10c. Compared to the previous case, the output spectrum is broadened by operating in a strong pump depletion region, giving a sub-2-cycle transform-limited pulse of 62.6 fs as shown in Figure 3.10d. In the strong pump depletion region, the output stability of the signal can usually be improved significantly. The corresponding gain spectrum is shown in linear scale in

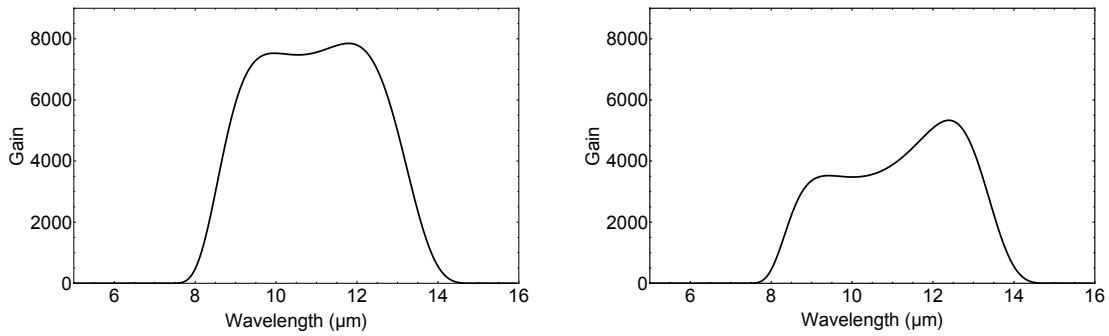

(a) (b)

Figure 3.11: Gain profile of the collinear GaSe OPCPA with pump-to-signal ratio of (a) 10^5 and (b) 10^4. The crystal length is 5 mm, the pump intensity is 1 GW/cm^2, and the crystal temperature is set to room temperature.

Figure 3.11b. The gain profile is still centered at ∼11 μm with a slightly increased FWHM width of 4.8 μm. The gain spectrum does not have a flat profile and has a peak at 12.3 μm. At an order of magnitude higher seed level, the gain can still reach ∼4000.

Temperature detuning from the perfect phase-matching condition prevents the operation of OPCPA at high average power. Figure 3.12 shows the dependence of the index of refraction and phase-matching angle of GaSe (eo-e) on temperature detuning ΔT from room temperature, which is calculated from the temperature-dependent Sellmeier equation [132].

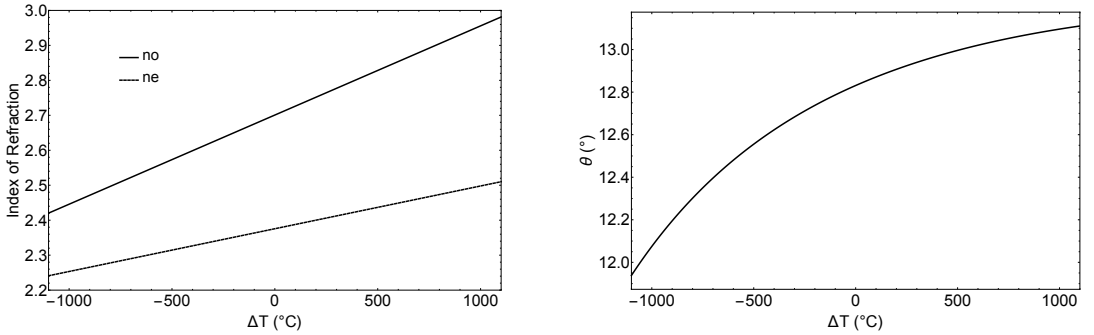

(a) (b)

Figure 3.12: (a) Temperature detuning of index of refraction of GaSe [132], and (b)Phase-matching angle of GaSe (eo-e) vs. temperature detuning.

Figure 3.13 shows the distortion of gain spectra due to the temperature-induced phase mismatch at two different pump-to-signal ratios of 10^{4-5} and at a pump intensity of 1 GW/cm^2. As can be seen in Figure 3.13a, the gain is reduced from ∼8000 to ∼4000 with the increase of temperature detuning from the room temperature to 520°. The gain bandwidth decreases from 4.5 µm to 3.8 µm, whereas the central wavelength of the gain spectra moves to a longer wavelength from 11 µm to 12 µm. A similar trend is observed in Figure 3.13b, which shows the spectra obtained at a higher input signal with ΔT ranging from 0° to 500°. The gain and gain bandwidth are reduced from ∼4000 to ∼3000 and from 4.8 µm to 3.8 µm, respectively, as the ΔT increases from 0° to 500°. The central wavelength of gain moves from ∼11 µm to 12 µm. Generally, at a higher input signal level, the temperature dependence is less pronounced.

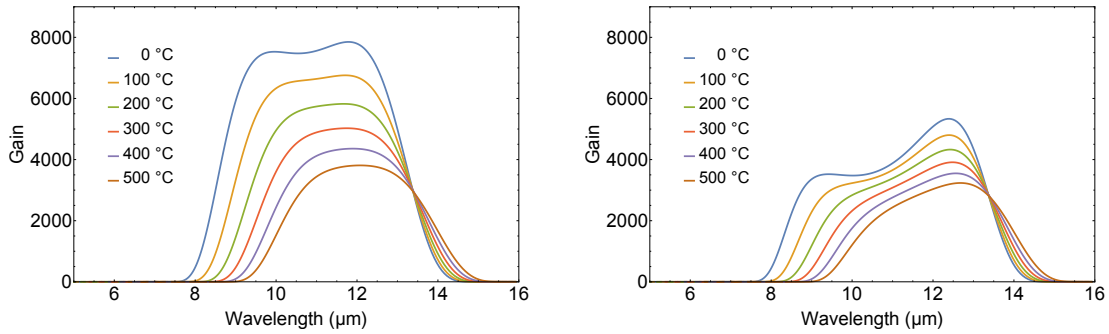

(a) (b)

Figure 3.13: Gain spectra of GaSe OPCPA in collinear geometry with different temperatures detuning from room temperature. The pump-to-signal ratio used is (a) 10^5, and (b) 10^4. The pump intensity is kept at 1 GW/cm^2.

3.5.2 OPCPA in orientation-patterned GaAs

Derived from a Sellmeier equation at room temperature [133], the refractive index of isotropic GaAs is shown in Figure 3.14a. For QPM in OP-GaAs, the length of

optimum period can be calculated as

$$\Lambda = \frac{2\pi}{k_s + k_i - k_p}, \tag{3.6}$$

where

$$k_{s,i,p} = \frac{2\pi n_{s,i,p}}{\lambda_{s,i,p}}. \tag{3.7}$$

Figure 3.14b plots the QPM period as a function of signal wavelength. To obtain QPM at a central wavelength of 10 µm, the optimum period is 133.6 µm. The step dz in the simulation is set to $\Lambda/132$.

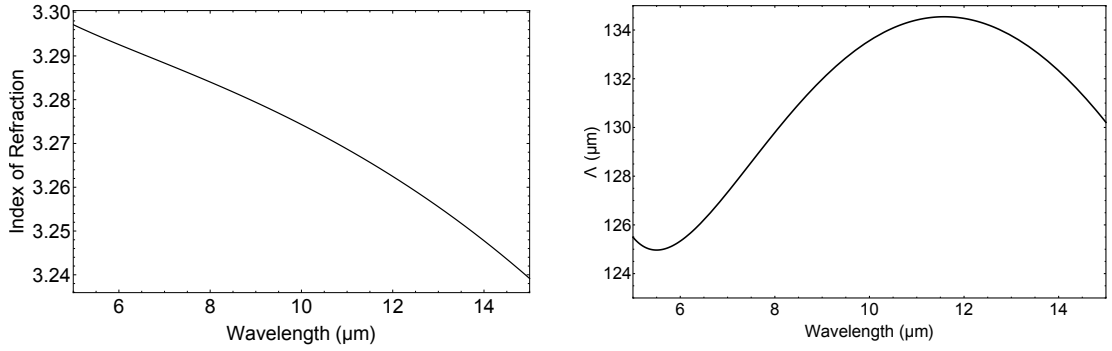

(a) (b)

Figure 3.14: (a) Index of refraction of OP-GaAs at room temperature [133], (b) room-temperature quasi-phase-matching curve of OP-GaAs at a pump wavelength of 2.75 µm.

When the three waves propagate along $\langle 011 \rangle$ with three polarizations kept parallel to $\langle 111 \rangle$ (the direction of the Ga–As bond) [134], the d_{eff} can be maximized:

$$d_{eff} = \frac{2}{\sqrt{3}} d_{14}. \tag{3.8}$$

The value of $|d_{eff}|$ used in the simulation is 85.2 pm [115]. Figure 3.15a shows a periodic alternation of the sign of d_{eff} in the first four periods of OP-GaAs. Figure 3.15b shows the spatial variation of gain in the first four periods of OP-GaAs via QPM. The analytical solutions for QPM and perfect phase matching in OP-GaAs are also shown

in Figure 3.15b for comparison. The numerical modeling result follows the trend of analytical solution for QPM. The increase for QPM is slower than in the hypothetical case of perfect phase matching, which is impossible in isotropic GaAs.

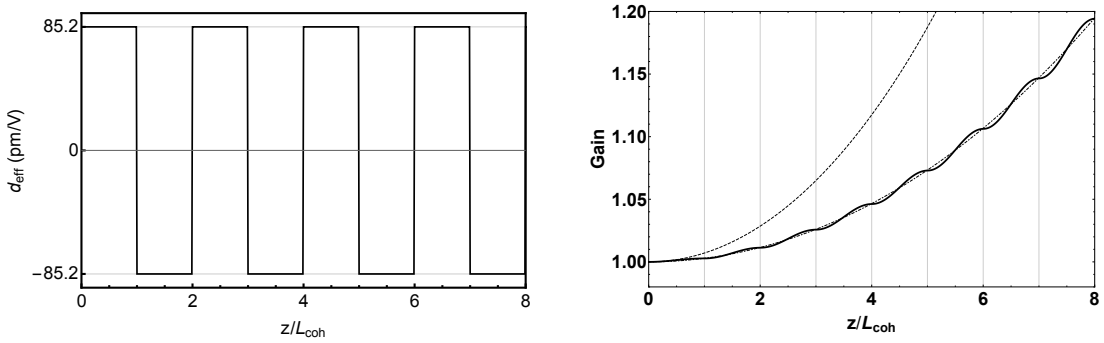

(a) (b)

Figure 3.15: (a) Spatial dependence of d_{eff}, and (b) spatial variation of gain at 10 µm in the first four periods of OP-GaAs at a pump wavelength of 2.75 µm.

Figure 3.16 shows the gain spectra of OPCPA in OP-GaAs with various number of periods and two different pump-to-signal ratio of 10^5 and 10^4. Compared to the GaSe OPCPA, OP-GaAs OPCPA presents a lower gain but wider gain bandwidth at similar crystal lengths. The gain spectra show increasing modification when the crystal length is greater than 61 periods (8.09 mm) and 53 periods (7.08 mm) with a pump-to-signal ratio of 10^5 and 10^4, respectively. However, 45 periods (6.07 mm) are sufficient in both cases to give a gain of a few thousand without unwanted gain distortion. Figure 3.17–3.18 show more detailed information of the two cases with a crystal length of 45 periods (6.07 mm).

The amplified signal spectra and the spectral phases obtained from the 45-period OP-GaAs OPCPA are shown in Figure 3.17a and Figure 3.17c with pump-to-signal ratio of 10^5 and 10^4, respectively. The pump intensity is kept at 1 GW/cm^2. Due to the broader gain bandwidth achieved in the OP-GaAs OPCPA, the amplified signal spectra are less symmetric with longer red tails, and the acquired phase variation of $\pi/2$ spans over a wider wavelength range compared to that obtained in the GaSe

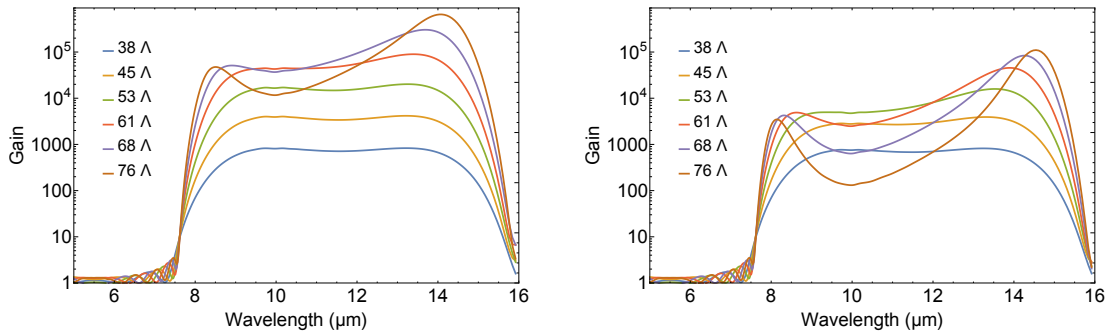

(a) (b)

Figure 3.16: Gain spectra of OP-GaAs OPCPA in collinear geometry with different crystal lengths at room temperature. The pump-to-signal ratio used is (a) 10^5, and (b) 10^4. The pump intensity is kept at 1 GW/cm^2.

OPCPA. No significant differences are observed in the two cases with different pump-to-signal ratios, and accordingly the transform-limited signal pulses obtained in both cases exhibit the same 58.7 fs FWHM width (sub-2-cycles). Figure 3.18 shows the gain spectra in linear plots corresponding to the cases presented in Figure 3.17. The gain spectra are centered at 11.6 μm with a FWHM bandwidth of 5.5 μm. The gain reaches ∼4000 with a relatively flat profile at a pump-to-signal ratio of 10^5, while it is still kept at ∼3000 at a ratio of 10^4, despite the slightly higher peak at ∼13.3 μm.

Calculated from the temperature-dependent Sellmeier equation [133], the dependence of the index of refraction and quasi-phase-matching period of OP-GaAs on temperature detuning from room temperature are shown in Figure 3.19. Based on these curves, the gain spectra at a pump intensity of 1 GW/cm^2 and a pump-to-signal ratio of $10^{4\text{-}5}$ are simulated with ΔT ranging from 0° to 100°, which are shown in Figure 3.20. Despite the asymmetric shape of the gain profile at a higher seed level, the trends of the two cases are similar. The gain decreases significantly (by a factor of ~ 4) over a temperature change of 100°. The gain bandwidth is reduced to ∼2.3 μm, whereas the central wavelength of the gain profile moves slightly from 11.6 μm to 11.8 μm.

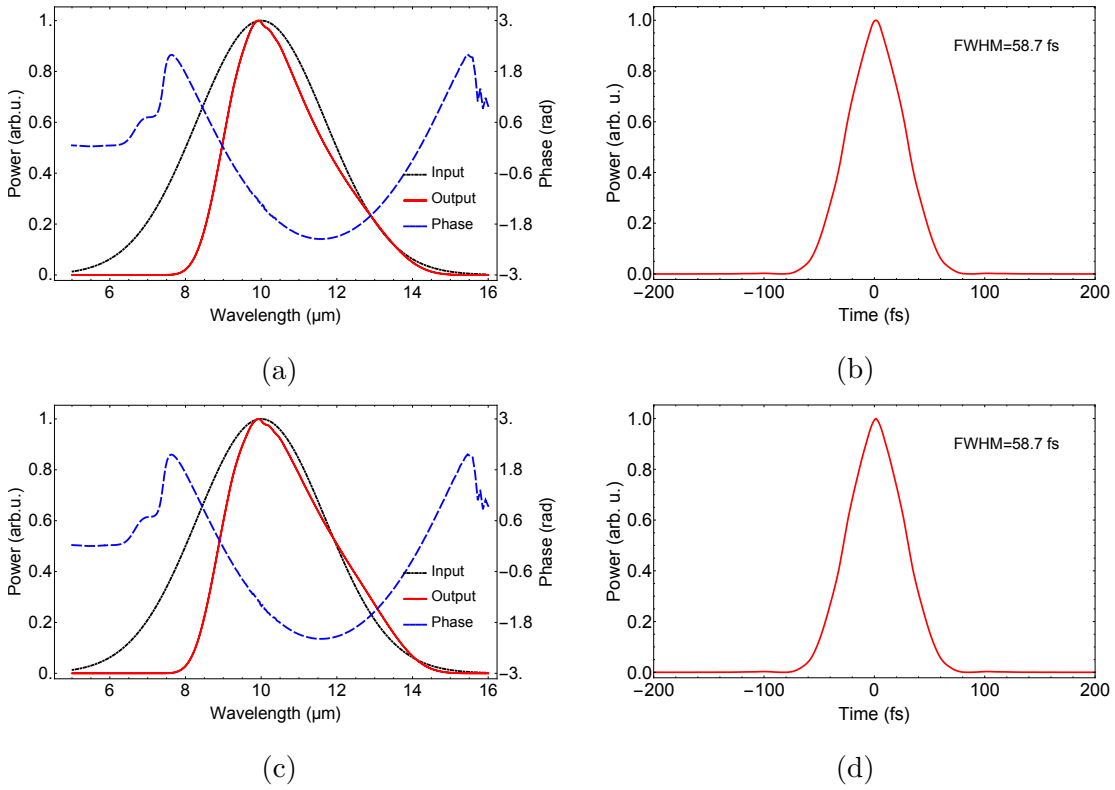

Figure 3.17: (a),(c) Output signal spectrum and spectral phase of OP-GaAs OPCPA in collinear geometry, (b),(d) Fourier transform of the spectrum assuming phase has been compensated. The pump-to-signal ratio is set to be 10^5 in (a),(b), and 10^4 in (c),(d). The crystal length is 6.07 mm (45 domains), the pump intensity is 1 GW/cm^2, and the crystal temperature is set at room temperature.

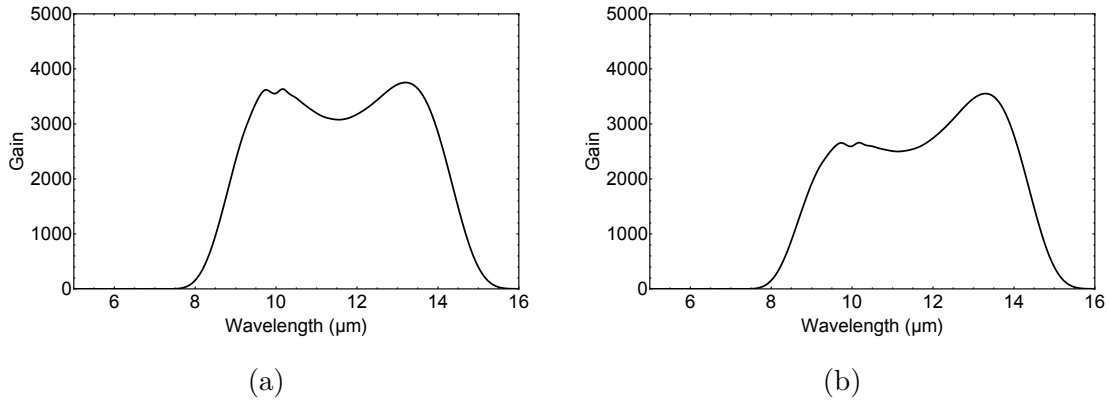

Figure 3.18: Gain profile of the collinear OP-GaAs OPCPA with pump-to-signal ratio of (a) 10^5 and (b) 10^4. The crystal length is 6.07 mm (45 domains), the pump intensity is 1 GW/cm^2, the crystal temperature is set at room temperature.

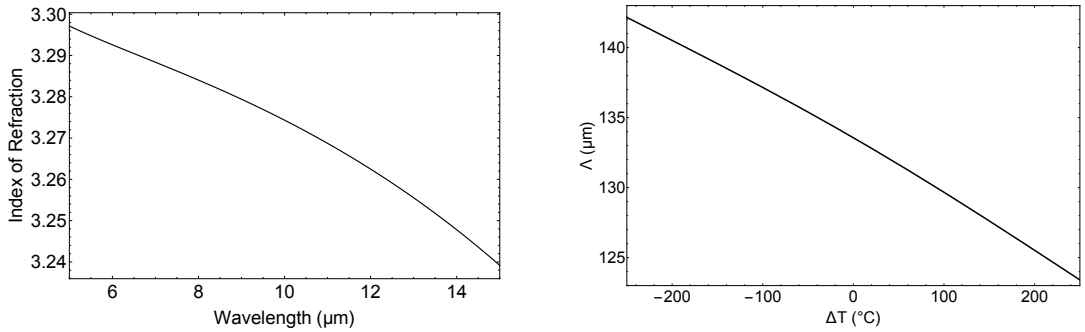

(a) (b)

Figure 3.19: (a) Temperature detuning of the index of refraction of OP-GaAs [133] and (b) quasi-phase-matching period of OP-GaAs vs. temperature detuning.

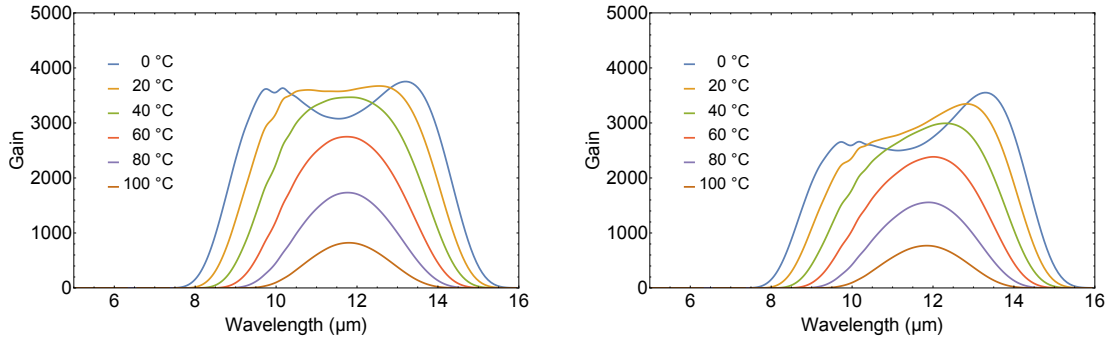

(a) (b)

Figure 3.20: Gain spectra of OP-GaAs OPCPA in collinear geometry with different temperatures detuning from room temperature. The pump-to-signal ratio used is (a) 10^5, and (b) 10^4. The pump intensity is kept at 1 GW/cm^2.

3.6 Conclusion

GaSe and OP-GaAs have been selected for evaluation from various non-oxide nonlinear crystals, and their broadband phase-matching conditions have been determined correspondingly. For converting 2.75-µm pump to signal in the LWIR spectral range with a central wavelength of 10 µm, GaSe uses type-II (eo-e) CPM at 12.8°, whereas OP-GaAs is QPM using a domain period of 133.6-µm. The 2.75-µm driven OPCPA performance in both crystals is analyzed subsequently via numerical simulation. The one-dimensional model developed is based on solving the standard coupled differential equations for three-wave mixing via the split-step Fourier method. As the model assumes collinear interaction with infinite plane waves in lossless gain media, spatial effects such as Poynting walk-off and beam diffraction are not considered in the simulation, and neither is the linear absorption. The optical Kerr effect is also not included in the model. The simulation results show that GaSe OPCPA presents a higher gain but narrower gain/temperature bandwidth when compared to OP-GaAs OPCPA by using the same crystal length. The central wavelength of the gain profile is at 11 µm and 11.6 µm in GaSe and OP-GaAs, respectively. Despite the differences, the OPCPA in both crystals at a pump intensity of 1 GW/cm^2 and a pump-to-signal ratio in the range of $10^{4–5}$ supports 2-cycle pulse amplification at a central wavelength of 10 µm within 5–6 mm long crystals, with a parametric gain of several thousand. For a 10-mJ pump, the predicted output signal energy is on the order of a millijoule, which corresponds to several tens of gigawatts peak power for a 2-cycle pulse duration.

CHAPTER 4

High-energy Nanosecond 2.75-µm Parametric Source

The development of high-energy pump sources in the picosecond to nanosecond regime approaching MIR range benefits the ultrashort LWIR OPCPA implementations based on non-oxide crystals. The past decade has seen steady progress in efficiency, power scaling, and beam quality output from the most developed Er^{3+}-doped fluoride fiber lasers operating in the spectral region of ∼3 µm. A Q-switched diode-pumped Er:ZBLAN fiber laser operating at 2.71 µm has been demonstrated with 0.2-mJ pulse energy in 13.1 ns pulse duration at a 100 Hz repetition rate [135]. The energy scaling potential of Er:ZBLAN fiber amplifiers has been experimentally explored, demonstrating up to 0.67 mJ energy in ∼10 ns pulses from a single 0.8-m long Er:ZBLAN double cladding fiber with 70 µm core diameter [21]. The recently implemented CPS amplification technique using Yb-doped fiber amplifiers demonstrates a potential for generating high-energy sub-nanosecond stacked pulses via cascaded resonant reflecting cavities, alleviating the peak power limitations encountered in the fiber amplifiers [136]. Targeting 1.2–1.5 J pulse energy with 1-ns duration and kHz repetition rate, future high-energy Er:ZBLAN fiber-based CPS systems are promising pump sources for the LWIR OPCPA. In order to allow concurrent development of the LWIR OPCPA and also to support the initial stage of Er:ZBLAN fiber amplifier development, a surrogate parametric source has been developed via OPO/OPA techniques for efficient

generation/amplification of coherent radiations in the vicinity of 2.75 µm. The source is driven by a ubiquitous nanosecond high-energy laser operating at 1 µm. In this chapter, the system design of the surrogate pump is presented. Its complete characterization in the spectral, spatial, and temporal domain are given, as well as the energy output and stability. The majority of the materials contained in this chapter have been published as a journal paper [137].

4.1 Nonlinear oxide crystal and phase-matching condition

Oxide nonlinear crystals could be used to construct a nanosecond 2.75-µm parametric pump source. Oxide crystals are mature in terms of growth technology, such that they exhibit few defects, small residual losses, and high damage threshold [7]. Additionally, it is highly beneficial that oxide crystals are widely available commercially. Figure 4.1 shows the FOM of various standard oxide nonlinear crystals versus transparency range. Among the listed materials, $KNbO_3$, $LiNbO_3$, and $KTiOPO_4$ (KTP) family has extended transparency range and relatively high FOM. More importantly, KTA, as the arsenate isomorph of KTP, shows significantly less pronounced absorption features at ∼2.8 µm, as can be seen in Figure 4.2. This absorption line is caused by hydrogen trapped in the crystal lattice and attached to an oxygen site, forming the OH^- defects that are common in the growth of oxide nonlinear crystals [138].

In addition, KTA has a high damage threshold of 1.2 GW/cm^2 (8 ns) at 1064 nm [139], low-temperature sensitivity, and is non-hygroscopic. It offers phase matching for converting the 1 µm pump photons into ∼3 µm spectral region via birefringence and has a high value of $d\lambda/d\theta$, resulting in narrow free-running linewidth [140].

Specifically, for generating 2.75 µm radiation from the 1 µm pump in a positive biaxial KTA crystal, type-II phase matching (eo-o) in the XZ principal plane has been

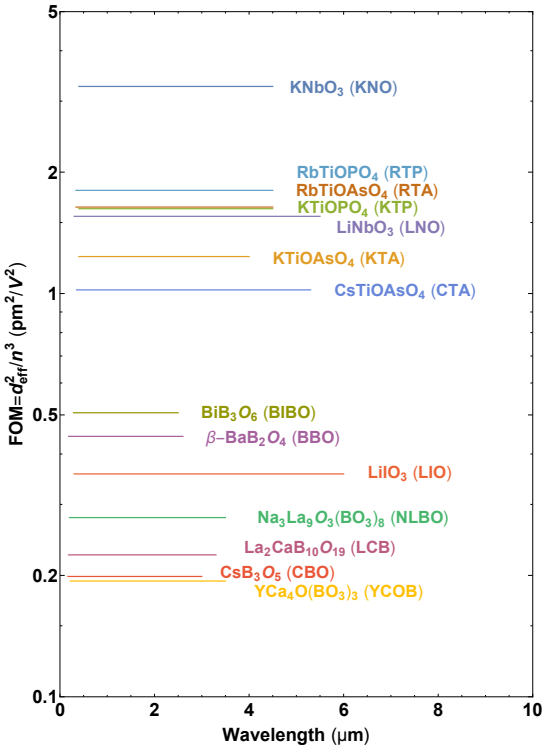

Figure 4.1: Nonlinear FOM of oxide birefringent nonlinear crystal versus transparency range. Adapted from [115].

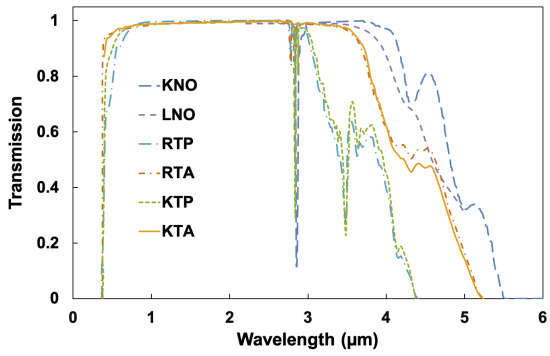

Figure 4.2: Transmission of selected oxide nonlinear crystals [115].

chosen to maximize both d_{eff} and the acceptance angle, and to minimize the walk-off angle. These values are listed in Table 4.1 for different geometries of type-II phase matching in both XZ and YZ planes, which can be obtained conveniently from the SNLO software [115]. Type-I phase matching and phase matching in the XY plane are not achievable. Figure 4.3 shows the index of refraction and the type-II phase matching curve of KTA, calculated from infrared-corrected Sellmeier equations of undoped KTA crystals [141].

Table 4.1: Specifications of type-II phase matching in KTA [115]

Prin. plane	Geom.	d_{eff} (pm/V)	Accp. ang. (mrad · cm)	Walf-off ang. (mrad)
XZ	eo-o	2.66	3.92	38.35
	oe-o	2.09	2.16	44.90
YZ	eo-o	1.57	3.85	39.21
	oe-o	1.16	2.39	40.68

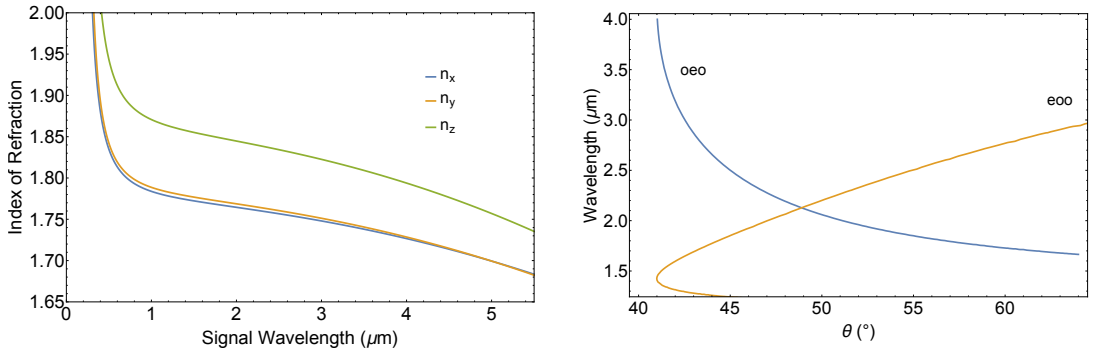

(a) (b)

Figure 4.3: (a) Index of refraction of KTA and (b) type-II phase-matching curve of KTA in XZ plane at a pump wavelength of 1.064 µm.

4.2 Pump laser

The pump laser is a critical component of parametric devices. Due to the instantaneous nature of energy transfer in parametric processes as opposed to energy-storage devices, it is desirable to have a pump with a flat spatiotemporal intensity profile and high

stability, as well as pulse width that is well-matched with the signal. However, it is difficult for a solid-state laser to have all of those favorable characteristics simultaneously. This section presents two modifications made to a simple commercial Nd:YAG laser to partially meet the desired pumping requirements of parametric devices.

The commercial laser is a Spectra-Physics Quanta-Ray flashlamp-pumped Q-switched Nd:YAG laser (PRO-250-10H). The laser operates at a fundamental wavelength of 1.064 µm at 10 Hz and delivers ∼1.4 J per pulse with Root-Mean-Square (RMS) energy stability of ±2.4%. The laser adopts a positive-branch confocal unstable resonator with a Gaussian variable-reflectivity out-coupling mirror and operates with multiple longitudinal modes, producing a highly modulated time profile with a Gaussian envelope. A typical time-integrated near-field spatial beam profile of the laser is shown in Figure 4.4, which is measured by a Charge-Coupled Device (CCD) camera (Mightex SCE-BG04-U). The second-moment width is measured to be 2.11 mm in the horizontal direction and 1.76 mm in the vertical direction. The beam displays spatial modulations and asymmetric hot spots, presumably due to asymmetric side pumping of the Nd:YAG rods. The beam quality parameter (M^2 value) of this laser model is reported to be 2.4 [142] and the beam pointing stability is <50 µrad. The temporal characteristics of the laser are given in Section 4.2.1, and the spatiotemporal dynamics of the laser are presented in Section 4.2.2.

4.2.1 Injection seeding

A smooth temporal profile of the 2.75-µm pump pulse is essential for obtaining a smooth spectral gain profile in OPCPA. This requirement passes on to the pump laser of the 2.75-µm parametric source. However, the Quanta-Ray Nd:YAG laser emits multiple longitudinal modes, resulting in temporal modulation of the generated pulse due to mode competition. Injection seeding technique has been used to produce a

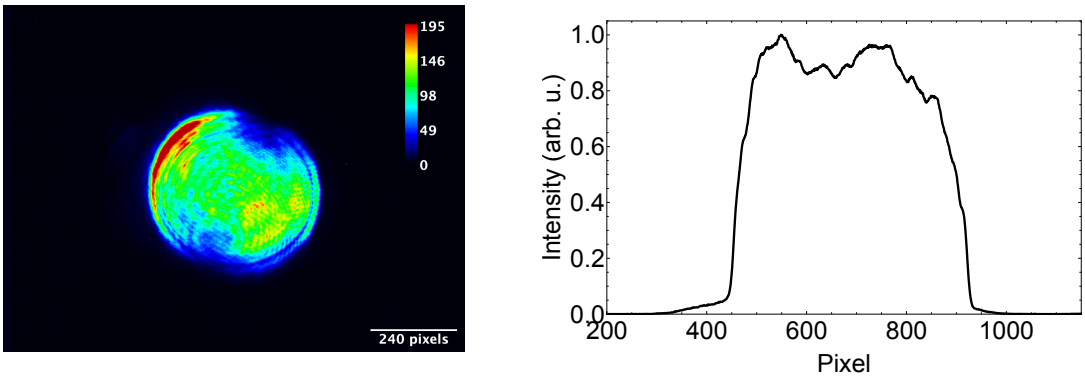

(a) (b)

Figure 4.4: Time-integrated near-field spatial beam profile of the Quanta-Ray Nd:YAG laser.

single longitudinal mode operation of a Q-switched Nd:YAG laser. It is accomplished by injecting a cw single-frequency master laser into a Q-switched slave laser cavity during the pulse buildup time [143]. The resonator mode of that frequency oscillates with much higher power and dominates in the output pulse. As a result, the emission bandwidth is drastically reduced, the pulse profile becomes much smoother, and the buildup time is significantly reduced with reduced timing jitter. For reliable single-frequency operation in a standing-wave resonator, the longitudinal spatial hole burning effect, which leads to strong gain saturation for the lasing resonator mode than for the other modes, should be avoided. The spatial hole burning is usually eliminated by suppressing axial modulation of the optical intensity (standing-wave interference pattern) in a laser cavity via the twisted mode technique [144].

Figure 4.5a shows the CAD design of a homemade injection seeder assembly of the Quanta-Ray laser. The injection seeder (Lightware, 101-04) is based on a diode-laser-pumped Nd:YAG laser with a Monolithic Isolated Single-mode End-pumped Ring (MISER) design [145] and produces a cw single-frequency TEM_{00} mode output. A separate Faraday isolator (Optics For Research, IO-5-YAG) with an isolation of -44.8 dB replaces the one that was originally inside the injection seeder case. The isolator can prevent damage to the master seeder laser and provides a feedback signal

to the photodiode for monitoring the buildup time of the Q-switched pulses. A half-wave plate after the periscope rotates the beam to vertical polarization for seeding via an additional thin-film polarizer (not shown in Figure 4.5a) positioned at the entrance of the oscillator section of the Quanta-Ray laser. The angle bracket integrates these components for mounting inside the Quanta-Ray laser.

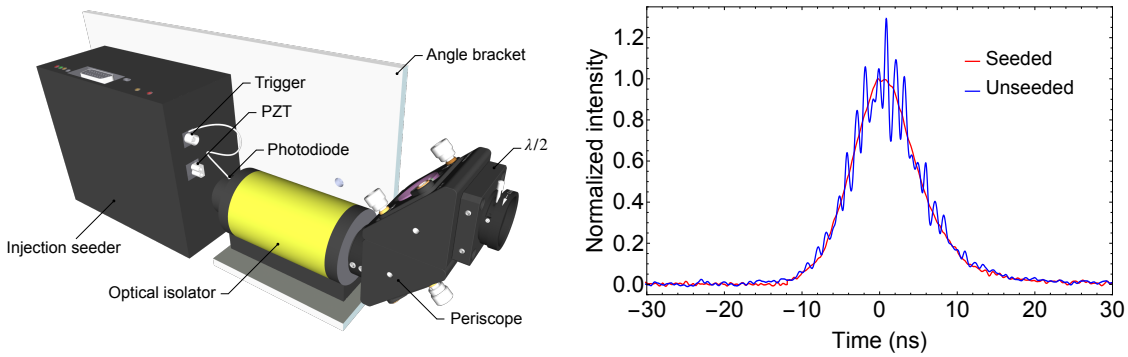

(a) (b)

Figure 4.5: (a) CAD design of the homemade injection seeder assembly for the Quanta-Ray Nd:YAG laser; (b) pulse temporal profile of the Nd:YAG laser with and without injection seeding.

Two quarter-wave plates are used at both ends of the Nd:YAG rod in the oscillator section, such that the two counter-propagating waves in the rod are circularly polarized, possessing a total electric field mode pattern in a shape of twisted ribbon. The end cavity mirror is replaced by a piezoelectric mirror (Spectra-Physics, 0129-0882S) to allow active control and stabilization of the slave cavity length via the feedback loop circuit inside the injection seeder, such that the cavity stays in resonance with the master seeding laser by achieving minimal buildup time. Figure 4.5b shows the temporal pulse profiles of the Nd:YAG laser measured by a 12.5-GHz InGaAs photodetector (EOT, ET-3500) and a 1-GHz oscilloscope (Agilent, Infiniium 54833D). With injection seeding, the strong modulation due to the mode beating is removed, and the pulse has a Gaussian shape with a FWHM width of 9.6 ns. The RMS energy fluctuation of the laser pulse is reduced to $\pm 1.9\%$ after seeding.

Figure 4.6a–4.6b shows the temporal delay and timing jitter of pulses with and without injection seeding, respectively. The temporal delay with respect to the Q-switch trigger is reduced by 18 ns with seeding, and the timing RMS jitter is reduced from 0.54 ns to 0.46 ns with seeding. Both the pulse-width and pulse-amplitude RMS fluctuations, as shown in Figure 4.6c–4.6d, are reduced from $\sim \pm 7\%$ to $\sim \pm 4\%$ in seeded operation.

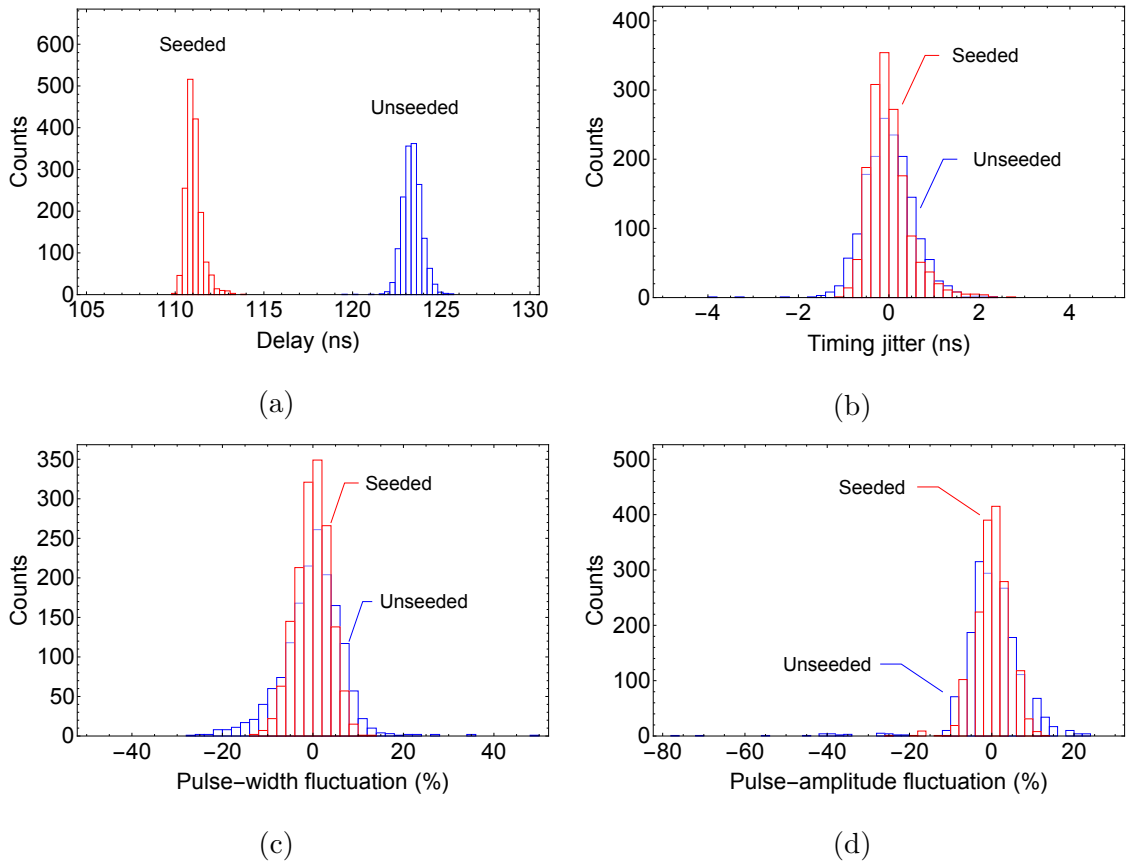

Figure 4.6: (a) Time delay of the generated pulse with respect to the Q-switch trigger, (b) pulse-to-pulse timing jitter, (c) pulse-width fluctuation, and (d) pulse-amplitude fluctuation of the Nd:YAG laser pulses with and without injection seeding.

4.2.2 Pulse slicing

As discussed in Section 2.5.2, the damage threshold fluence scales as $\tau^{1/2}$ in the nanosecond regime and thus, there is a $\tau^{-1/2}$ dependence of damage threshold intensity

on the pulse duration τ. To increase the damage threshold intensity and the parametric gain of the amplifier, the 10-ns pump pulse could be reduced to a shorter duration, which would also match the stretched seed pulse for optimum conversion efficiency. Higher applied pump intensity could, in turn, reduce the length of the amplifier, and thus reduce the spectral phase distortion and increase the gain bandwidth of the OPCPA. Moreover, parametric fluorescence can also be suppressed outside the temporal range in which the pump and the seed overlap, such that a high temporal contrast can be obtained at a reduced pump pulse duration. Limited by the practical grating size and the accuracy of compression, it is not desirable to stretch the seed pulses to arbitrarily long duration for amplification. OPCPA devices usually operate in the picosecond up to the nanosecond time scale. Since a higher stretcher-compressor mismatch can be tolerated in the LWIR spectral range, nanosecond-OPCPA is favored considering more pump energy could be available.

To slice the pulse to 1 ns, a high-speed Pockels cell (Leysop UPC068/2) and thin-film polarizers were adopted for optical gating. The Pockels cell is equipped with two KD_2PO_4 (KD*P) electro-optic crystals and is driven by an HV switch module (BME PCD6i5). The Pockels cell receives two successive HV pulses from the switch module via two cables of different lengths. The nominal rise time of the HV pulse is $\sim$250 ps with RMS timing jitter of $\sim$50 ps. The fall time of the HV pulses is 100 µs. The voltage at the Pockels cell increases to the half-wave voltage when the first pulse arrives, such that the linearly polarized input is rotated by 90° and is allowed to be transmitted through the thin-film polarizer. The voltage is then increased to the full-wave voltage as the second pulse arrives, such that another 90° is rotated, and the polarizer rejects the beam transmission. The optical gate width is fixed by the cable length difference to $\sim$1 ns. The optic axis of the crystals within Pockels cell is aligned by using the Maltese cross after setting up the crossed polarizers. Some pulse leakage is observed after inserting and aligning the Pockels cell, potentially due to the

misalignment of the two KD*P crystals inside it. Figure 4.7a shows a typical sliced pulse profile measured by the 12.5 GHz diode and the 1 GHz oscilloscope, from the most intense part of the seeded Nd:YAG laser pulse. The sliced pulse has a FWHM width of 1.2 ns with a clean rising edge and some residual tail. Figure 4.7b shows the timing RMS jitter of the sliced pump pulses is further reduced to 69 ps. The pulse-width and pulse-amplitude RMS fluctuations of the sliced pulses, as shown in Figure 4.7c–4.7d, are ±1.1% and ±5.0%. The RMS energy stability of the sliced laser pulse was measured to be ±5.2%. The increased pulse amplitude/energy fluctuations are due to the timing jitter between the seeded pump and the gating window of the Pockels cell.

It is known that spatiotemporal dynamics of pulses from a Q-switched Nd:YAG laser with unstable resonator as well as its time-varying diffraction characteristics are significantly different than those with stable resonator whose spatial profile is close to Gaussian and M^2 remains close to unity throughout the pulse duration [146, 147]. With an unstable resonator, the laser starts oscillation on the resonator axis in a small spot and grows rapidly as the pulse builds up. The initial Gaussian profile flattens as the gain on the resonator axis saturates first and the peripheral part of the beam builds up at a later time. At the end of the pulse, the beam profile has a ring shape. The corresponding M^2 value starts close to unity and increases rapidly approaching the pulse tail. It is important that the sliced 1-ns pulse has a relatively uniform beam profile for pumping the parametric devices, and thus the timing of the slicing needs to be chosen carefully.

Such spatiotemporal dynamics have been experimentally analyzed by a combination of pinhole and fast photodetector [146], and by a fast gated camera and Intensified CCD (ICCD) [147]. As the fast Pockels cell has been integrated into the system for pulse slicing, the spatiotemporal evolution of the Quanta-Ray Nd:YAG laser can be conveniently revealed by using a standard CCD camera (Mightex CGE-B013-U) with

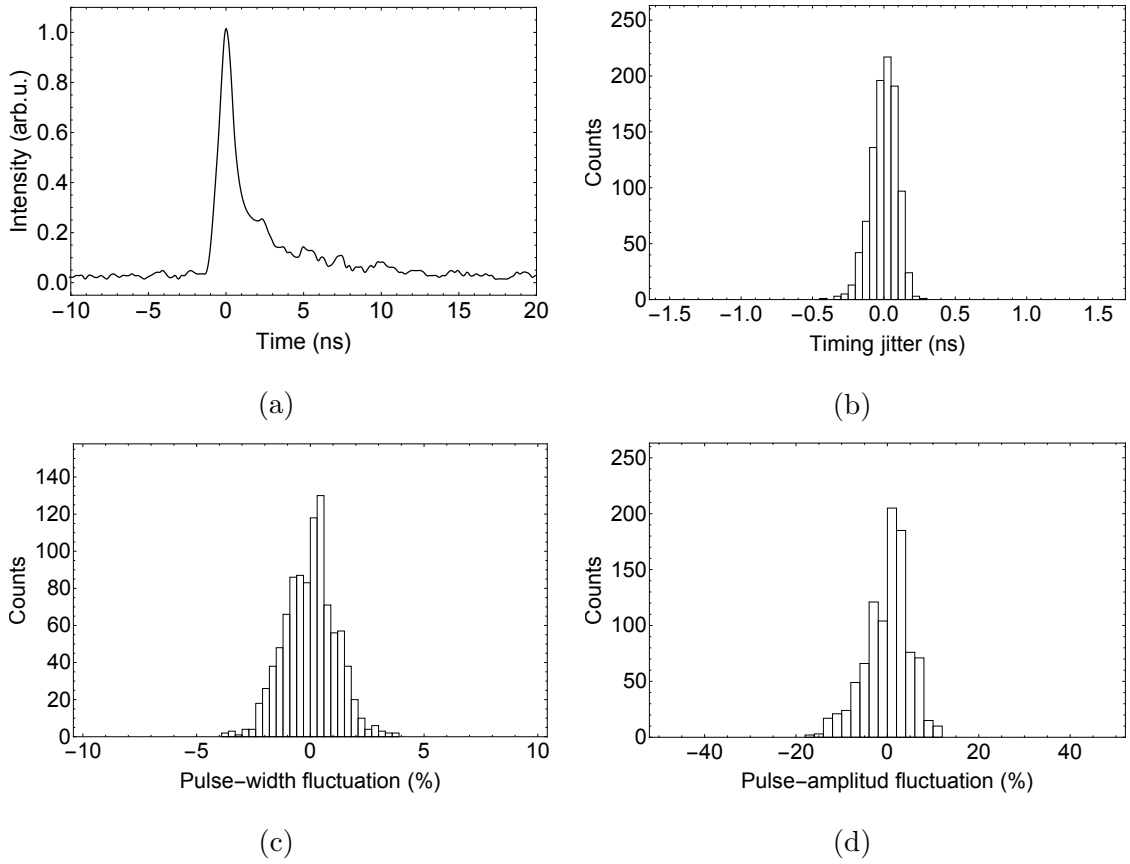

Figure 4.7: (a) Typical temporal profile, (b) pulse to pulse timing jitter, (c) pulse-width fluctuation, and (d) pulse-amplitude fluctuation of the seeded Nd:YAG laser sliced with a fast Pockels cell.

the 1-ns optical gating provided by the Pockels cell. Figure 4.8 shows the spatial profiles of the sliced pump beam at various time delays across the entire temporal pump profile over 30 ns. The measured spatiotemporal evolution of the pump pulse does not follow the pattern described earlier. The center part of the beam builds up from the beginning of the pulse and disappears at the pulse tail. However, the peripheral part of the beam is present in each time slice in Figure 4.8. This is due to the pump pulse leakage from the Pockels cell and polarizers, as the CCD integrates the sliced pump and the pump leakage. Figure 4.9 shows the sliced pump pulse corresponding to selected gate delays in Figure 4.8. Beyond a time delay of 0 ns, the pump leakage forms a decreasing pulse tail attached to the 1-ns sliced pulse. When sliced before the pulse peak, the pump pulse leakage becomes increasingly prominent compared to the sliced pulse with the decrease of the gate delay. All sliced pulses have clean rising edges. The full pump pulse profile is also shown in Figure 4.9 for comparison. At a time delay of 0 ns, the amplitude of the sliced pulse is 85.5% of that of the full profile, and the corresponding energy transmission of the sliced pulse is 30.0% of the full pulse energy. Among all temporal slices, the beam profile sliced at the center of the full pump pulse, as shown in Figure 4.8d, exhibits the most homogeneous spatial distribution for pumping the parametric amplifiers.

4.3 System design

OPOs are devices that are capable of generating widely tunable, coherent radiation. A number of KTA-OPOs pumped by Q-switched 1-µm Nd-doped lasers have been reported to operate at high average power [148–152] and at high pulse energy [153–156]. Singly resonant at either ∼1.5 µm eye-safe signal or ∼3.5 µm MIR idler, these OPOs employ type-II NCPM scheme to take advantage of higher nonlinear coefficient, no walk-off angle, and larger acceptance angle compared to the CPM. For the high-

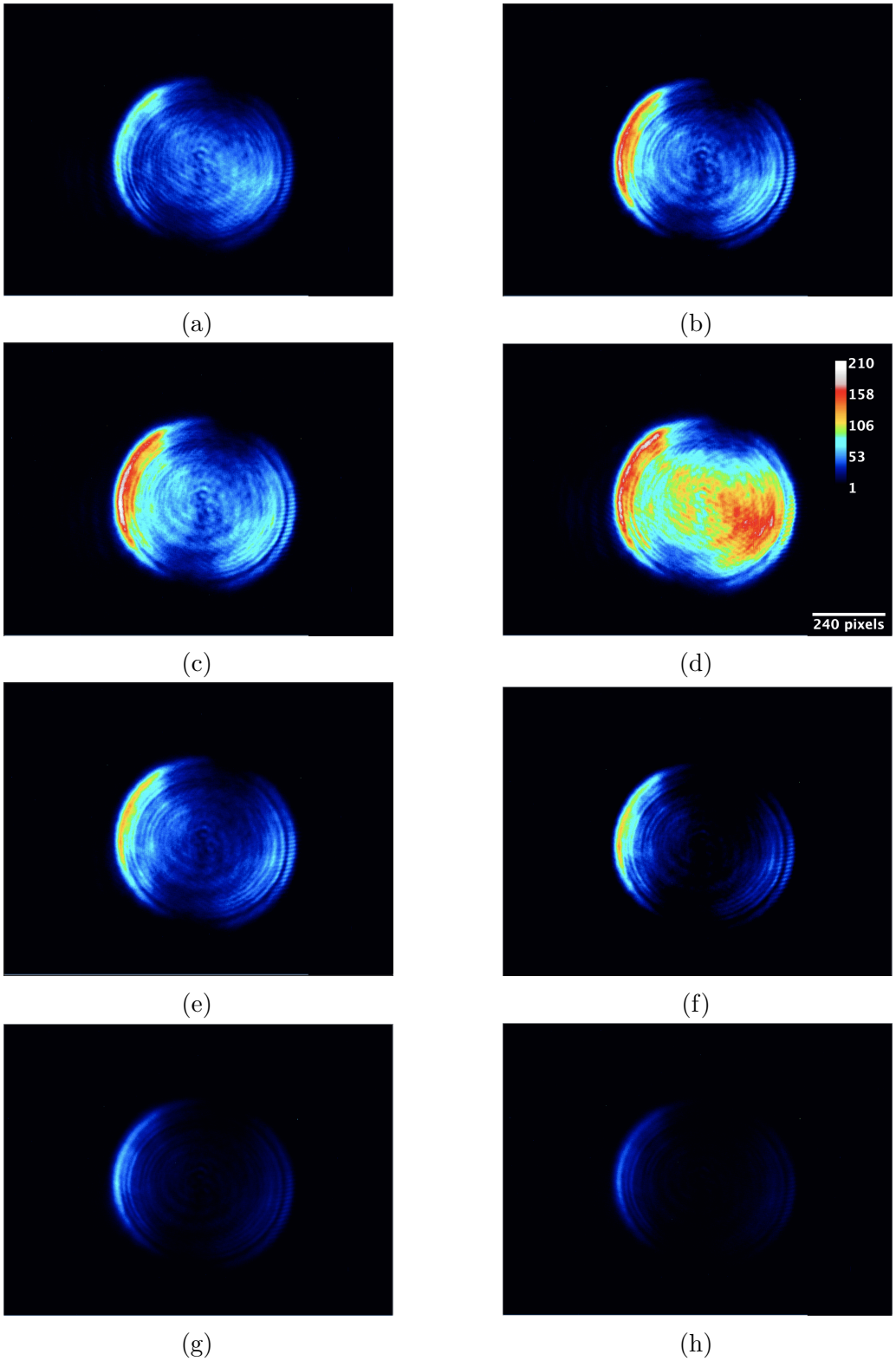

Figure 4.8: Spatio-temporal dynamics of the 1-µm pump pulse measured via pulse slicing at various time delays: (a) −16 ns, (b) −6 ns, (c) −2 ns, (d) 0 ns, (e) 2 ns, (f) 4 ns, (g) 7 ns, (h) 14 ns.

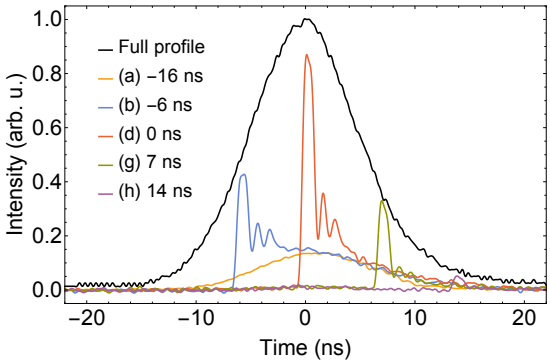

Figure 4.9: Temporal slice of the 1-µm pump pulse at various gate delays.

pulse-energy implementations, the MIR pulse energy (peak power) has reached 10 mJ (5 MW) from an extra-cavity KTA-OPO [154] and 31 mJ (5.3 MW) from an intra-cavity KTA-OPO [155], both at 10 Hz. Intra-cavity pumped self-cascaded NCPM KTA-OPO driven by a diode laser has also been developed to operate at 2.6 µm with up to 445 mW at 60 kHz [104]. However, the tunability of such NCPM designs relies on the tuning of the pump wavelength, which is realized by choosing between different Nd-doped laser crystals. To provide more flexible and wider tunability, CPM has to be adopted in KTA-OPO devices to reach the targeted operating wavelength of ∼2.75 µm. A few high-pulse-energy CPM KTA-OPO implementations have been reported but are not designed to fulfill our specific purpose of OPCPA development, where high-energy, ∼1-ns, ∼2.75 µm pulses are needed with good beam quality. Examples of these schemes include those that operate in the eye-safe spectral region [157, 158], and the one at 2.9 µm [140]. Although the CPM configurations suffer a relatively lower nonlinear coefficient compared to NCPM configurations, the 2.9-µm KTA-OPO device adopting double-pass pumping has achieved up to 17 mJ (>3.4 MW) with a photon conversion efficiency of 32% [140].

It is known that scaling the nanosecond OPO to high energy is challenging if high beam quality is needed along with high efficiency [102,159]. High-energy OPO generally requires a larger beam diameter to avoid optical damage, and a smaller cavity length

for shorter buildup time and thus higher efficiency. As a result, a resonator with a high Fresnel-number ($d^2/\lambda l_c$, where d is the beam diameter) is adopted, which unavoidably leads to poor beam quality due to a large number of supported transverse modes. To improve the output beam quality of high-Fresnel-number OPO, confocal unstable resonators and image-rotating cavities have been proposed and implemented but generally suffer an efficiency penalty and cannot prevent beam distortion induced by severe back conversion [102, 160, 161]. Alternatively, the parametric Master Oscillator Power Amplifier (MOPA) provides a promising approach allowing efficient energy scaling without sacrificing the beam quality [102, 162]. Such MOPA architectures are generally comprised of a low-energy master OPO driven by a small-diameter pump for suppression of higher-order transverse modes, and a power OPA stage driven by a large-diameter pump containing most of its energy and seeded by an expanded signal from the OPO matching the pump beam diameter. The overall energy output and efficiency are dominated by the power OPA stage, whereas higher-order modes tend not to grow with the increase in seed energy when compared to the parametric fluorescence noise. By splitting into multiple stages with idler coupled out instead of implementing a single high-energy OPO, the back conversion can be suppressed/controlled more easily, and high gain can be obtained simultaneously. Delayed pumping of the OPA stages is adopted to account for the buildup time of the OPO stage for higher efficiency.

The experimental setup of the KTA-based MOPA system is schematically shown in Figure 4.10a. As discussed in Section 4.2, the pump (not shown in Figure 4.10) of the MOPA is the Spectra-Physics Q-switched Nd:YAG laser, which is seeded by a Lightwave injection seeder (101-04) to provide single-longitudinal-mode operation. The pump laser is capable of delivering 1.064-μm, 10-ns pulses with an energy of up to 1.4 J at a repetition rate of 10 Hz. The RMS energy stability and pulse-to-pulse timing jitter are 2.4% and 0.46 ns, respectively. The master oscillator (OPO) employs a 5 mm×5 mm×20 mm KTA crystal (KTA1) from Castech Inc. with XZ cut at

$\theta \approx 59^\circ$ for type-II (eo-o) phase matching. The crystal surfaces are AR coated for the interaction waves with an estimated $\sim$500-MW/cm^2 damage threshold of the AR coatings provided by the vendor. A 2° wedge is used to prevent parasitic intra-crystal oscillation. The OPO uses a simple parallel plane cavity with cavity mirrors (M1) that are high-transmission coated at the fundamental wavelength of 1.064 µm and idler wavelength of $\sim$1.74 µm, and high-reflection coated at a signal wavelength of $\sim$2.75 µm. The OPO thus singly resonates at the signal wavelength for a better spatial and spectral performance of the signal beam, while also generating and amplifying the idler in the parametric amplification process. The cavity length of the OPO is approximately 24 mm. The pump beam is relay imaged from the laser to the OPO crystal by using a vacuum telescope, which also collimates and demagnifies the beam to minimize the angular dephasing and to comply with the limited crystal aperture. Since the signal is mostly confined in the cavity without a customized output coupler, the idler beam is extracted after the OPO stage and is combined with the imaged, demagnified, and collimated pump collinearly in a 5 mm×5 mm×25 mm KTA crystal (KTA2) with the same cut as KTA1 in the next OPA stage by using short-pass dichroic mirrors (M2) with a 1.5 µm cutoff wavelength. The pulse that pumps this stage can be sliced to $\sim$1 ns using the fast Pockels cell, such that the converted signal has a similar pulse duration. The signal beam is then extracted by dichroic mirrors identical to M1 used in the OPO cavity, and is expanded and collimated by a Galilean telescope (L1, L2) by a factor of 3 for combination with the pump in the final power OPA stage. This stage uses a KTA crystal (KTA3) with a dimension of 10 mm×10 mm×25 mm using the same cut as KTA1. The pump beam to this final stage is also relay imaged from the laser, but with a smaller magnification of 1.5 compared to that of 5 of the other stages that has a pump beam size of $\sim$1.9 mm in the crystals. Evacuated tubes are used inside the pump telescopes to prevent air breakdown at the focus. The pump intensity applied to the OPA crystals is kept to $\lesssim$350 MW/cm^2 (10 ns) to avoid

potential damage to the AR coatings. The amplified signal beam is stripped from the pump and the idler via several reflections from M1-type dichroic mirrors for further characterization. The polarization of the signal is in the horizontal direction, whereas the pump and the idler are polarized vertically. A photograph of the experimental setup of the MOPA system is shown in Figure 4.10b.

A Czerny-Turner monochromator (Horiba iHR550) equipped with 300 mm^{-1} ruled grating (Horriba 510-23), an InSb detector (Hamamatsu P4631-03) and a boxcar averager (Stanford Research System SR250), an InSb camera (Xenics Onca-MWIR-InSb-320), a HgCdTe (MCT) detector (VIGO AIP INTIR), energy sensors (Coherent J-10MB-LE, J-25MB-LE), and a scanning knife-edge are used for diagnostics. The beam quality measurement is performed in accordance with the ISO standard 11146 [163].

4.4 Experimental results

4.4.1 10-ns operation

The KTA-OPO stage was tuned to singly oscillate at a signal wavelength of 2726 nm, which is around the peak wavelength of the amplified spontaneous emission bandwidth of Er:ZBLAN. The idler beam is used to seed the next preamplification stage for conversion and amplification of the signal beam, such that sufficient seed energy can be provided to saturate the power OPA stage. The FWHM linewidth of the signal was measured to be 2.8 nm using a scanning monochromator. The individual longitudinal modes cannot be resolved by the monochromator with a resolution of 0.3 nm since the spacing between adjacent longitudinal modes of the OPO is only 3.4 GHz. The idler wavelength is centered at 1745 nm with a FWHM linewidth of 1.7 nm. Figure 4.11 shows the typical output spectra of the idler and the signal obtained from the OPO stage and the first OPA stage, respectively.

Figure 4.12a shows the output idler energy from the OPO as a function of the

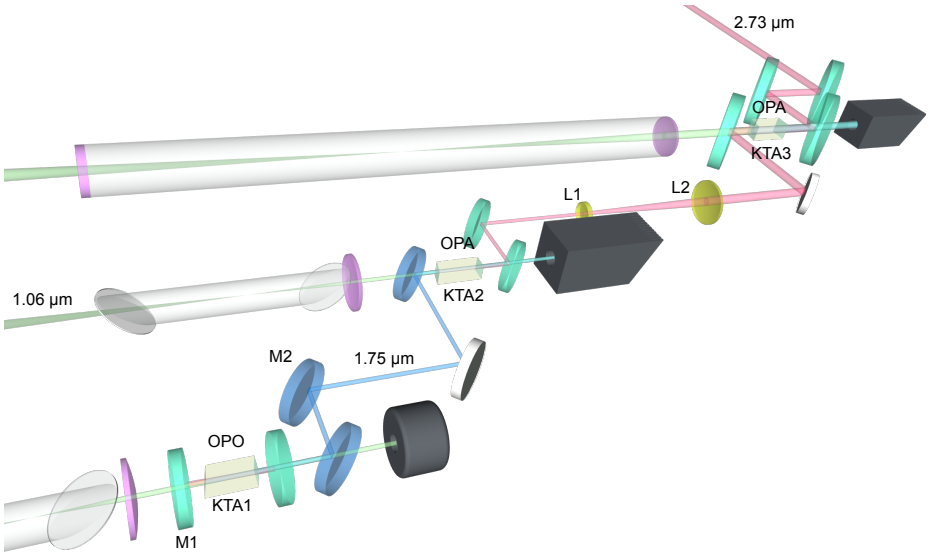

(a)

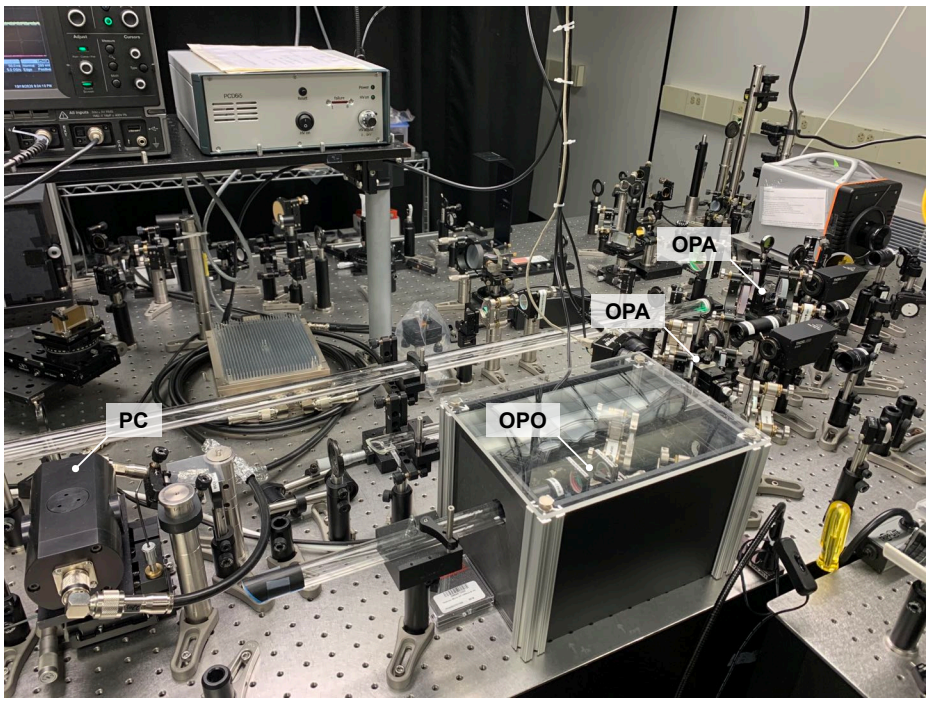

(b)

Figure 4.10: (a) Schematic diagram of KTA MOPA system driven by a 1.064 μm Nd:YAG laser; (b) photograph of the experimental setup of KTA MOPA system.

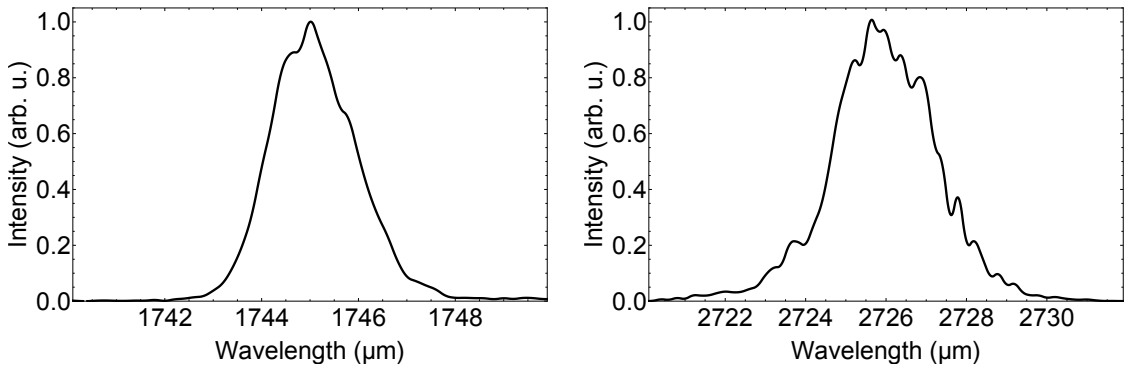

(a) (b)

Figure 4.11: Output spectra of (a) the idler from the OPO stage, and (b) the signal from the first OPA stage.

pump energy. The OPO starts oscillation at threshold pump fluence of ∼1 J/cm^2. The maximum photon conversion efficiency of the idler is limited to 25.3% at 1.7 times the pump energy at OPO threshold to comply with the limited damage threshold of the dichroic mirrors used in the construction of the OPO. The corresponding maximum idler pulse energy is 7.59 mJ with ±2.34% RMS fluctuation over 1800 pulses. The OPO has not reached saturation at this pump level, and thus the back conversion is expected to be insignificant. It has been shown that the absorption coefficient at 2726 nm is ∼0.00047 cm^{-1} in air with relatively high humidity of 60% [39]. The energy loss due to air absorption in the OPO cavity is estimated to be no more than 0.23% in our laboratory environment with typically much lower humidity levels. Numerical model of unseeded OPO provided by SNLO [115] has been used to simulate the KTA OPO assuming super-Gaussian spatial profile and Gaussian temporal profile. As shown in Figure 4.12a, the model cannot fully reproduce the experiment since the OPO develops from quantum noise and operates with multiple longitudinal modes, which are not included in the model [164]. Since the idler propagates freely from the OPO to the first OPA stage over ∼450 mm (∼0.75 Rayleigh range) in air, the idler beam diameter evolves to be somewhat greater than that of the pump beam in this stage. This expansion helps to provide a better beam overlap in the first OPA crystal,

where the beam size is relatively small. The larger seed beam also acts as a spatial filter since only the central part of the idler overlaps with the pump, such that the converted signal beam has a better beam quality [102]. An estimation of ∼63% of the signal energy is taken as the seed for the first OPA. This OPA stage amplifies the idler to a maximum of 11.08 mJ with ±6.2% RMS stability and converts the signal to a maximum of 3.8 mJ with ±6.8% RMS stability over 1800 shots. The maximum gain of the idler achieved in this stage is only 1.7 due to the high input energy of the idler pulse, which is used as the seed. The photon conversion efficiency of the signal is 9.7% in this OPA stage. Optimization of gain and conversion efficiency is performed by adjusting the transverse displacement between the idler and the pump on the front face of the crystal, which is also the case in the final power OPA stage. Figure 4.12b compares the output signal energy from the first OPA stage as a function of the pump energy with the SNLO simulation. The efficiency achieved in the experiment is ∼27% of that predicted by simulation, which is attributed to the imperfect beam profiles and incomplete pulse overlap due to the finite buildup time of the OPO. A simple estimate of the buildup time assuming a rectangular pump pulse given in Equation 2.43 is calculated to be ∼1 ns. Delay lines for the pump have not been used since the time overlap is not a crucial factor for 1-ns operation, whereby the pump pulse for the OPA preamplifier is sliced. The 3.8-mJ signal from the preamplifier is expanded and collimated by the Galilean telescope and is used to seed the power OPA stage. The air absorption of the signal between the two OPA stages is less than ∼2% over ∼430 mm. As shown in Figure 4.12c, the power OPA stage produces a maximum experimental gain of 5.4, which is ∼35% of the gain predicted by SNLO simulation. The consistent large discrepancy between the experiment and the simulation observed in both OPAs could also be due in part from the imperfect quality of the multidomain KTA crystals used. The maximum signal energy output from the power OPA stage was measured to be 25 mJ with ±7.2% RMS fluctuation over 1800 pulses as shown in Figure 4.12d. The

signal beam pointing stability is within 0.2 mrad as shown in the inset of Figure 4.12d.

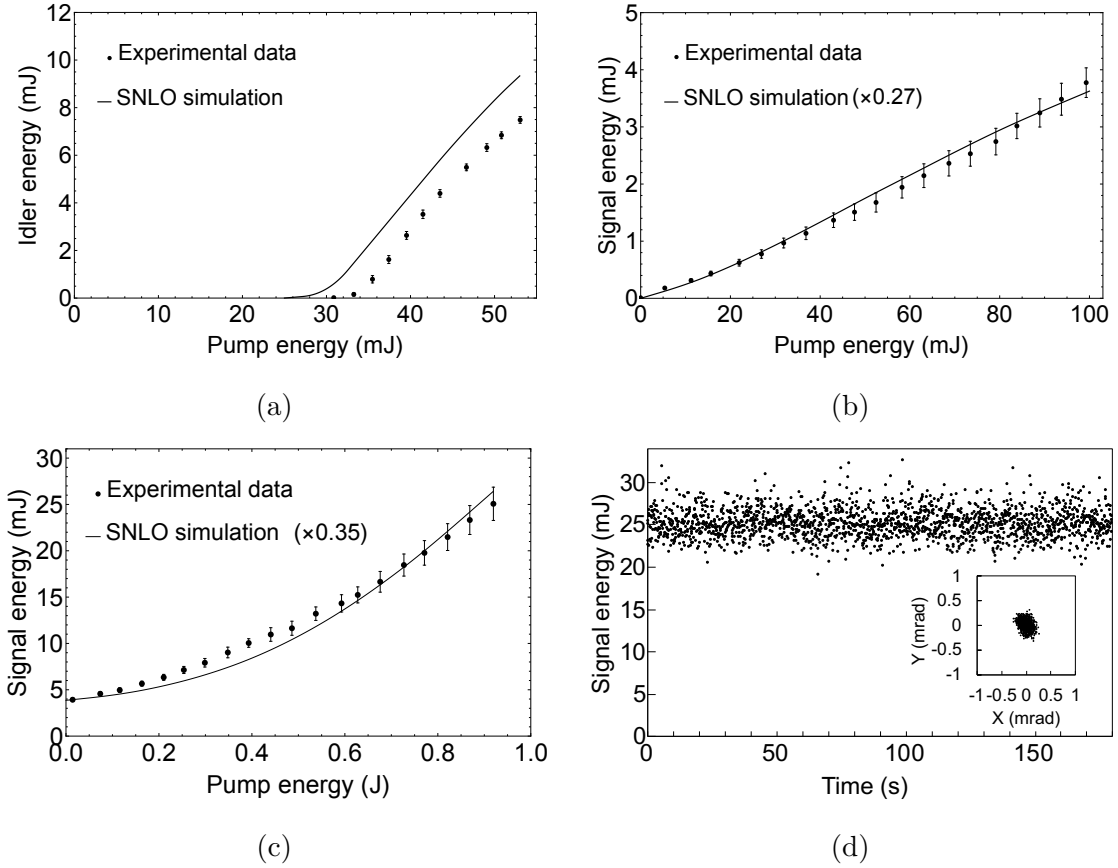

Figure 4.12: Output energy vs. pump energy of (a) the OPO stage, (b) the first OPA stage, and (c) the power OPA stage; (d) energy stability, beam pointing stability (inset) of the power OPA stage.

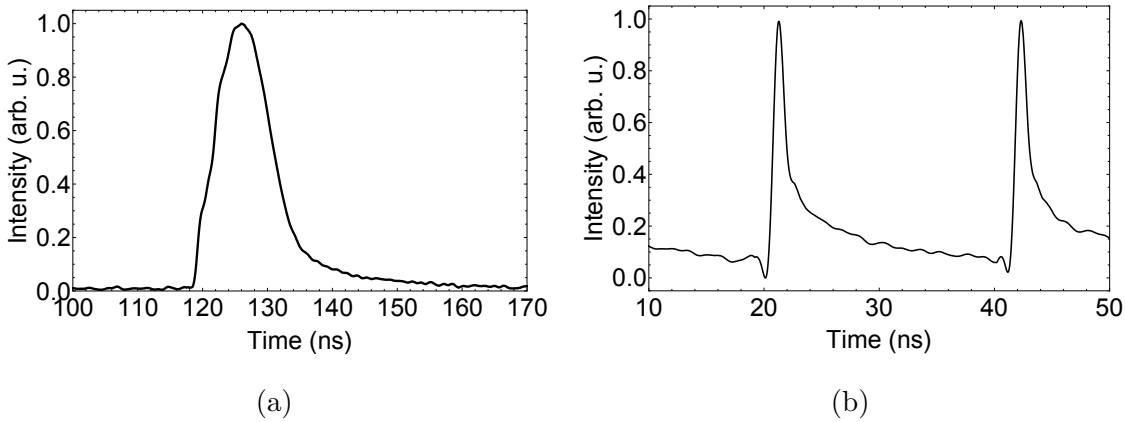

Figure 4.13: (a) Temporal profile of the signal pulse and (b) impulse response of the MCT detector at 2.75 µm.

Figure 4.13a shows the temporal profile of the signal pulse. The FWHM pulse duration of the signal was measured to be 9.6 ns by using the fast MCT detector and a 1-GHz oscilloscope. The nominal bandwidth of the MCT detector is >1 GHz at 10 µm. However, the MCT detector shows a much slower response at 2.75 µm as the signal wavelength is on the edge of its spectral response. The impulse function of the MCT detector at 2.75 µm is shown in Figure 4.13b, which was generated using the mode-locked Er:ZBLAN fiber laser. At the signal wavelength, the MCT detector has a 0.6-ns rise time and a long fall time of 12.4 ns. The measured 3-dB bandwidth of the impulse response is 400 MHz at the signal wavelength. The prolonged pulse tail may be induced by the diffusive current components due to the carries generated outside of the intended absorption region when the detecting wavelength is far away from the design wavelength. Nevertheless, 400-MHz bandwidth is sufficient for 10-ns pulse measurement, while for 1-ns pulse characterization, the MCT detector is not fast enough.

Figure 4.14a shows a typical near-field spatial beam profile of the idler beam from the OPO stage measured by the InSb camera. The InSb camera has 320×256 pixels with a pixel pitch of 30 µm. The spectral response of the InSb camera is 1.0–5.5 µm and peaks at ∼3.8 µm. The idler beam has a flat-top spatial profile and shows slight signs of back conversion in the center part of the beam. The beam quality analysis for the OPO stage was performed using a CaF_2 lens with a focal length of 100 mm. At least five beam-width measurements were taken within one Rayleigh range on either side of the beam waist, and at least five measurements were distributed beyond two Rayleigh lengths from the beam waist [163]. The second-moment beam width is used in the M-squared analysis [165]. The beam width in the x-direction (same for the y-direction) is defined as

$$W_x = 2\sigma_x, \tag{4.1a}$$

where the second moment of the beam intensity profile $I(x, y)$ across the x-direction

can be written as

$$\sigma_x^2 = \frac{\int_\infty^\infty (x - x_0)^2 I(x,y) dxdy}{\int_\infty^\infty I(x,y) dxdy}, \tag{4.1b}$$

where x_0 is the center of gravity of the beam. For arbitrary beam profile, the quadratic free-space propagation of the beam width in the z-direction is in the form

$$W_x^2(z) = W_{0x}^2 \left[1 + \left(\frac{M_x^2 \lambda}{\pi W_{0x}^2} \right)^2 (z - z_{0x})^2 \right], \tag{4.2}$$

where M_x^2 is the beam propagation factor (usually referred to as "beam quality"), W_{0x} is the beam width at the waist, and z_{0x} is the waist position. For a single-mode TEM_{00} Gaussian beam, the M-squared value is 1. For an arbitrary beam, the M-squared value is usually greater than 1. As shown in Figure 4.14 (b), the beam quality factors of the 1.8 mm×1.9 mm idler beam from the OPO stage were measured to be $M_x^2 = 2.6$ for the horizontal direction and $M_y^2 = 2.7$ for the vertical direction. This is consistent with the general expectation that the beam quality is better in the critical plane than in the noncritical plane in OPOs due to the smaller acceptance angle of the resonated idler beam in the critical direction [102, 164]. For the first OPA stage, the spatial profile of the signal beam is given in Figure 4.14c. The 2.1×1.8 mm signal shows a larger ellipticity of 1.15 and exhibits a stronger intensity lobe on the left side of the beam profile, which is in the walk-off direction. Measured by the same setup as in the OPO stage, the quality of the signal beam obtained from this OPA stage is improved to $M_x^2 = 2.0$ and $M_y^2 = 1.9$ as shown in Figure 4.14d, which could be ascribed to limited spatial filtering in the signal beam expansion while free propagating between the OPO and OPA [102]. Better quality in the noncritical plane than in the critical direction of this OPA stage was observed, which is likely due to the walk-off of the signal beam. The signal beam is expanded for seeding the power OPA stage. Figure 4.14e shows the beam profile of the amplified signal beam from the power OPA stage. The amplified signal beam is also elliptical with a FWHM beam width of

6.4 mm in the horizontal direction and 5.8 mm in the vertical direction. The walk-off effect in the power OPA stage is less significant due to larger beam sizes. The beam profile of the amplified signal beam inherits clear features from the pump beam as shown in Figure 4.4, except for much lower spatial resolution. The two relatively intense parts at 4 and 10 o'clock and two relatively weaker parts at 1 and 7 o'clock can be clearly seen on top of this flat-top distribution. The M^2 values of this stage are deteriorated somewhat to $M_x^2 = 2.8$ and $M_y^2 = 2.7$ as shown in Figure 4.14f, which were measured using a CaF_2 lens of $f = 200$ mm focal length. The measured beam profile and the beam quality derived thereof were integrated over the entire temporal profile of the signal pulse as shown in Figure 4.13.

4.4.2 1-ns operation

In order to adapt the MOPA system for 1-ns operation, the pump line to the first OPA stage was modified to include the fast Pockels cell for pulse slicing. Due to the instantaneous nature of the OPA process, the pulse duration of the converted signal is reduced, correspondingly provided a sliced pump. The modification includes using a Galilean resizing telescope to reduce the pump beam diameter by a factor of two to fit the 8-mm aperture of the Pockels cell, and using a different vacuum relay telescope to further reduce the pump beam size by a factor of 2.5 and image the laser to the KTA crystal after the Pockels cell and the polarizer. As can be seen in Section 4.2.2, the beam profile of the sliced pump shows the best uniformity when the 1-ns optical gating is set near the pulse peak (gate delay of 0 ns). However, due to the finite buildup time of the OPO, the optimum timing of the pump slicing is chosen such that the OPA stage can generate high signal energy while also maintaining a good beam profile/quality for pumping the OPCPA.

Figure 4.15a shows the output signal energy as a function of the sliced pump energy of the first OPA stage with a gate delay of 0–2 ns. For comparison, the signal

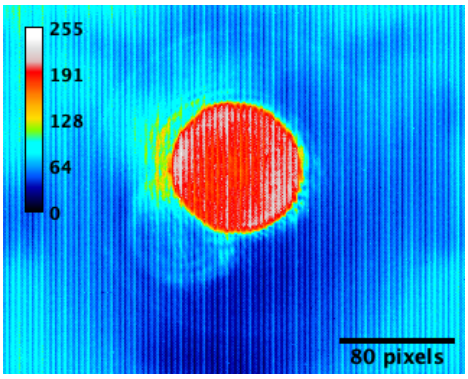

(a)

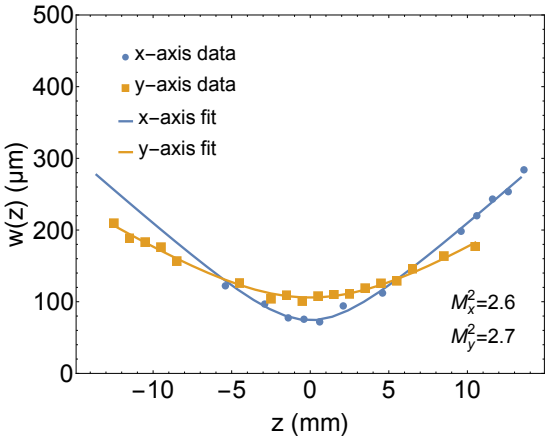

(b)

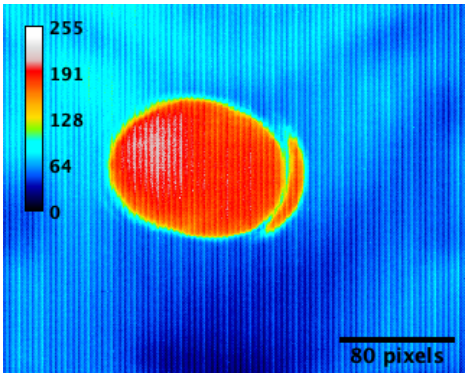

(c)

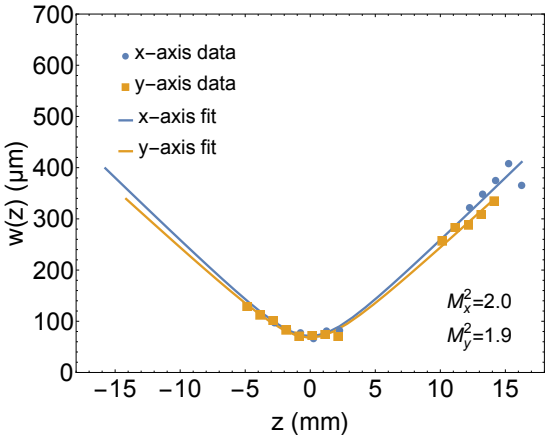

(d)

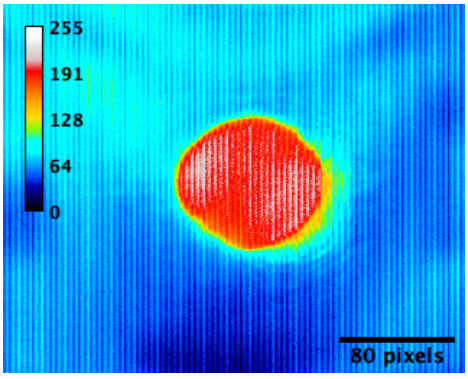

(e)

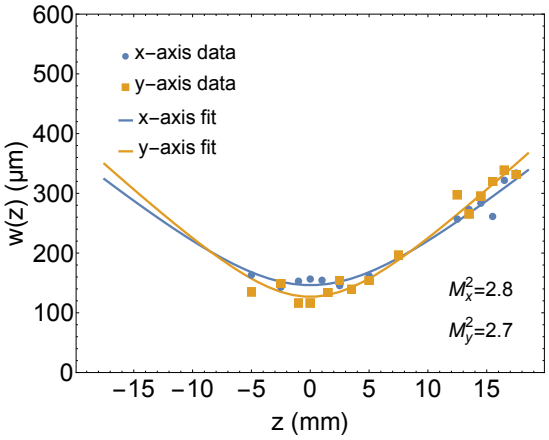

(f)

Figure 4.14: Typical time-integrated beam profile and time-integrated beam quality measurement for (a), (b) the OPO stage; (c), (d) the first OPA stage; and (e), (f) the power OPA stage.

energy output with the Pockels cell off is also shown. The conversion efficiency of this stage increases by a factor of 1.8 by using the sliced pump since only the high-intensity part of the pump pulse is used. The maximum output energy of the sliced signal pulse is 1.44 mJ with ±6.5% stability at a gate delay of 1 ns. When setting the gate delay to 0 ns and 2 ns, the maximum output signal energy decreases by 14.9% and 8.6%, respectively. The corresponding energy fluctuation shows an increase in both cases to ±8.5% and ±8.8%. This is a clear indicator of temporal mismatch of the pump and the idler pulses in the first OPA stage due to the OPO buildup time on the order of 1 ns. Figure 4.15b shows the temporal profile of the sliced signal at a gate delay of 0–2 ns. Note that the MCT detector is not fast enough at the signal wavelength to fully resolve the sliced signal pulse: the FWHM widths of these pulses are greater than 2 ns. The measured signal pulses show a decrease of pulse tail as the gate delay increases, which is consistent with the measurements of sliced pump pulses.

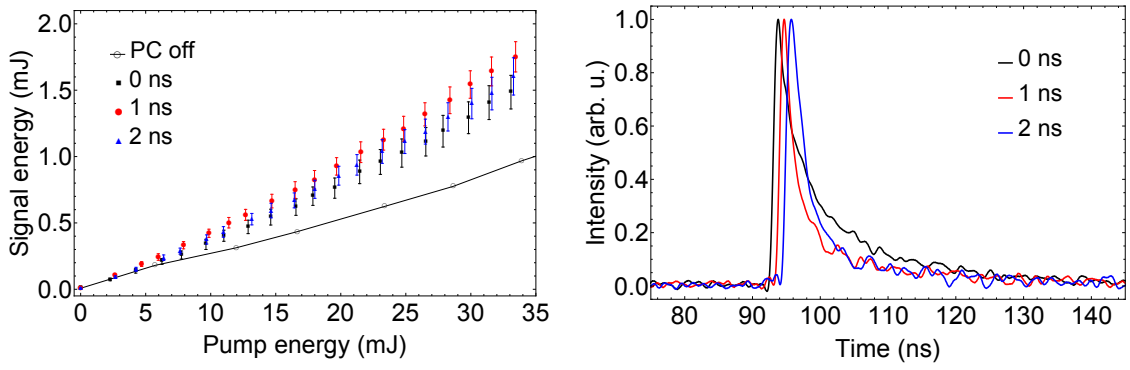

(a) (b)

Figure 4.15: (a) Output signal energy vs. sliced pump energy and (b) temporal profile of the sliced signal from the first OPA stage at different gate delays.

Figure 4.16a–4.16a shows the sliced signal beam profiles of the first OPA stage at a gate delay of 0-2 ns. Since the pulse slicing eliminates the peripheral ring shape of the pump beam at the end of the pulse, the sliced signal shows a slightly smaller beam size with decreased ellipticity of 1.12 compared to the full signal beam. The walk-off intensity lobe is less pronounced when compared to the other parts of the

beam profile in the sliced signal profile, especially in the cases with gate delays of 1 and 2 ns. Despite all the features discussed, the measured beam profiles at different gate delays do not show prominent differences. Therefore, the gate delay of 1 ns is chosen since the highest signal output energy and best energy stability can be achieved. As shown in Figure 4.16d, the M^2 value of the sliced signal of the first OPA stage was measured to be $M_x^2 = 1.9$ and $M_y^2 = 1.9$ at the gate delay of 1 ns.

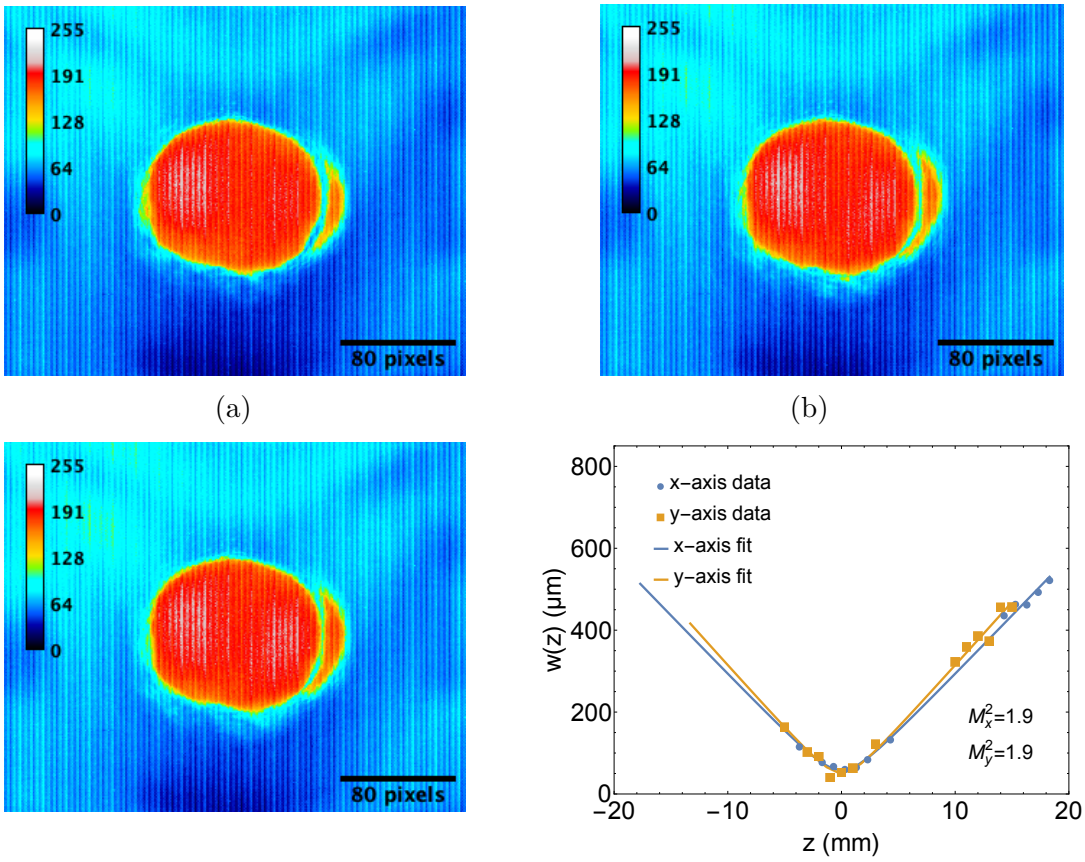

Figure 4.16: Sliced signal beam profile of the first OPA stage at a gate delay of (a) 0 ns, (b) 1 ns, (c) 2 ns, and (d) beam quality measurement of the sliced signal at a gate delay of 1 ns.

For the power OPA stage, the maximum output energy of the amplified sliced signal is 10.5 mJ, which is 41.8% of the maximum amplified signal pumped with the full 10-ns pulse profile. Figure 4.17a shows the output signal energy as a function of input pump energy of the power OPA stage with and without pulse slicing in the

previous OPA stage. The sliced signal experiences a higher maximum gain of 6.7 since the low gain regions of the pump pulse wings do not contribute significantly to the final energy. As the power OPA stage has not reached saturation, the RMS stability of the 1-ns amplified signal increases to ±16.1% over 1800 pulses since the sliced pump pulse has worse energy stability due to the finite timing jitter of the laser. Figure 4.17b shows the energy stability of this stage for both 1-ns and 10-ns operation.

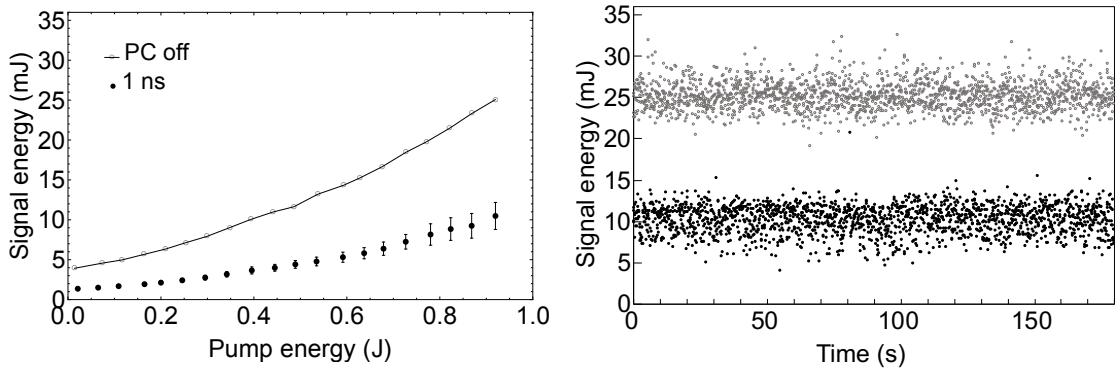

(a) (b)

Figure 4.17: (a) Output signal energy vs. pump energy and (b) energy stability of the power OPA stage with and without pulse slicing in the previous OPA stage.

Figure 4.18 shows the beam profile and beam quality measurements of the amplified 1-ns signal from the power OPA stage. As the sliced seed only uses a small portion of the pump beam near the pump pulse peak in the power OPA stage, the amplified sliced signal shows a smaller dimension of 5.8 mm×4.9 mm with improved M^2 values of $M_x^2 = 2.5$ and $M_y^2 = 2.3$ when compared to the full amplified signal. The features that present in the full amplified signal beam profile do not show in the sliced profile. Instead, the amplified sliced signal beam exhibits a more uniform spatial distribution that is highly suitable for OPCPA pumping.

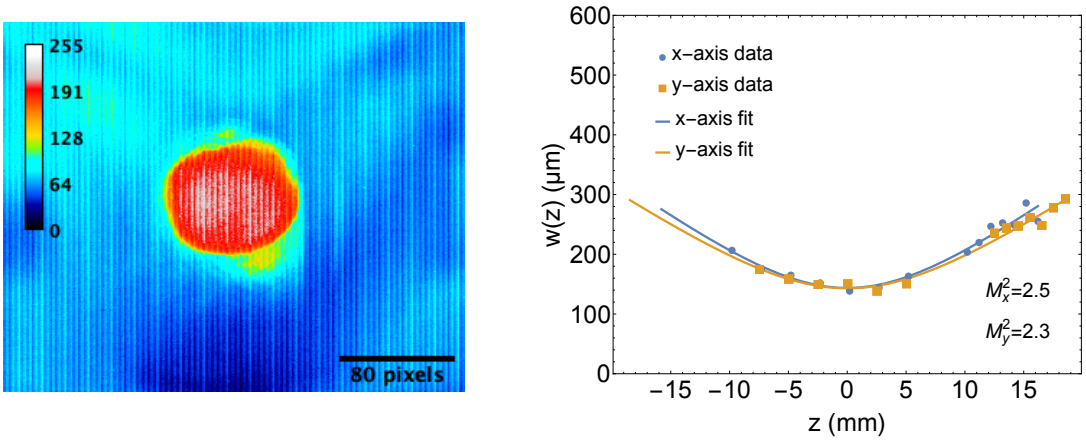

(a) (b)

Figure 4.18: (a) Beam profile and (b) beam quality measurement of the sliced signal from the power OPA stage at a gate delay of 1 ns.

4.5 Conclusion

In summary, a high-energy parametric MOPA system based on KTA crystals has been developed, which is driven by an injection-seeded, Q-switched Nd:YAG laser. This MOPA is designed as a surrogate pump source that will aid the development of the LWIR OPCPA which is designed to be pumped by an Er:ZBLAN fiber-based CPS system in the future. The KTA MOPA system delivers a signal beam up to 25 mJ at 10 Hz with a pulse duration of 9.6 ns and a beam width of 6.4 mm×5.8 mm. The central wavelength of the signal is 2726 nm with a spectral linewidth of 2.8 nm. The signal beam generated from the MOPA system preserves a good beam quality with a time-integrated M^2 value of 2.8. A maximum of 10.5 mJ of the signal could be obtained with the pulse sliced to ∼1 ns. The beam width of the sliced signal is reduced to 5.8 mm×2.9 mm, and the M^2 value is improved to 2.4. The 2.7 µm surrogate pump not only supports the initial assessment of large-core Er:ZBLAN fiber amplifiers [21], but also enables the evaluation of OPCPA in GaSe or OP-GaAs crystals in the LWIR spectral region. It has favorable characteristics for OPCPA pumping, such as uniform beam profile, good beam quality, reduced pulse duration,

and low timing jitter. However, the surrogate pump is limited to a relatively low repetition rate, which precludes possible evaluation of the LWIR OPCPA at high average powers.

CHAPTER 5

Noncollinear LWIR OPCPA in GaSe

It is well known that noncollinear geometry of OPA offers an additional degree of freedom to achieve broadband phase-matching compared to a collinear configuration. As a common practice, noncollinear configurations have been adopted not only to provide convenient separation of the amplified signal but also to enable a broader gain bandwidth and correspondingly a shorter pulse. Extensive investigation of broadband NOPA/NOPCPA with type-I phase-matching (oo-e) in negative uniaxial nonlinear crystals has been performed in the visible and near-infrared spectral range [99,166–169]. Such wavelength-insensitive phase-matching ($\partial\Delta k/\partial\lambda = 0$) in NOPCPA has enabled ultrashort pulse generation in the sub-5-fs regime [170, 171] and the production of multi-petawatt pulses [172, 173]. It has been shown that by introducing Poynting Vector Walk-off Compensation (PVWC) in wavelength-insensitive phase-matching, better energy stability and improved beam profile symmetry can be achieved at the expense of a slightly lower gain as compared to a Tangential Phase Matching (TPM) configuration [174]. The higher parametric conversion efficiency in TPM results mostly from the suppressed parasitic second-harmonic generation of the signal and the idler wave [166]. Other noncollinear configurations, such as pump-idler or pump-signal Poynting vector collinear geometries, show superior beam profile and wavefront but sacrifice the available bandwidth and conversion efficiency [175]. Careful evaluation and engineering of the noncollinear geometry are of vital importance to the development

of OPA/OPCPA systems.

In this chapter, since GaSe is more convenient to obtain commercially than OP-GaAs, the NOPCPA in GaSe is further studied. The noncollinear type-II phase-matching geometry in GaSe is analyzed, followed by simulation of NOPCPA in GaSe. The optimum noncollinear and phase-matching angles in GaSe NOPCPA are studied parametrically via simulation. The potential parasitic nonlinear processes in the GaSe NOPCPA are also simulated. Preliminary gain measurement in the GaSe NOPA at a signal wavelength of 10.6 µm is presented, followed by a discussion of the ongoing experiments including broadband gain measurement in the GaSe NOPCPA using LWIR seed. LWIR stretcher and compressor designs are modeled by ray-tracing and constructed for use in experiments.

5.1 Noncollinear OPA (NOPA)

Since the interacting waves propagate in different directions in NOPA, it is useful to express the k-vector phase mismatch in vector form:

$$\Delta \boldsymbol{k} = \boldsymbol{k}_p - \boldsymbol{k}_s - \boldsymbol{k}_i. \tag{5.1}$$

For the case of perfect k-vector phase-matching, $\Delta \boldsymbol{k}$ is set to zero, and the k-vector triangle must be closed as shown in Figure 5.1. By using the cosine rule, the phase-matching condition can be expressed as

$$k_s^2 + k_p^2 - k_i^2 - 2k_s k_p \cos\alpha = 0, \tag{5.2}$$

where α is the internal noncollinear angle between the pump and signal k-vectors, which is also referred to as the pump-tilt angle. The variation of the phase-matching angle θ between the pump and the optical axis with the noncollinear angle α can

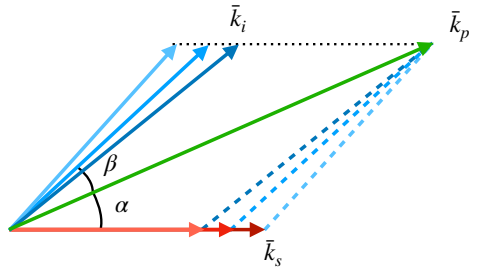

Figure 5.1: Schematic of k-vector triangle for perfect phase-matching in NOPA with narrowband pump and broadband signal. The generated idler is angularly dispersed, since its direction is automatically detuned to satisfy the phase-matching condition.

be determined accordingly, as the variation with θ impacts the extraordinary wave vector. The internal noncollinear angle β between the pump and idler k-vectors can be determined by the sine rule as

$$k_i \sin\beta = k_s \sin\alpha. \tag{5.3}$$

Due to the broad bandwidth of the signal wave, the generated idler is angularly dispersed with β being wavelength-dependent.

The conventional broadband phase-matching can be obtained by requiring that the variation of the phase mismatch with signal frequency vanishes to the first order. Therefore, by differentiating Equation (5.2) and using the fact that $d\omega_i = d\omega_s$, the broadband condition can be written as

$$k_p \cos\alpha = k_s + k_i \frac{n_{g,i}}{n_{g,s}}, \tag{5.4}$$

where $n_{g,i}$ and $n_{g,s}$ is the group index of the idler and signal, respectively. Further mathematical manipulation combining Equation (5.2) and Equation (5.4) leads to the requirement that

$$\cos(\alpha+\beta) = \frac{n_{g,i}}{n_{g,s}}, \tag{5.5}$$

which is equivalent to

$$v_{g,s} = v_{g,i}\cos(\alpha + \beta), \tag{5.6}$$

where $v_{g,i}$ and $v_{g,s}$ is the group velocity of the idler and signal, respectively. In type-I phase-matching, Equation (5.6) simply indicates that broadband amplification could be obtained when group velocities of the idler and the signal waves can be matched in the signal direction [99, 167, 169]. However, in type-II interaction, Equation (5.6) is more difficult to be interpret, as one of the idler and signal waves walks off from its k-vector direction. Note that Equation (5.6) can be satisfied only if $v_{g,i} > v_{g,s}$ in NOPA.

5.2 Type-II nondegenerate NOPA in GaSe

Type-II (eo-e) nondegenerate NOPA in a negative uniaxial crystal, particularly in GaSe crystal, is discussed in this section. A schematic diagram of the perfect type-II k-vector triangle for NOPA in a negative uniaxial crystal is shown in Figure 5.2. Note that the k-vector of the signal is chosen to be at an angle of $(\theta - \alpha)$ relative to the optical axis. Since the Poynting vectors of the signal and the pump point at a larger angle from the optical axis than their k-vectors in negative uniaxial crystals, the directions of the Poynting vector of the waves, and thus the directions of their group velocities, become closer to each other. This could lead to a better overlap of power flow and improved group-velocity matching than the opposite orientation, where the k-vector of the signal is chosen to be at an angle of $(\theta + \alpha)$ relative to the optical axis. The scheme shown in Figure 5.2 is referred to as the PVWC configuration in the following analysis.

As shown in Figure 5.2, the walk-off angle of the signal (ρ_s) and the pump (ρ_p) in

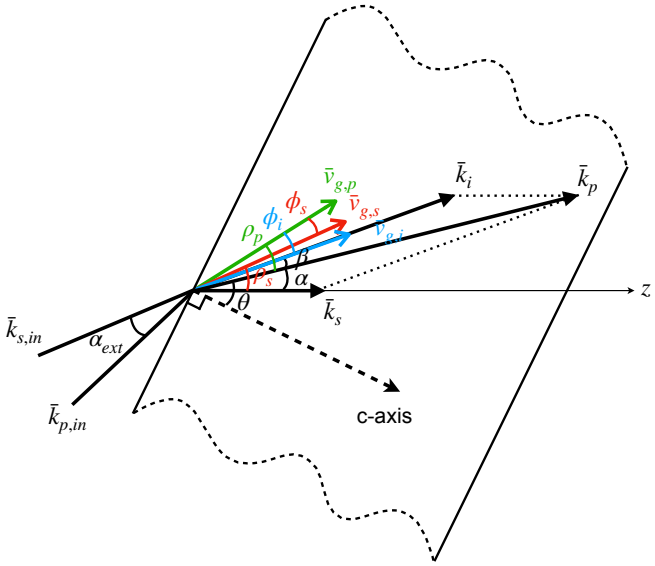

Figure 5.2: Perfect type-II (eo-e) phase-matching k-vector triangle for noncollinear OPA in GaSe with a Poynting vector walk-off compensation (PVWC) design.

negative uniaxial crystals can be formulated as

$$\tan\rho_s = \frac{\sin(\theta-\alpha)\cos(\theta-\alpha)(n_o^{s2} - n_E^{s\,2})}{n_o^{s2}\sin^2(\theta-\alpha) + n_E^{s\,2}\cos^2(\theta-\alpha)}, \tag{5.7a}$$

$$\tan\rho_p = \frac{\sin\theta\cos\theta(n_o^{p2} - n_E^{p\,2})}{n_o^{p2}\sin^2\theta + n_E^{p\,2}\cos^2\theta}, \tag{5.7b}$$

where n_E is the refractive index of an extraordinary wave along the optical axis. The angle between the group velocities of pump and signal (ϕ_s) and the angle between the group velocities of pump and idler (ϕ_i) can be calculated as

$$\phi_s = \rho_p - \rho_s + \alpha, \tag{5.8a}$$

$$\phi_i = \rho_p - \beta. \tag{5.8b}$$

The wavenumbers of the signal (e), idler (o), and pump (e) in the PVWC configuration

can be expressed as

$$k_s = \frac{2\pi n_e^s(\theta - \alpha)}{\lambda_s}, \tag{5.9a}$$

$$k_i = 2\pi n_o^i \left(\frac{1}{\lambda_p} - \frac{1}{\lambda_s}\right), \tag{5.9b}$$

$$k_p = \frac{2\pi n_e^p(\theta)}{\lambda_p}. \tag{5.9c}$$

Together with the Equation 5.2 and 5.3, the internal and external noncollinear angles as a function of phase-matching angle for the case of perfect type-II phase-matching in GaSe at a pump wavelength of 2.71 µm and a signal wavelength of 10 µm can be calculated as shown in Figure 5.3a. Figure 5.3b gives the variation of relative walk-off angles with the phase-matching angle in such configuration.

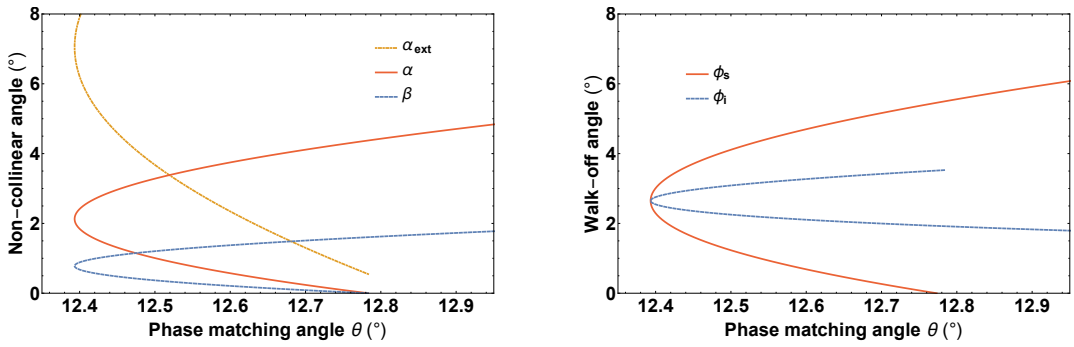

(a) (b)

Figure 5.3: (a) noncollinear angles and (b) walk-off angles relative to pump as a function of perfect type-II phase-matching angle for a signal wavelength of 10 µm in GaSe. The pump wavelength is set to 2.71 µm.

Figure 5.4 shows the phase-matching angle versus the signal wavelength for the perfect type-II interaction in GaSe pumped at 2.71 µm. Broadband amplification can be achieved around the extrema of the phase-matching curve, where the spectral variation of the phase-matching angle is minimum. Mathematically, this is equivalent to Equation (5.4). The broadband phase-matching angle can be determined accordingly at a certain pump-tilt angle. As the pump-tilt angle varies, the broadband phase-matching angle changes, as well as the corresponding perfectly phase-matched signal

wavelength.

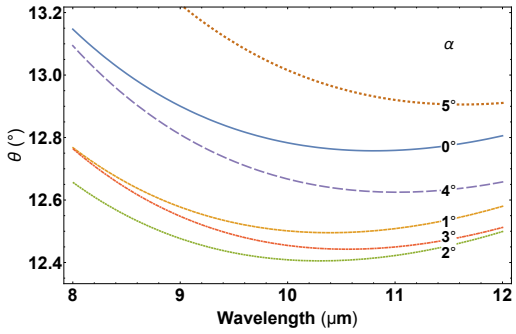

Figure 5.4: Type-II phase-matching angle as a function of signal wavelength for different pump-tilt angles in GaSe. The pump wavelength is set to 2.71 µm.

With a certain combination of pump-tilt angle and phase-matching angle, the signal wavelength offset from the perfectly phase-matched wavelength could lead to a phase mismatch that reduces the gain. Since the k-vector mismatch contributing to the gain reduction is given by the component along the signal direction [99, 167, 169], the k-number mismatch can be calculated as

$$\Delta k = k_p \cos\alpha - k_s - k_i \cos(\alpha + \beta). \tag{5.10}$$

The spectral dependence of k-number mismatch along the signal direction for the type-II NOPA pumped at 2.71 µm in 5-mm GaSe with various pump-tilt angles, and broadband phase-matching angles are shown in Figure 5.5a. Such quadratic dependence of k-number mismatch on the wavelength detuning from its perfectly phase-matched signal wavelength is a clear indication of broadband amplification. At a pump-tilt angle of 1.7° and broadband phase-matching angle of 12.4°, the perfectly phase-matched signal wavelength has a minimum of 10.3 µm. Alternatively, the spectral dependence of k-number mismatch is analyzed with a fixed center signal wavelength of 10 µm, as shown in Figure 5.5b. The corresponding phase-matching angle is adjusted to be perfectly phase-matched at 10 µm, and thus differs from the broadband phase-matching angle. As can be seen in Figure 5.5b, the slope of the

k-number mismatch curve at 10 µm is reduced as the pump-tilt angle increases to 1.7° and steepens as the angle further increases, which implies a maximum available bandwidth at 1.7°. Therefore, the above analysis indicates that a pump-tilt angle of 1.7° is the optimum for broadband phase-matching at a central wavelength of 10 µm.

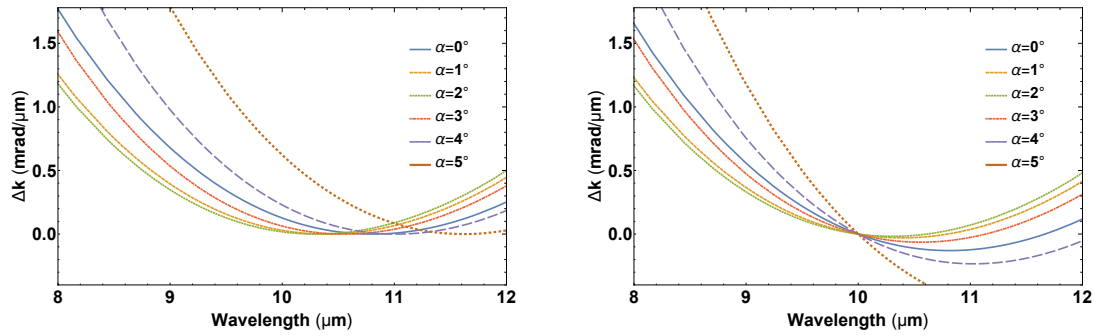

(a) (b)

Figure 5.5: k-number mismatch as a function of signal wavelength in 5-mm long GaSe (a) with broadband phase-matching angle and (b) with fixed central signal wavelength at 10 µm, for different pump-tilt angles. The pump wavelength is set to 2.71 µm.

5.3 Modeling of NOPCPA in GaSe

Theoretical investigation of the NOPCPA performance in GaSe is of significant importance as discussed in Chapter 3. To accommodate the noncollinear configuration, a set of coupled wave equations is derived for nonlinear parametric process in type-II (eo-e) NOPA in negative uniaxial crystals. Linear processes, including the spatial walk-off and crystal absorption, are included in the equations. The modified coupled wave equations, describing the directional derivative of field along the k vector of signal (z-axis), can be expressed as [91, 176]

$$\frac{dA_s(t)}{dz} = -\frac{\alpha_s}{2\cos(\rho_s)}A_s(t) + i\frac{2\omega_s d_{eff}}{n_s c}\frac{1}{\cos^2(\rho_s)}A_p(t)A_i(t)^* e^{i\Delta kz}, \tag{5.11a}$$

$$\frac{dA_i(t)}{dz} = -\frac{\alpha_i}{2\cos(\alpha+\beta)}A_i(t) + i\frac{2\omega_i d_{eff}}{n_i c\cdot\cos^2(\alpha+\beta)}A_p(t)A_s(t)^* e^{i\Delta kz}, \tag{5.11b}$$

$$\frac{dA_p(t)}{dz} = -\frac{\alpha_p}{2\cos(\rho_p+\alpha)}A_p(t) + i\frac{2\omega_p d_{eff}}{n_p c\cdot\cos(\alpha)}\frac{1}{\cos(\rho_p)\cos(\rho_p+\alpha)}A_i(t)A_s(t)e^{-i\Delta kz}, \tag{5.11c}$$

where $\alpha_{s,i,p}$ are the absorption coefficients for the signal, idler, and pump. By numerically solving these differential equations via the SSFM in the space-time domain and implementing the spectral effects in the frequency domain, the nonlinear parametric processes in the GaSe NOPCPA can be modeled. As shown in Figure 3.7, the initial signal wave is generated at a central wavelength of 10 µm with a spectral bandwidth of 4 µm. A linear chirp is applied to stretch the signal pulse to 1 ns for seeding the GaSe NOPCPA. A 10-ns, 2.75-µm narrowband pump pulse with an intensity of 1 GW/cm^2 is used to amplify to seeded signal in 5-mm GaSe crystal. The input pump-to-signal ratio is kept at 10^5, and no input idler wave is applied.

Figure 5.6 shows the impact of pump-tilt angle on the gain spectrum in two conditions shown in Figure 5.5. It should be noted that the mathematically determined broadband phase-matching condition does not correspond to the optimal arrangement of the NOPCPA in GaSe. Since a certain degree of k-number mismatch can be tolerated, phase-matching at 10 µm exhibits a broader gain bandwidth as compared to the cases where broadband phase-matching angles are used, as shown in Figure 5.6. The broadening of the parametric gain is usually accompanied by a modulation of the gain profile, which contributes to a modulation of the corresponding temporal profile. As the k-number mismatch becomes increasingly large, the amplified signal energy cannot be concentrated into a central main pulse. Instead, it is distributed over a pulse train. Therefore, a trade-off is needed between a wider bandwidth and a less modulated gain profile.

Since the FWHM duration measures only the central width of the pulse, the RMS width is used to give an integral measure of temporal distribution of pulse energy, also accounting for the energy contained in the pulse wings [177]. The RMS width can be

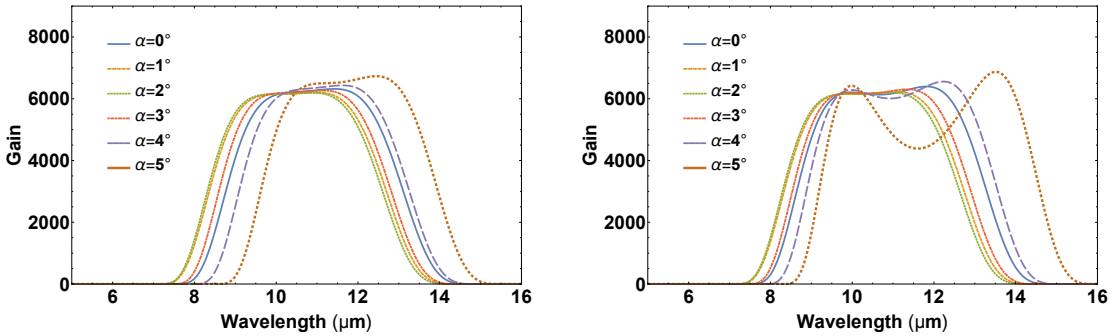

(a) (b)

Figure 5.6: Gain spectrum of the GaSe OPCPA with various pump-tilt angles (a) at broadband phase-matching angles and (b) at a fixed perfectly phase-matched wavelength of 10 µm. The crystal length is 5 mm. The pump intensity is 1 GW/cm^2.

expressed as

$$\tau_{RMS} = \sqrt{\langle t^2 \rangle - \langle t \rangle^2}, \tag{5.12a}$$

where

$$\langle t^n \rangle = \frac{\int_{-\infty}^{\infty} t^n I(t) dt}{\int_{-\infty}^{\infty} I(t) dt}. \tag{5.12b}$$

The RMS width could serve as a good candidate to quantify the trade-off. Figure 5.7a shows a two-dimensional analysis of the RMS width of the direct Fourier transform of the gain spectrum as a function of pump-tilt angle and perfectly phase-matched signal wavelength. An optimum pump-tilt angle of 1.7° can be observed, consistent with the previous k-number mismatch analysis. A range of perfectly phase-matched signal wavelength from 9.2 µm to 11.5 µm and pump-tilt angle of 1–2° can be chosen to generate comparable RMS widths, indicating a good amount of tolerance in the operating parameters.

Figure 5.7b analyzes the transform-limited output signal pulse. The broadband phase-matching curve is also shown in the contour map. The analysis shows a minimum RMS width at a pump-tilt angle of 1.7° and a perfectly phase-matched wavelength of 8.6 µm, which corresponds to a phase-matching angle of 12.53°. Due to the quadratic feature of the phase-matching curve, there is a symmetric minimum at 12.3 µm

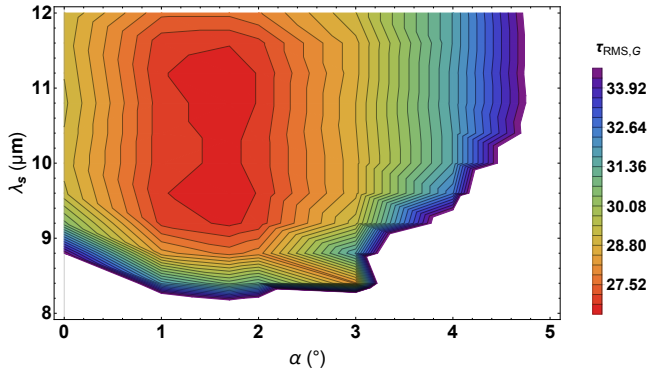

(a)

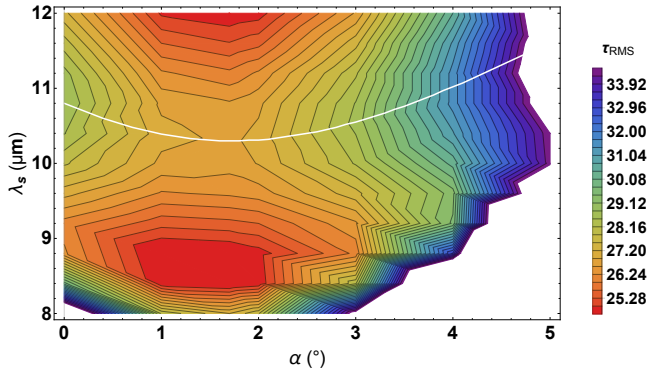

(b)

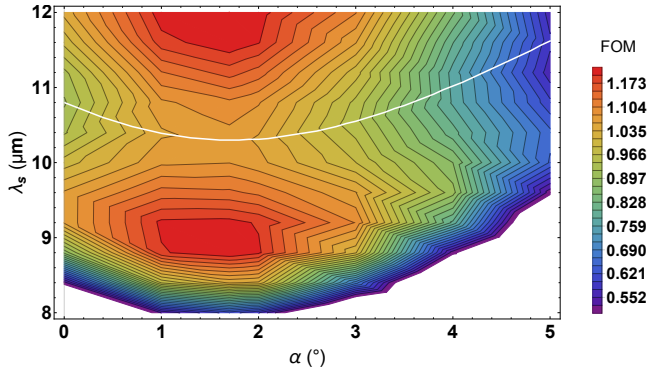

(c)

Figure 5.7: (a) RMS pulse width of the direct Fourier transform of gain spectrum, (b) RMS pulse width of the amplified signal, and (c) normalized FOM of GaSe OPCPA as a function of pump-tilt angle (α) and perfectly phase-matched signal wavelength (λ_s). The broadband phase-matching curve is shown as a solid white line in the contour map. The crystal length is 5 mm, and the pump intensity is 1 GW/cm^2.

about the broadband phase-matching curve (solid white line), which gives the same phase-matching angle of 12.53°.

Considering also the conversion efficiency and the transmission of air in addition to the RMS width, a FOM could be defined as

$$FOM = \frac{\eta \times T}{\tau_{RMS}}, \tag{5.13}$$

where η is the photon number conversion efficiency and T is the transmission of air in typical laboratory conditions as shown in Figure 1.1. Figure 5.7c shows the normalized FOM as a function of pump-tilt angle and perfectly phase-matched signal wavelength. The hot spots in the FOM analysis move closer to the broadband phase-matching curve as compared to the RMS width map. The optimal parameter configuration appears at a pump-tilt angle of 1.7° and a signal wavelength of 9 µm (a phase-matching angle of 12.48°). At a pump-tilt angle of 1.7°, an improvement of 8% can be achieved when phase-matched at a blueshifted signal wavelength of 9 µm when compared to 10 µm. Further comparing the FOM given in the optimized configuration with that obtained in collinear geometry (see Chapter 3), an improvement of 12% can be seen in the optimization. Figure 5.8 shows a comparison of the optimized gain spectrum with that of the collinear case. The optimized gain profile is centered at ∼10.5 µm with a gain bandwidth of 5 µm. Although the gain profile features a small modulation, a significant broadening of spectral gain can be seen towards the shorter wavelength.

The amplified signal spectrum and its spectral phase at the optimized combination of parameters for NOPCPA in GaSe is shown in Figure 5.9a, which is overlaid with the initial signal spectrum. The output spectrum is slightly narrowed after amplification. The corresponding transform-limited output pulse profile is shown in Figure 5.9b. No significant pulse wings can be observed. The FWHM width of the pulse is reduced by 14.6% to 56.9 fs as compared to the collinear case.

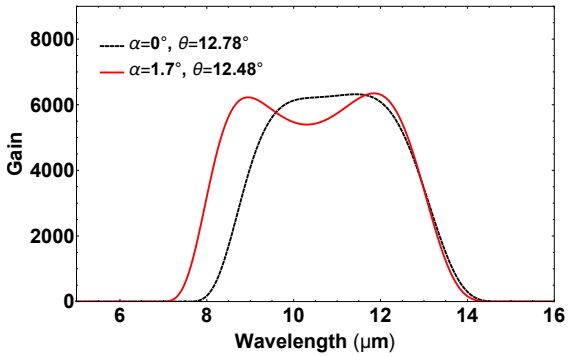

Figure 5.8: Comparison of gain spectrum obtained in the optimized noncollinear geometry phase-matched at 9 μm at a pump-tilt angle of 1.7° with and that obtained in collinear geometry phase-matched at 10 μm. The crystal length is 5 mm, and the pump intensity is 1 GW/cm^2.

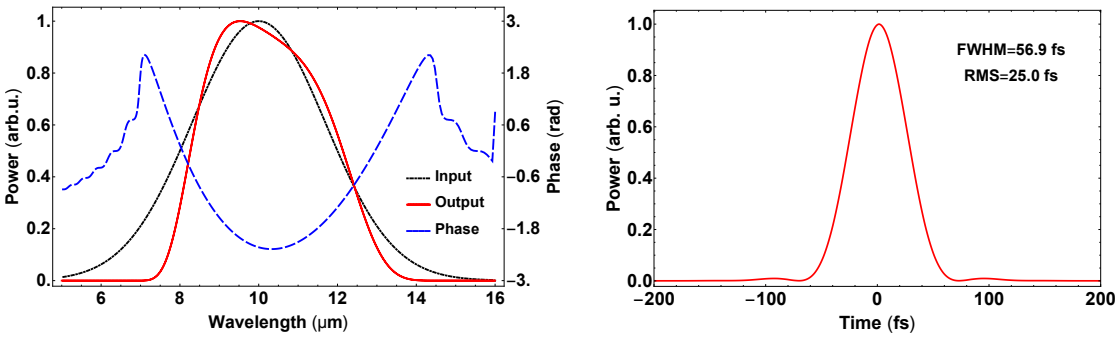

(a) (b)

Figure 5.9: (a) Output signal spectrum and spectral phase of GaSe OPCPA in noncollinear geometry with a noncollinear angle of 1.7° at a perfectly phase-matched wavelength of 9 μm and (b) Fourier transform of the spectrum assuming phase has been compensated. The crystal length is 5 mm, and the pump intensity is 1 GW/cm^2.

Further optimization of the NOPCPA performance is conducted by varying the signal pulse duration (τ_s) while fixing the pump pulse duration (τ_p) to 1 ns. The pump and signal are simultaneously incident on the crystal, and their peak amplitudes occur at the same time. Figure 5.10a shows the normalized FOM as a function of the pump-to-signal pulse duration ratio simulated at the optimized noncollinear geometry with a pump intensity of 1 GW/cm^2 and a pump-to-signal intensity ratio of 10^5. An optimum ratio of the pump-to-signal pulse duration of 1.3 can be observed. The FOM is 6.7% higher than that for the equal pump-to-signal pulse duration. Optimization of the signal pulse delay ($\Delta\tau = \tau_p - \tau_s$) with respect to the pump pulse is shown in Figure 5.10b at a pump-to-signal pulse duration ratio of 1.3. By launching the signal pulse 50 ps ahead of the pump pulse, the FOM slightly increases (by 2.6%) as compared to the zero time difference. This is because the pump pulse has a slightly larger group velocity than the signal pulse. Compared to the collinear geometry phase-matched at 10 µm with equal pulse duration and zero pulse delay, a total improvement of 34.5% is obtained in these optimizations. The 1-ns pumped gain profile/output signal spectrum obtained with optimized pulse ratio and delay are not shown since they do not show a significant difference as compared to the case when 10-ns pump is used.

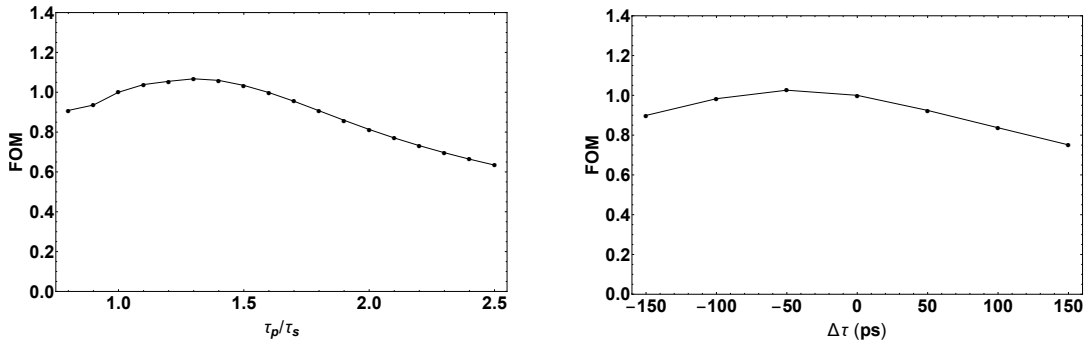

(a) (b)

Figure 5.10: Variation of the normalized FOM (a) with the pump-to-signal pulse duration ratio and (b) with signal pulse delay in the optimized noncollinear geometry with a pump tilt angle of 1.7° and a phase-matching angle of 12.48°. The pump intensity is 1 GW/cm^2, and pump-to-signal intensity ratio is 10^5.

Parasitic nonlinear processes such as frequency doubling of the interacting waves are important considerations in the design of OPCPA systems. The presence of such parasitic processes might distort the output spectrum, reduce the efficiency, and thus degrade the OPCPA performance [166]. In the type-II GaSe NOPA, the signal SHG cannot be phase-matched, while the idler SHG (oo-e) is unavoidable. The phase-matching curves for the type-II GaSe NOPA and the idler SHG are shown in Figure 5.11 at a pump-tilt angle of 1.7°. In the optimized NOPA configuration (α=1.7°, θ=12.48°) as shown in the previous section, the perfectly phase-matched idler SHG is achieved at an idler wavelength of 3.54 µm.

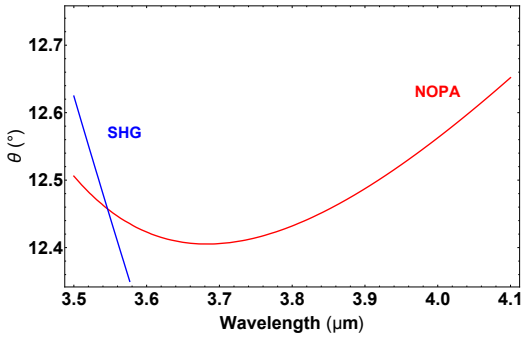

Figure 5.11: Type-II phase-matching angle in 2.71-µm pumped GaSe NOPA (α=1.7°) as a function of idler wavelength. The phase-matching curve for idler SHG is also shown.

To evaluate the effect of the idler SHG in the GaSe NOPCPA, an additional coupled wave equation for generating the idler SHG ($\omega_{iSH} = 2\omega_i$) needs to be used in the SSFM modeling in the time domain. The equation can be written as

$$\frac{dA_{iSH}(t)}{dz} = -\frac{\alpha_{iSH}}{2\cos(\alpha+\beta+\rho_{iSH})}A_{iSH}(t) - i\frac{2\omega_{iSH}d_{eff,iSH}}{n_{iSH}\cdot c\cdot\cos(\alpha+\beta)} \cdot\frac{1}{\cos(\rho_{iSH})\cos(\alpha+\beta+\rho_{iSH})}A_i(t)^2, \tag{5.14}$$

where $d_{eff,iSH}$, n_{iSH}, α_{iSH} are the effective nonlinear coefficient, index of refraction, and absorption coefficient of the extraordinary idler SHG wave, respectively. The

walk-off angle of the idler SHG wave can be calculated as

$$\tan \rho_{iSH} = \frac{\sin(\theta+\beta)\cos(\theta+\beta)(n_o^{iSH^2} - n_E^{iSH^2})}{n_o^{iSH^2}\sin^2(\theta+\beta) + n_E^{iSH^2}\cos^2(\theta+\beta)}. \tag{5.15}$$

To account for the conversion of the idler to the idler SHG, a term $-A_i(t)^* A_{iSH}(t)$ need to be added into Equation (5.11b). The idler SHG is investigated in the optimized NOPA configuration with 5-mm GaSe crystal at a pump intensity of 1 GW/cm^2.

Figure 5.12 shows the spectrum of the amplified signal, the generated idler, and the parasitic idler SHG in the GaSe NOPCPA. According to the simulation, the intensity of the parasitic idler SHG in the noncollinear configuration is considerably lower than the signal and the idler, and is one half of that generated in the collinear geometry. No spectrum distortion exists, and the conversion efficiency of the signal wave is not affected by such a parasitic process.

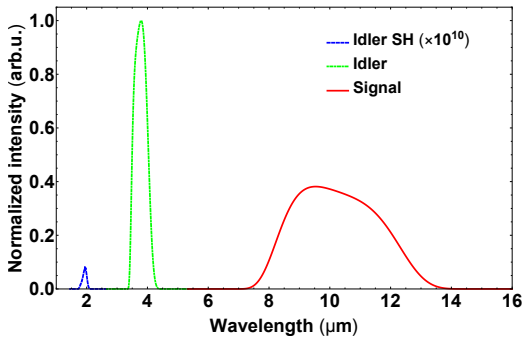

Figure 5.12: Spectrum of the signal, idler, and idler SHG in the 5-mm GaSe NOPCPA pumped at an intensity of 1 GW/cm^2. The pump-tilt angle and the phase-matching angle are 1.7° and 12.48°, respectively.

5.4 Seeding NOPA at 10.6 μm

By using the surrogate pump source operating at a wavelength of 2.75 μm and a pulse duration of 10 ns, an initial NOPA experiment in GaSe has been performed adopting a conventional 10.6-μm CO_2 laser (SYBRAS, 48-1) as the seed [178]. The CO_2 laser

generates seed pulses with a duration of 1.06 µs and timing jitter of 2.55 µs at a duty cycle of 2.5% and a repetition rate of 5 kHz, which is then synchronized with the Nd:YAG laser. The beam diameter of the CO_2 laser is 3.5 mm and has an M^2 value that is better than 1.2. The output polarization of the CO_2 laser is vertical. A cleaved, Z-cut GaSe crystal (Eksma Optics) of 5×5×5 mm^3 was used in the experiment with type-II (eo-e) phase matching at a θ of 12.4° in a noncollinear geometry. The crystal is uncoated, such that the 2.75-µm pump suffers a 16.6% Fresnel loss.

The schematic of the experimental setup is shown in Figure 5.13. A 15× telescope with two CaF_2 lenses (L1, L2) has been used to resize the 2.75-µm pump beam to provide the intensity needed for gain measurement in GaSe. The pump beam on the crystal is ∼0.9 mm in diameter, which is determined by inspecting the damage spot that was later created in the experiment. A periscope is used to rotate the polarization of the CO_2 laser, such that both the pump and the seed are horizontally polarized. The seed is then directed at a noncollinear angle of 128 mrad with respect to the pump to the GaSe, corresponding to the 2.2° internal noncollinear angle in the crystal. An iris is inserted right before the GaSe crystal to reduce the seed beam size to roughly match the pump beam, such that a higher ratio between the amplified signal and the seed can be obtained. The MCT detector is used to measure the amplified 10.6-µm signal. A Ge filter with a cutoff frequency of 7.3 µm (Andover Corp.) prevents the residual pump pulse from entering the detector.

Due to the significant timing jitter of the CO_2 laser, only the seed pulses that exhibit a good timing overlap with the pump are selected for analysis. A typical temporal pulse profile of such seed is shown in Figure 5.14a, where the ∼10-ns amplified signal can be seen superimposed on the peak of the seed pulse. The trace is magnified in the inset of Figure 5.14a to give a more clear view of the amplified signal pulse. A hyperbolic sine squared model, consistent with small-signal parametric gain, is used to fit the measured dependence of parametric gain on the pump intensity. Figure 5.14b

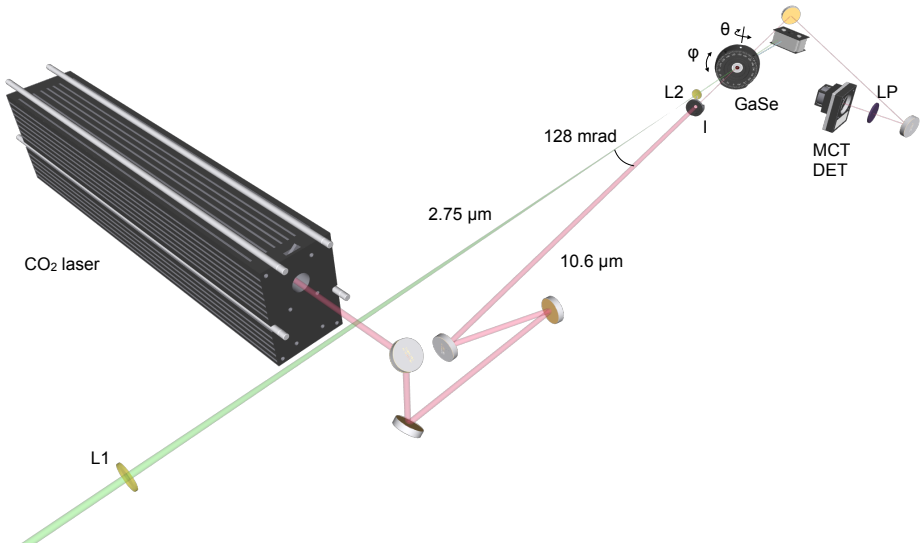

Figure 5.13: Schematic diagram of 2.75-μm driven GaSe NOPA seeded by a CO_2 laser.

shows the experimental data and the model fit for the dependence of single-pass power gain at 10.6 μm for the type-II, 5-mm GaSe crystal on the 2.75-μm pump intensity. A simulation of this process is also shown in Figure 5.14b, which is based on the use of the nondepleted-pump solution of standard coupled differential equations for three-wave mixing. The crystal surface was damaged at an intensity of ∼0.25 GW/cm^2 in the experiment, which is attributed to the relatively long pump pulse duration of 10 ns, along with the pump beam profile that has not been optimized at that time. By slicing the pump pulse to a duration of ∼1 ns, the damage threshold intensity could be increased by a factor of ∼3. A further increase is anticipated by optimizing the pump beam profile, such that a higher intensity that is close to ∼1 GW/cm^2 can be directed to the crystal surface with a more uniform intensity distribution. Based on the fit to the experimentally measured gain scaling, a single-pass parametric gain of ∼5.5×10^3 can be obtained at a pump intensity of 1 GW/cm^2.

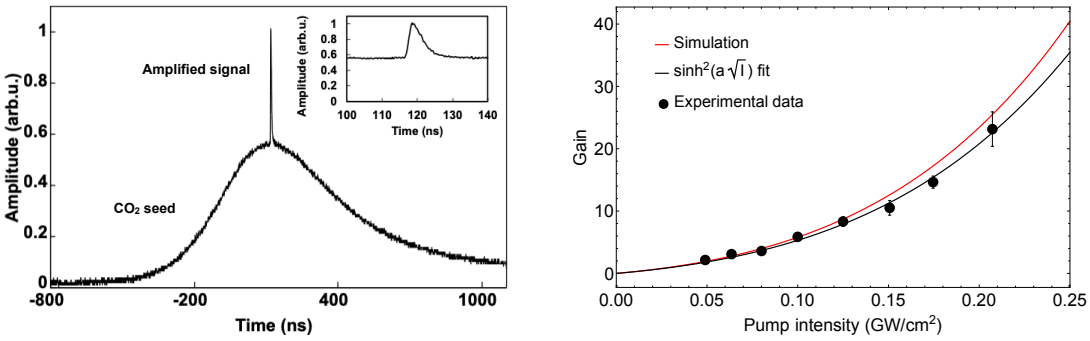

(a) (b)

Figure 5.14: (a) Temporal pulse profile of the CO_2 seed and the amplified signal (also shown in the inset) and (b) single-pass power gain at 10.6 µm as a function of 2.75-µm pump intensity in type-II NOPA using 5-mm long GaSe.

5.5 Broadband LWIR parametric seed source

In order to perform NOPCPA in GaSe, a broadband LWIR seed is an indispensable part of the entire system. Additionally, characterization of such an ultrashort seed source in the LWIR range of high importance. The experimental setup and the current performance of the LWIR seed source are briefly discussed in this section (see more details in Ref. [179]). The single-shot LWIR spectrometers used in the experiments are introduced in the Appendix A, and the LWIR autocorrelator/Cross-Correlation Frequency-Resolved Optical Gating (XFROG) developed/to be developed are described in Appendix B.

Intrapulse DFG of two intense laser pulses with different colors from a common Ti:sapphire laser system in GaSe/AGS crystal has been proven to be a simple approach that can generate broadband, CEP stable LWIR signal tunable near 10 µm [63,65,180]. To avoid strong TPA in crystals by using transform-limited femtosecond pumping, DFG based on chirped phase-matching between the two-color outputs of a Ti:sapphire amplifier has been proposed to provide higher conversion efficiency while maintaining broad phase-matching bandwidth [64].

The broadband LWIR seed source is based on intrapulse DFG of two-color chirped

Ti:sapphire laser output in an AGS crystal using type-II (eo-e) phase-matching geometry. The Ti:sapphire laser is a custom-built CPA system which is capable of delivering >22 mJ, ∼40 fs pulses at 480 Hz. The two-color chirped output is generated by using a 2-µm thickness nitrocellulose pellicle placed in the regenerative amplifier and an acousto-optic programmable dispersive filter (Fastlite, Dazzler HR 800) introduced after the oscillator. The two-color output beam is resized to 5 mm diameter via a 5× Galilean reflective telescope.

Figure 5.15 shows the experimental setup of the LWIR seed source. This seed design can be accommodated within a 1×1 ft^2 footprint. In the setup, the two-color output from the Ti:sapphire laser is split into two paths by using a half-wave plate and a thin-film polarizer combination. The vertically polarized seed path beam carries ∼10% of the energy of the pump path beam that has horizontal polarization. The pump path is delayed and is combined with the seed path through another thin-film polarizer, such that the 770-nm pulse in the pump path beam and the 830-nm pulse in the seed path beam can be overlapped in a 5×5×0.4 mm^3 AGS crystal (Eksma Optics, cut at θ=45.4°, ϕ=0°) both temporally and spatially. The crystal is broadband AR coated in the range of 700–900 nm on the front surface and in the range of 8–12 µm on the back surface.

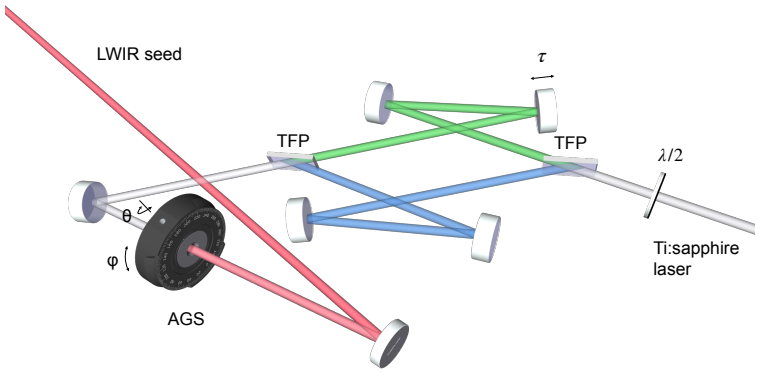

Figure 5.15: Schematic diagram of the experimental setup of the LWIR seed generation via chirped-pulse DFG in AGS crystal.

The generated LWIR signal is centered at 10.3 µm with a FWHM of 1.1 µm, supporting sub-five-cycle (∼140 fs) transform-limited pulses [181]. Figure 5.16 shows the spectra of the two-color Ti:sapphire input and the generated LWIR pulse from the AGS DFG, which were measured by a compact CCD spectrometer (Ocean Optics, USB4000) and the single-shot home-made prism-based spectrometer, respectively. The central wavelength of the generated LWIR pulse can be conveniently adjusted by changing the wavelength separation of the two-color output. The LWIR spectral bandwidth can be further broadened by precise tailoring of the chirp of the seed and the pump in the two-color input. A genetic algorithm has been applied in the numerical simulation of the intrapulse DFG process in AGS to explore the parameter space, which includes spectral phase, intensity, temporal offset of the pump and the seed, the crystal length, and the phase-matching angle. A three-fold increase in bandwidth has been demonstrated in the simulation, supporting sub-two-cycle (∼60 fs) LWIR pulse generation [181]. Experiments are underway to validate those simulations.

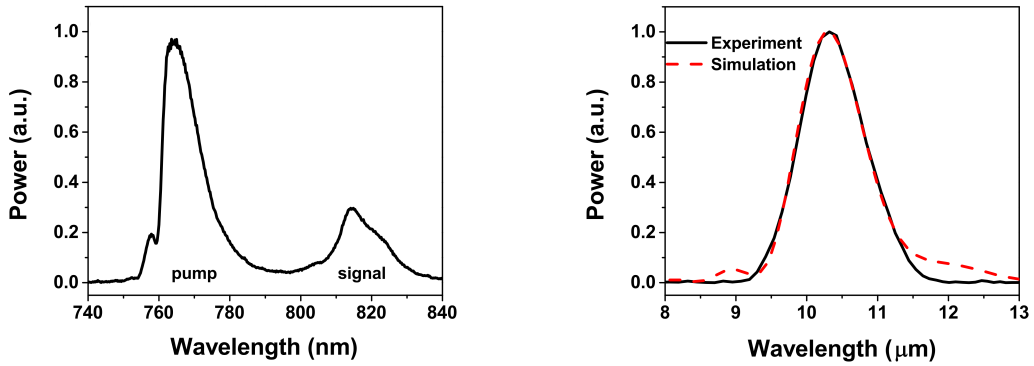

(a) (b)

Figure 5.16: (a) Spectrum of the two-color Ti:sapphire laser input and (b) the generated LWIR pulses via DFG in the AGS crystal [181].

5.6 Pulse stretcher and compressor

Pulse stretcher and compressor are key components of a CPA/OPCPA system. Treacy-Martinez [182–184] configurations based on diffraction gratings are the commonly used designs, which could provide stretching/compression ratios typically on the order of $10^{3–4}$. The Treacy compressor is comprised of a parallel pair of identical diffraction gratings with ruled surfaces facing each other and lines parallel to each other, providing negative GVD that is tunable by adjusting the grating separation. The Martinez stretcher can provide tunable positive GVD by using two identical antiparallel diffraction gratings with equal and opposite inclination and parallel lines, and a unity magnification refracting/reflecting telescope. Double-pass arrangements are usually adopted in Treacy-Martinez configurations by using roof mirrors to retroreflect the beam, such that spatial chirp can be eliminated and the temporal dispersion can be doubled. The dispersion provided by the Martinez stretcher can be exactly matched over all orders to that of the Treacy compressor with opposite signs. A deviation from perfect match may be caused by the finite beam and grating size, misalignment/mismatch of the stretcher and compressor components, and the aberration introduced by the lenses/mirrors used in the stretcher telescope.

To analyze the dispersion introduced by the stretcher and compressor design (Treacy-Martinez configuration) and to gain some insight into the space-time coupling phenomena such as spatial and angular chirp, a ray-tracing model based on a nonlinear extension of the ABCD matrix model is used [185]. The model is presented with more details in Appendix C. In the model, the grating groove density is chosen to be 100 lines/mm to provide an optimum degree of dispersion, such that the gratings can be oriented closer to the Littrow angle to maximize the grating efficiency while also providing enough stretching/compression ratio with reasonable grating separation. The angle of incidence to the grating is set at 45°. The stretcher uses spherical mirrors with a focal length of 609 mm and a distance between the gratings and the

spherical mirrors of 430 mm. The slant distance between gratings in the compressor is 358 mm. Figure 5.17a–5.17f shows the spectral phase up to the third-order in the wavelength range of 8–12 µm from the model provided by the stretcher alone and the stretcher/compressor combination. The stretcher design provides a chirp that can stretch the 4-µm bandwidth transform-limited pulses to ∼1 ns. The size of gratings in the stretcher and compressor for 4-µm bandwidth is >160 mm and >180 mm, respectively. Richardson Gratings, Newport could provide gratings with similar parameters. The 6-inch spherical concave mirror needed in the stretcher is available from Edmund Optics. Since the spherical mirror has a large focal length, the stretcher could be implemented in a folded configuration [5, 186]. In contrast to the results obtained from the analytical formula [187], modeling shows residual dispersion at the edges of the spectrum after the compressor due to the spatial aberrations introduced in the stretcher. The angular and spatial chirp after the compressor are shown in Figure 5.17g–5.17h. To avoid the angular and spatial chirp over such broad bandwidth and to eliminate residual dispersion, aberration-free Offner-type stretcher [188] could be adopted for a future broader bandwidth seed source.

For the current 1-µm bandwidth seed, 50×25 mm^2 plane-ruled diffraction gratings with 100 lines/mm blazed at 10.6 µm (Thorlabs, GR2550-10106) are used. According to the manufacturer (Thorlabs), the diffraction efficiency of the gratings at perpendicular polarization remains >80% in the wavelength range of ∼7–19 µm at Littrow angle. The measured efficiency at 10.6 µm is ∼80% at perpendicular polarization and shows a small variation of 3.3% with incident angles ranging from 35° to 60°. Spherical mirrors used in the stretcher have a focal length of 203.2 mm. The distance between gratings and spherical mirrors is 38.2 mm. The slant distance between gratings in the compressor is 329.8 mm. Figure 5.18 shows the spectral phase and the angular and spatial chirp as a function of wavelength in the range of 9–11 µm in the 1-µm bandwidth design. Based on the model, 2-inch gratings in the stretcher can support

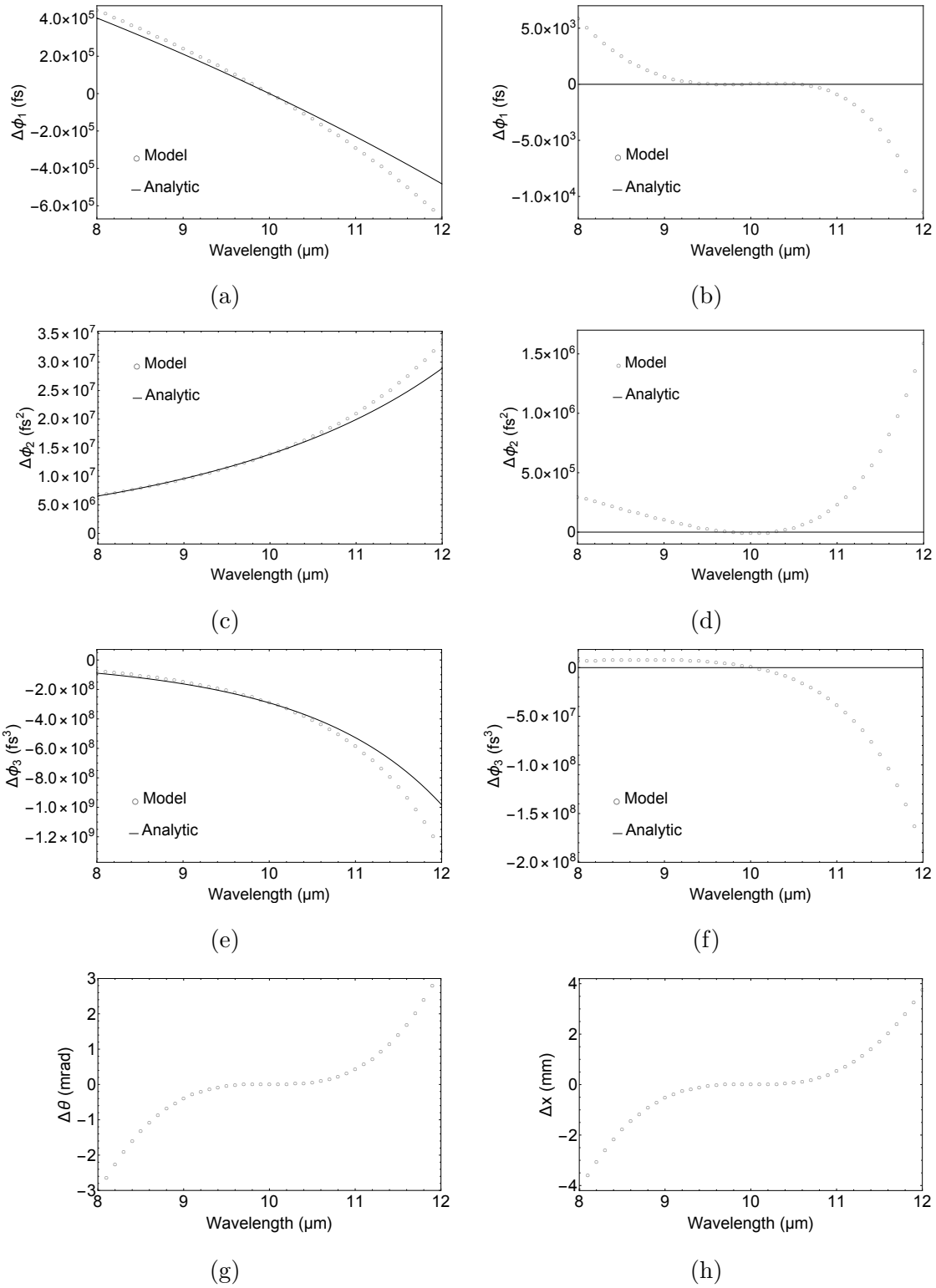

Figure 5.17: (a)–(b) First-order, (c)–(d) second-order, (e)–(f) third-order spectral phase, (g) angular, and (h) spatial chirp as a function of wavelength introduced by the stretcher alone ((a), (c), (e)), and the stretcher and compressor combination ((b), (d), (f), (g), (h)) in the 4-μm bandwidth design.

∼1.4 µm bandwidth and stretch the pulses to a duration of ∼340 ps. The residual dispersion and chirp after compression is significantly reduced, providing a satisfactory performance over 1-µm bandwidth.

5.7 NOPCPA in GaSe

Figure 5.19a shows the schematic of the experimental setup for the NOPCPA experiment. A 6.25× relay telescope with two CaF_2 lenses (L1, L2) has been used to resize the 1-ns, 2.73-µm beam to increase the pump intensity. The 2.73-µm pump and the LWIR seed are synchronized. The LWIR seed source is located next to the output compressor of the Ti:sapphire laser system. As a result, the seed beam has to propagate ∼8 m in air before entering the NOPCPA setup. The beam divergence of LWIR seed is measured to be 8.4 mrad in the horizontal direction and 1.1 mrad in the vertical direction. The large horizontal divergence might originate from a small undesired noncollinear angle between the two-color Ti:sapphire inputs in the DFG stage, such that the generated LWIR seed is angularly dispersed. The horizontally polarized LWIR seed is then directed to the stretcher that can accommodate 1.4-µm bandwidth seed (see Section 5.6). Based on the parameter scan as shown in Section 5.3, an external noncollinear angle of 102 mrad is used in the NOPA after the stretcher, corresponding to an internal angle of 1.7° in GaSe. The GaSe crystal used in the NOPA is the same as introduced in Section 5.4. The amplified seed after the NOPA is compressed in the conjugate compressor (see Section 5.6). A photograph of the experimental setup of the GaSe NOPCPA is shown in Figure 5.19b. Experiments are still underway to demonstrate the broadband gain in GaSe and the pulse compression performance of the NOPCPA.

Since the Rayleigh range of the LWIR seed is considerably smaller than that of the near-infrared beam, in the future, the two-color Ti:sapphire input from the regenerative

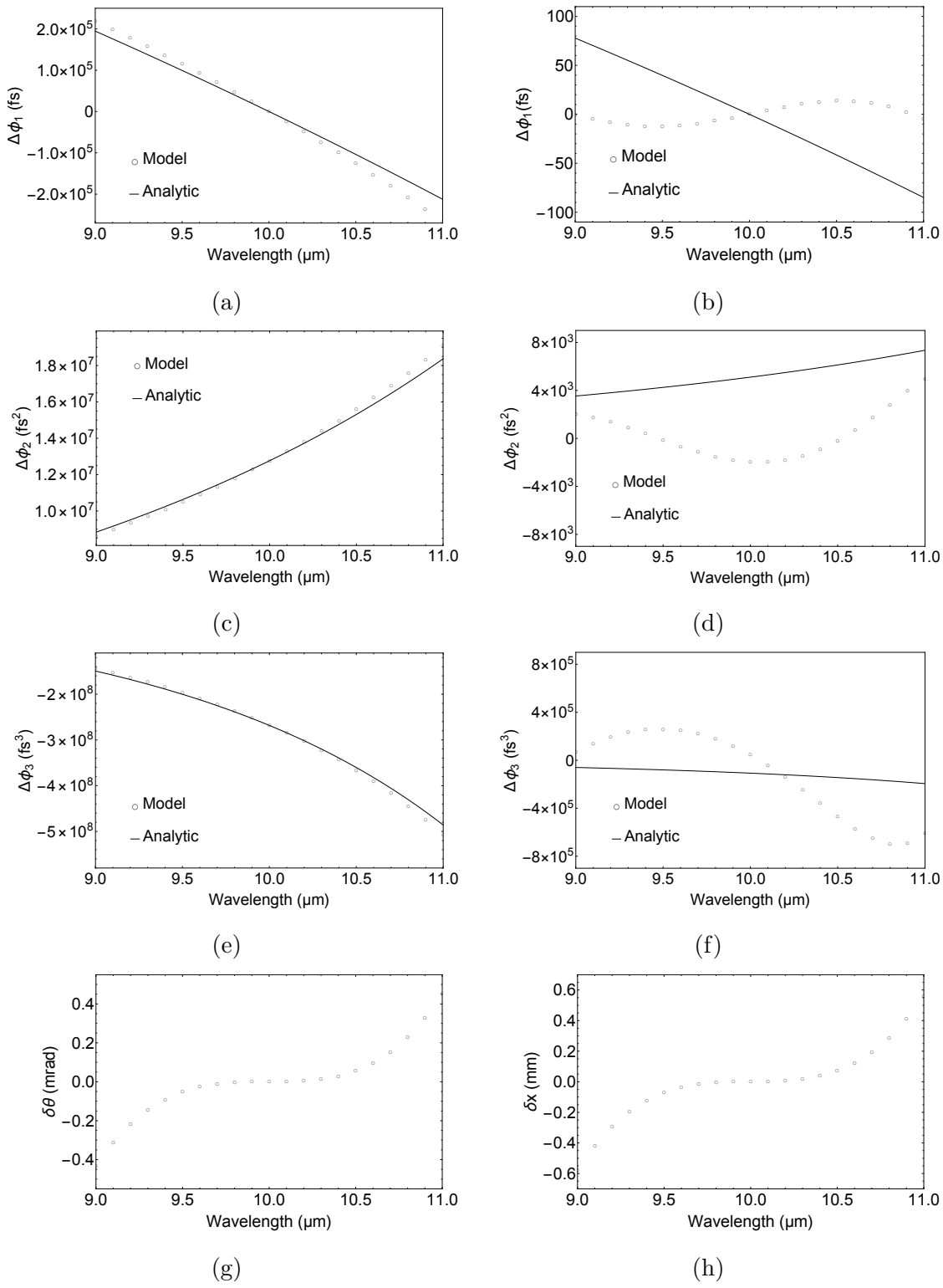

Figure 5.18: (a)–(b) First-order, (c)–(d) second-order, (e)–(f) third-order spectral phase, (g) angular, and (h) spatial chirp as a function of wavelength introduced by the stretcher alone ((a), (c), (e)), and the stretcher and compressor combination ((b), (d), (f), (g), (h)) in the 1-μm bandwidth design.

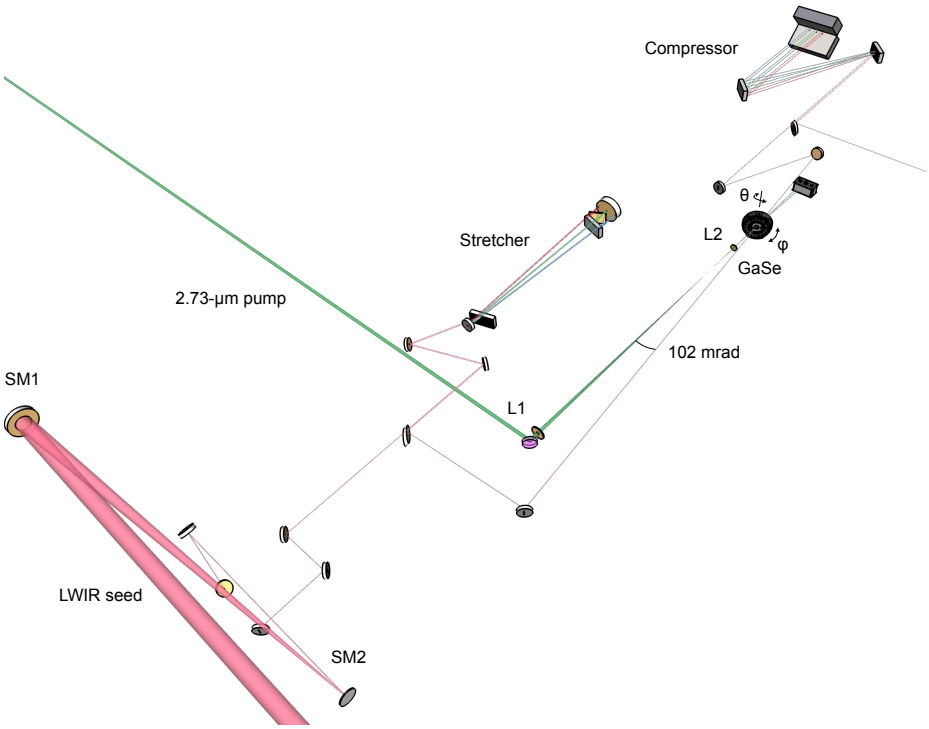

(a)

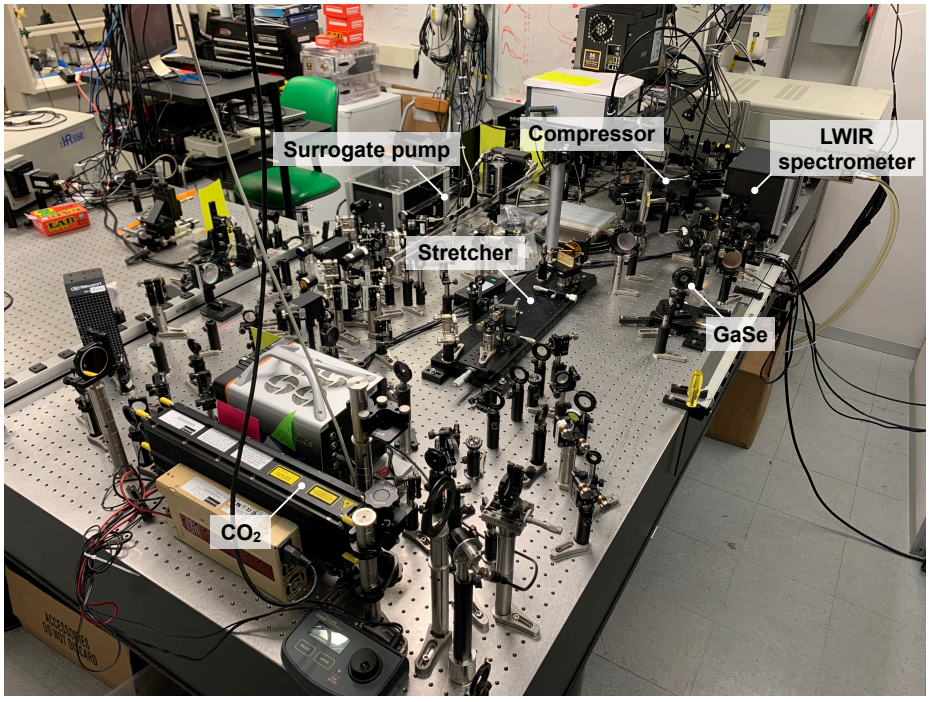

(b)

Figure 5.19: (a) Schematic diagram of 2.75-μm driven GaSe NOPCPA seeded by the LWIR seed source; (b) photograph of the experimental setup of GaSe NOPCPA.

amplifier will be sent to the NOPCPA side and then compressed in another compressor. As a result, the propagation distance of the LWIR seed will be significantly reduced, which should help improve the operation and performance of the NOPCPA.

5.8 Conclusion

In conclusion, 2.7-µm driven type-II (eo-e) phase-matched NOPCPA in GaSe has been analyzed using a one-dimensional model based on standard coupled wave equations for three-wave mixing, which are modified to accommodate the noncollinear configuration and to include linear processes (*i.e.*, spatial walk-off and crystal absorption). Parametric studies have been performed to determine optimum noncollinear and phase-matching angles in GaSe NOPCPA, such that broad gain bandwidth and high conversion efficiency can be obtained simultaneously. Additionally, optimization of the timing overlap and the pump-to-signal pulse duration ratio is also performed, resulting in a considerable improvement compared to the collinear case studied in Chapter 3. Parasitic nonlinear processes (*i.e.* SHG of the signal/idler) are shown to be negligible based on the simulation. The initial NOPA experiment has been conducted using a 10.6-µm CO_2 laser as the seed. Although the crystal damage occurs at a lower intensity than expected when using 10-ns, 2.7-µm pump, a single-pass parametric gain over 5000 is predicted based on the fit to the experimentally measured gain scaling if a pump intensity of 1 GW/cm^2 can be imposed on GaSe, which can be achieved by using the sliced 2.7-µm pump with improved beam profile. A broadband LWIR seed source has been developed concurrently based on the intrapulse DFG of a two-color chirped Ti:sapphire laser in an AGS crystal using type-II (eo-e) phase-matching geometry. The seed source generates CEP stable, 1.1-µm bandwidth LWIR signal centered at 10.3 µm to support the NOPCPA experiment. Analyzed using a ray-tracing model, a nanosecond pulse stretcher and compressor in Treacy-Martinez configuration has

been designed for 4-μm bandwidth LWIR seed. A prototype GaSe NOPCPA has been developed using a pulse stretcher and compressor modified to accommodate the current 1.1-μm bandwidth LWIR seed. Experiments are still underway to validate the performance of the GaSe NOPCPA.

CHAPTER 6

Other Applications for LWIR OPCPA

Although this dissertation work is directly motivated by laser-pulse filamentation studies and n_2 measurements in ambient air, the development of few-cycle LWIR OPCPA with high peak power is also of interest for a range of applications that benefit from a high U_p at long driving wavelength, as discussed in Chapter 1. These applications include strong-field physics, attosecond science, and laser-particle acceleration. Additionally, the LWIR spectral range is the "fingerprints" region for many molecules. The ultrafast LWIR OPCPA source could be used as a unique tool for molecular spectroscopy. Since filamentation studies and n_2 measurements have been introduced in Section 1.4, other important applications are briefly presented in the following sections.

6.1 Strong-field physics and attosecond science

The field of strong-field physics studies the interaction of intense electric fields with matter and has developed the capability of tracking electronic and structural dynamics on the attosecond time scale. A classic recollision model has been introduced to qualitatively interpret strong-field interactions. In the model, the electron is emitted close to the peak of the oscillating laser electric field, and then it accelerates in the field before recolliding with its parent ion roughly three-quarters of an optical cycle later. The returning electron could either recombine with the ion and emit a

high-energy photon via a coherent frequency upconversion process (high-harmonic generation) or scatter off the parent ion inelastically, causing nonsequential double (or multiple) ionization or just scatter elastically. This classic model usually asks for tunneling conditions as a prerequisite, which can be satisfied by requiring the Keldysh parameter $\gamma = \sqrt{\frac{I_p}{2U_p}} \ll 1$, where I_p is the ionization potential of the target atoms [189]. By adopting MIR sources, low peak intensity can be used to maintain a high U_p while avoiding ground-state depletion/ionization saturation, which is conducive for classical interpretation of experimental results in the tunneling limit. Additionally, since the time that the electron accelerates in the field is proportional to the optical period, high-energy recollision electrons can be created with a longer wavelength driver, which are beneficial for imaging applications. Finally, by tuning to a longer driving wavelength, high-quality attosecond bursts can be generated via high-harmonic generation with a denser frequency comb, higher cutoff energy ($I_p + 3.17U_p$), and a reduced attochirp [189–191].

Experimental validation of the wavelength scaling of the Keldysh picture has been performed by concurrently analyzing the production of energetic electrons and photons emitted by argon atoms interacting with ultrashort pulses at fixed intensity but with different laser wavelengths at 0.8 µm, 1.2 µm, 2 µm, 3.6 µm. As the ionization increasingly approaches the tunneling regime by increasing the wavelength, the electron behavior evolves closer to the classical limit, and the harmonic generated can reach the extreme-ultraviolet region (50–200 eV), which supports the implicit predictions in Keldysh's theory [190]. Ultrahigh harmonics have later been demonstrated by guiding a 330 TW/cm^2, 3.9 µm, 80-fs pulse in high-pressure helium gas, producing a bright high-harmonic x-ray supercontinuum that spans from ultraviolet to more than 1.6 KeV in the soft x-ray region, corresponding to a 2.5 attoseconds (single x-ray cycle) transform-limited pulse [191]. The unprecedented time resolution offered by such coherent attosecond soft x-ray pulses enables time-resolved probing of ultrafast electronic

dynamics in atom, molecules, and solids [192]. MIR high-harmonic generation has also been explored in narrow-bandgap solid-state materials, giving promise to future compact ultrafast and coherent x-ray sources, although the microscopic processes involved differ from the classical recollision model that is valid in the gas-phase experiments [193]. Time-resolved imaging of electron recollision with Xe atoms in the tunneling regime has been demonstrated by using a 100 TW/cm^2, 3.1 µm, 30-fs, CEP-stable pulse in combination with a reaction microscopy detection system that is capable of providing a 3D view of the momentum distribution of strong-field interactions in full particle coincidence. Recollisions with Xe atoms at both low (meV) and high (hundreds of eV) electron energies have been studied, giving insights into low-energy structures (as well as very-low-energy and zero-energy structures) that are not predicted by the classical model, and atomic structures that permit extraction of the doubly differential elastic electron scattering cross-section via laser-induced electron diffraction, respectively [189]. This MIR source and reaction microscope system has also been applied in dynamic visualization of larger and heteronuclear molecular structures via laser-induced electron diffraction, allowing the retrieval of multiple bond lengths from aligned acetylene molecules [194]. Moreover, nonsequential double ionization has been investigated, revealing complex and unexpected interplay between the returning electron and its parent ion core [189, 195].

6.2 Laser-driven particle acceleration

Accelerating fields that could be achieved in conventional radio-frequency accelerators are typically limited to the order of 10 MV/m owing to the electrical breakdown of metal structures. Advanced laser-based acceleration concepts, such as dielectric laser acceleration in a vacuum and laser wakefield acceleration in plasma, have spawned significant interests as they circumvent the limit of conventional accelerators and

are able to produce accelerating fields on the order of 1–10 GV/m. As a result, such advanced schemes are highly promising to create compact tabletop accelerators instead of conventional large-scale accelerator facilities for producing relativistic particle beams. Laser-accelerators feature reduced energy spread since they produce low-charge bunches at a high repetition rate, and thus bremsstrahlung energy losses become less significant. Additionally, the electron bunch lengths obtained from laser-accelerators can be as short as sub-femtoseconds to attoseconds, which is attractive to many applications [196, 197].

Dielectric laser acceleration is realized by confining tailored longitudinal modes of the electric field in near-field structures with phase velocity synchronized to the particle beam [196, 198]. The first reported dielectric laser acceleration was demonstrated in fused silica dual-grating structures (*i.e.*, two opposing binary gratings of period of 0.8 µm, separated by a vacuum gap of 400 nm) fabricated via lithographic techniques and was driven by 1 ps long Ti:sapphire laser pulses. This laser-accelerator prototype achieved high-gradient (>250 MeV/m) acceleration of relativistic (60 MeV) electrons over 550 µm [198]. By using a femtosecond Ti:sapphire laser, sub-relativistic (sub-100 keV) electrons have been accelerated in silicon dual-grating structures over 5.6 µm with a high accelerating gradient of 370 MeV/m [199]. Relativistic electron acceleration with a record high gradient of ∼690 MeV/m has also been demonstrated recently in fused silica dual-grating structures driven by a Ti:sapphire laser with a pulse duration of 90 fs [200]. Although the majority of the work has been performed by using ubiquitous Ti:sapphire lasers, it is desirable to use MIR sources to drive the dielectric laser-accelerators since multiphoton ionization leading to dielectric structure breakdown can be greatly mitigated, and higher laser intensity could be applied to dielectric structures resulting to higher accelerating gradients. Additionally, since the dimension of grating structures is on the order of laser wavelength, using MIR sources alleviates the difficulties for manufacturing processes. Furthermore, electron bunches

with higher charge can be transmitted through the larger apertures if MIR source could be used.

In laser wakefield acceleration, relativistic self-focusing of the pulse can be initiated above the critical power threshold and is arrested by electron blow-out forming a bubble (ion channel) behind the laser pulse. This bubble exerts an attractive Coulomb force on the blown-out electrons, causing them to stream around the bubble and self-inject in the blow-out region, exciting a wakefield with ideal focusing and accelerating properties. The electrons carried by the bubble constantly gain momentum as they propagate through the background ion plasma and reach relativistic energies, producing a monoenergetic electron bunch. It has been shown that a stable wake for acceleration can be excited when the laser spot size can be matched to the blow-out radius, such that the transverse ponderomotive force can be roughly balanced by the force of the ion channel [201]. Laser plasma acceleration experiments relying on relativistic self-focusing have usually required large, terawatt, ultrafast lasers and scale favorably to the MIR spectral regime as the critical power for relativistic self-focusing decreases with the increase of laser wavelength squared. The ponderomotive force that pushes the electrons outwards and drives the wakefield also scales as laser wavelength squared. The first demonstration of MIR laser wakefield acceleration has accelerated relativistic electrons up to ∼12 MeV in a hydrogen gas jet with moderate density and width that exceeds self-focusing scale length [202]. The driving source is a ∼100-fs, 0.25 TW, 3.9-µm OPCPA, which enables studies of near- and above-critical density interactions. The results show that the charge obtained in 3.9-µm laser-driven electron beams significantly exceeds the charge in beams driven at 0.8 µm [202]. Coherent control of the relativistic electron beam from wakefield acceleration with 3.9-µm laser pulses in near-critical density plasma has been performed, demonstrating improved electron total charge, energy spectrum, beam pointing, and fluctuation [203]. The application of TW CO_2 laser in wakefield acceleration can be achieved with an even lower plasma

density giving higher electric charge per bunch, further validating the wavelength scaling trend [204].

6.3 Molecular spectroscopy

The MIR spectral range is the well-known molecular fingerprint region, within which many rotational and vibrational resonances of molecules and molecular functional groups can be used as their unique identifiers. In particular, the two atmospheric transmission window regions can be exploited for sensitive detection of small traces of environmental and toxic vapors in a variety of atmospheric, security, and industrial applications [205]. Introduced in the early 2000s, optical frequency comb spectroscopy in the MIR spectral range revolutionized precise measurements of molecular structure and dynamics. Parametric downconversion devices driven by mode-locked lasers are one of the approaches that could generate MIR frequency combs. Compared to the conventional Fourier transform infrared spectroscopy, which employs incoherent, thermal light, frequency comb spectroscopy uses coherent combs and simultaneously provides large spectral bandwidth, high-frequency precision, and high brightness. High sensitivity and accuracy over a broad spectral bandwidth can thus be achieved along with reduced data acquisition time in frequency comb spectroscopy for remote sensing and diffraction-limited microscopic probing applications [205, 206].

In frequency comb spectroscopy, the spectra of the combs are attenuated and phase-shifted selectively by molecular resonances and are analyzed preferably by Fourier transform spectroscopy, which uses only a single photodetector instead of a dispersive spectrometer. Frequency comb Fourier transform spectroscopy is essentially a time-domain technique in which the pulse train of a comb is interferometrically sampled by a second pulse train of a different repetition rate. The two interfering combs interrogate the absorbing sample and generate a lower-frequency comb composed of

heterodyne beats for further manipulation through digital signal processing. Depending on how the second pulse train is generated, frequency comb spectroscopy has two implementations – Michelson-based Fourier transform spectroscopy and dual-comb spectroscopy. The former approach introduces the second pulse train by varying the optical delay of a Michelson interferometer, whereas the latter newly emerged approach incorporates a second frequency comb source. Although more technical challenges are encountered, dual-comb spectroscopy overcomes the speed and resolution limitations in the Michelson-based approach by eliminating the moving parts [205]. Mutually coherent combs with absolute external frequency reference are essential to achieve very high resolution and accuracy in dual-comb spectroscopy and are easier to be obtained from parametric devices via DFG processes, where their carrier-envelope offset frequency is zero due to passive CEP stability [207].

Dual-comb spectroscopy is currently the most widely pursued form of frequency comb spectroscopy, but mostly in the near-infrared range. Due to the lack of efficient MIR frequency combs and the difficulty of synchronization, dual-comb spectroscopy is still limited to proof-of-concept demonstrations with a few exceptions in the MIR regime [207]. Specifically in the LWIR window, the first dual-comb spectroscopy demonstration is based on intrapulse DFG of a Ti:sapphire comb in GaSe [208]. This ∼10-µW system can give a 2 cm^{-1} resolution over 70 µs from 9–12 µm and has been used to perform rapid, time-resolved spectroscopy of fluctuating ammonia vapor over 44 m [209]. By using 1-µm pumped, mW-level OP-GaP OPO, dual-comb spectroscopy of methane and ambient water vapor has been demonstrated in 6–8 µm with a resolution of ∼0.3 cm^{-1} over 40 µs [210]. Recently, a 0.25 mW, 4–12 µm source based on intrapulse DFG of a near-infrared comb from a Er:fiber platform in OP-GaP has been developed for dual-comb spectroscopy of vapor phase methanol and ethanol, providing a spectral resolution of 0.003 cm^{-1} over 20 ms in static measurements and 0.23 cm^{-1} over 285 µs in dynamic measurements [206].

CHAPTER 7

Conclusion and Perspective

Optical parametric chirped-pulse amplification is the most promising solid-state technology for intense few-cycle LWIR pulse generation. It also provides a viable alternative to the CO_2 lasers, which are bandwidth-limited to the production of ∼ps pulses. Intense LWIR pulses are highly valuable for a range of applications such as laser pulse filamentation, strong-field physics, laser-driven particle acceleration, and molecular spectroscopy. While the current MIR parametric sources have reached peak power on the order of several gigawatts, the near-infrared pumped OPCPA operating in the LWIR range is well below gigawatt level. Major limitations encountered in the LWIR OPCPA development at present are the availability of high-energy MIR pump lasers, suitable nonlinear materials, and appropriate ultrafast diagnostics in the challenging LWIR range. The high-energy MIR pump pulses may be provided in the future by several technologies. One of them is the Er:ZBLAN coherently pulse stacked fiber laser operating at ∼2.7 µm, which is under development in the community. This dissertation describes concurrent efforts in developing a surrogate, nanosecond, 2.7-µm parametric pump source and presents the simulation and experimental work on the development of a 2.7-µm driven nanosecond LWIR OPCPA based on GaSe crystal as a gain medium. The development of an LWIR parametric seed source and its diagnostics in the spectral and temporal domains is also presented. Although the experimental work is still ongoing, important milestones have already been achieved

towards demonstrating LWIR OPCPA for the first time. The key accomplishments over the course of this work are reiterated in the following text, along with proposals for future improvements.

To validate the feasibility of the proposed 2.7-μm driven LWIR OPCPA, simulations were first performed using a numerical model developed based on standard coupled differential equations for three-wave mixing. Based on the simulation results, GaSe and OP-GaAs are predicted to be suitable nonlinear materials for the production of broad-bandwidth pulses in the LWIR region via type-II (eo-e) CPM and QPM, respectively. At a pump intensity of 1 GW/cm^2 and a pump-to-signal ratio of 10^4–10^5, OPCPA in both crystals can support 2-cycle LWIR pulse amplification with a parametric gain of several thousand within 5–6 mm long crystals. If a pump energy of 10 mJ is available, the output LWIR seed could be amplified to the millijoule level, corresponding to several tens of gigawatts of peak power for a 2-cycle pulse duration.

To support the initial assessment of large-core Er:ZBLAN fiber amplifiers and also to enable the concurrent evaluation of LWIR OPCPA in GaSe/OP-GaAs crystals, a surrogate 2.7-μm parametric pump source has been developed based on KTA crystals, which is driven by an injection-seeded, Q-switched Nd:YAG laser. The surrogate pump adopts a parametric MOPA architecture in order to allow efficient energy scaling while maintaining good beam quality. Up to 10.5 mJ of output energy in 1.2-ns pulse duration has been achieved from the KTA MOPA system, generating a 5.8 mm×4.9 mm, 2.7-μm beam with a M^2 value of 2.4. Although the surrogate pump is limited to a relatively low repetition rate of 10 Hz which precludes possible evaluation of LWIR OPCPA at high average powers, characteristics such as uniform beam profile, good beam quality, reduced pulse duration, and low timing jitter are favorable for pumping LWIR OPCPA for energy scaling demonstration.

Further simulations have been conducted on the GaSe OPCPA in noncollinear geometry, which can offer an additional degree of freedom to achieve broader gain

bandwidth and can also provide convenient separation of the amplified signal. A non-collinear angle of 1.7° and a phase-matching angle of 12.48° show optimal performance in simulation studies, such that broad gain bandwidth and high conversion efficiency can be achieved simultaneously in GaSe NOPCPA. To experimentally evaluate the gain in GaSe crystal, initial NOPA experiment has been conducted using the surrogate pump and a 10.6-μm CO_2 laser as the seed, demonstrating an expected single-pass parametric gain over 5000 at a pump intensity of 1 GW/cm^2. For broadband seeding of the NOPCPA, a surrogate seed source based on intrapulse DFG in AGS crystal has been developed, which generates CEP-stabilized, 1.1-μm bandwidth LWIR signal centered at 10.3 μm. A three-fold increase in bandwidth has been predicted after optimization of the input phases based on the simulation employing a genetic algorithm. By adopting the optimized noncollinear/phase-matching angles, a prototype GaSe NOPCPA has been developed using a pulse stretcher and compressor designed to accommodate the current LWIR seed with limited bandwidth. A nanosecond pulse stretcher and compressor design has also been evaluated for the future LWIR seed source with optimized bandwidth. To provide a more intuitive view on the state of LWIR OPCPA development, a diagram of the prototype is shown in Figure 7.1. The surrogate pump has been completed, while the surrogate seed is deployable but needs further bandwidth optimization. The developed prototype has been aligned using the surrogate seed, and broadband gain in GaSe NOPCPA is currently under experimental evaluation. In addition, pulse recompression will be demonstrated in the near future, and pulse characterization will be performed using the home-built LWIR diagnostics, including the single-shot prism/grating spectrometer and the InSb autocorrelator. Although the bandwidth and the repetition rate are currently limited due to the constraints posed by the surrogate sources, the development of the prototype is significant for initial proof-of-concept studies of the MIR pumped LWIR OPCPA. Validation of the full-bandwidth performance of the GaSe NOPCPA will be

performed in the future after optimization of the bandwidth of the surrogate seed and implementation of the nanosecond pulse stretcher and compressor in the OPCPA architecture.

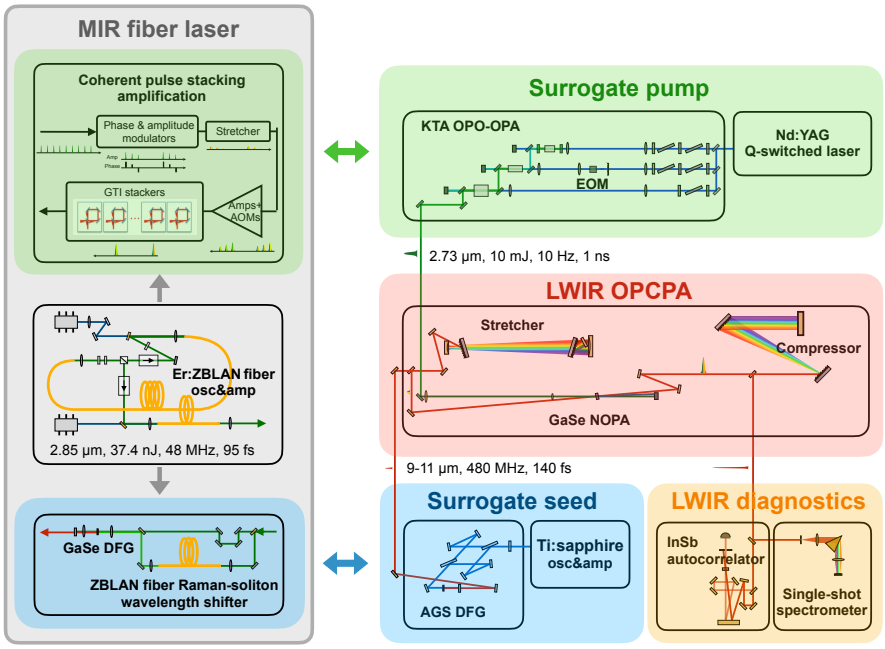

Figure 7.1: Diagram of the current OPCPA testbed using the surrogate pump and seed sources, and a concept for future integration with the MIR fiber-based sources [211,212].

Figure 7.1 also shows the roadmap to the future integration with the MIR Er:ZBLAN fiber laser-based pump and seed sources for scaling of the OPCPA architecture to high peak and average power. An Er:ZBLAN fiber mode-locked oscillator and a nonlinear amplifier/compressor have been developed. This source has enabled a generation of an ultrashort pulse train with 95 fs pulse duration, 37.4 nJ pulse energy, and 48 MHz repetition rate [211]. On the one side, the pulse train can be stacked coherently in a series of Gires-Tournois interferometers via the CPS amplification [136,212], generating MIR pulses targeting 1.2–1.5 J pulse energy in 1-ns pulse duration at a kHz repetition rate. The coherently combined MIR fiber laser can be used to replace the surrogate parametric pump, which would allow development of the LWIR OPCPA at high average powers. While this dissertation has numerically analyzed important

characteristics, such as gain and bandwidth, of the nonlinear materials in OPCPA for few-cycle LWIR pulse generation, simulation of the high-average-power performance of such OPCPA needs to be performed to better guide the future experimental demonstration by using the kHz-level MIR fiber pump laser. On the other side, the ∼2.8-µm pulses from the Er:ZBLAN fiber oscillator and amplifier can be sent through a ZBLAN fiber Raman-soliton wavelength shifter to generate the ∼3.5-µm signal for DFG in GaSe with the fundamental pulses. The fiber-based LWIR DFG source could replace the surrogate seed in the future. In addition to the currently pursued spectral and autocorrelation measurements, a complete characterization of the generated few-cycle LWIR pulses should be performed via techniques such as XFROG [213].

APPENDIX A

Single-shot MIR Spectrometers

Unlike monochromators such as the one described in Chapter 4, single-shot instruments can significantly reduce the measurement time and better resolve the potential spectral structures of the broadband signal that could be erased by the shot-to-shot instability of the laser. A pyroelectric linear array sensor (Pyroes, PY0723) integrated with a data acquisition board (Pyroes, PY0429) has been used for the development of single-shot spectrometers. The sensor has 128 pixels with a pitch width of 100 µm. Its spectral response is relatively uniform across the wavelength of interest, and the linearity is relatively good with an incident energy of ∼0.1–30 µJ. In Section A.1, the prism-based single-shot MIR spectrometer is discussed based on design in Ref. [214]. The grating-based single-shot spectrometer, which is discussed in Section A.2, is developed with the intent to obtain higher spectral resolution in the LWIR range than the prism-based one.

A.1 MIR prism-based spectrometer

Figure A.1a shows the experimental setup of the prism-based spectrometer. An f/3, 75-mm focal length ZnSe lens (Thorlabs, LA7660-E3) is used to collimate the focused MIR radiation from the slit. A dispersive ZnSe prism is then used to split the light into constituent wavelengths. The ZnSe prism used is a 20×15×10 mm^3 Brewster prism. The incident beam needs to have horizontal polarization so that the Fresnel

losses from the prism surfaces can be minimized. The refracted beam is collected and focused by another f/3, 75-mm ZnSe lens onto the array sensor. To minimize chromatic dispersion, the sensor is tilted at an angle of ∼15°. The prism spectrometer is aligned using a CO_2 laser.

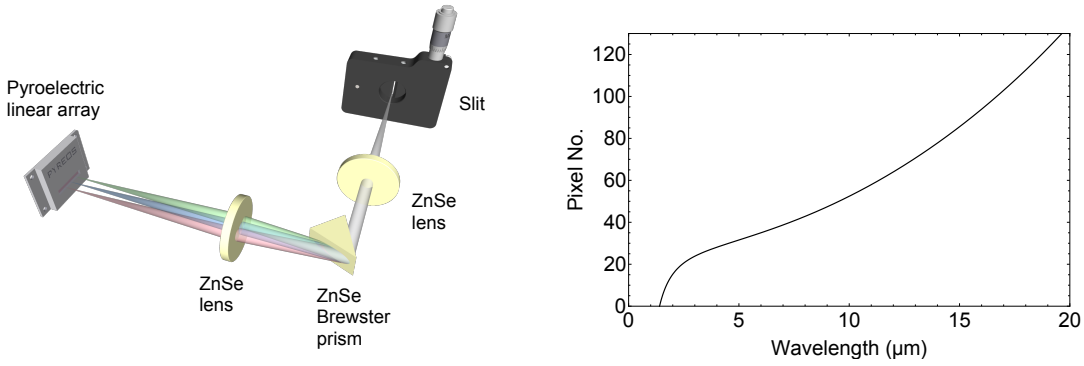

(a) (b)

Figure A.1: (a) Schematic diagram of the experimental setup of the LWIR prism spectrometer and (b) calculated wavelength-to-pixel mapping of the prism spectrometer.

The wavelength-to-pixel mapping of the prism spectrometer is calculated by using Snell's law and the Sellmeier equation [215], and is shown in Figure A.1b. Based on the calculation, wavelengths shorter than ∼750 nm experience total internal reflection inside the prism, and thus the pump and the seed can still possibly hit the sensor. To avoid exposing the sensor to the pump and the seed and also to fully cover the LWIR range of interest, the array is centered at ∼12 μm, giving a spectral coverage in the range of ∼1.4–20 μm as shown in Figure A.1b. The dependence of wavelength on pixel number is nonlinear, especially at the shorter wavelength side. However, a relatively more linear dependence can be obtained in the LWIR region. The spectral resolution of the prism spectrometer is estimated to be ∼189 nm at 10 μm.

A.2 LWIR Littrow grating spectrometer

As shown in Figure A.2a, the LWIR grating-based spectrometer uses a Littrow configuration, in which the first-order diffracted light propagates back along the incident beam direction. In the setup, the light that is focused on the slit is collected by an f/6, 149-mm ZnSe lens (Thorlabs, LA7028-E3). A 75 lines/mm, 25.0×12.5 mm^2 ruled grating (Thorlabs, GR1325-07106) blazed at 10.6 µm is positioned after the lens and is tilted to refract the light back above the center of the lens axis for ∼3 mm. A D-shaped pickoff mirror is used to direct the spectrum 90° onto the Pyroelectric linear array.

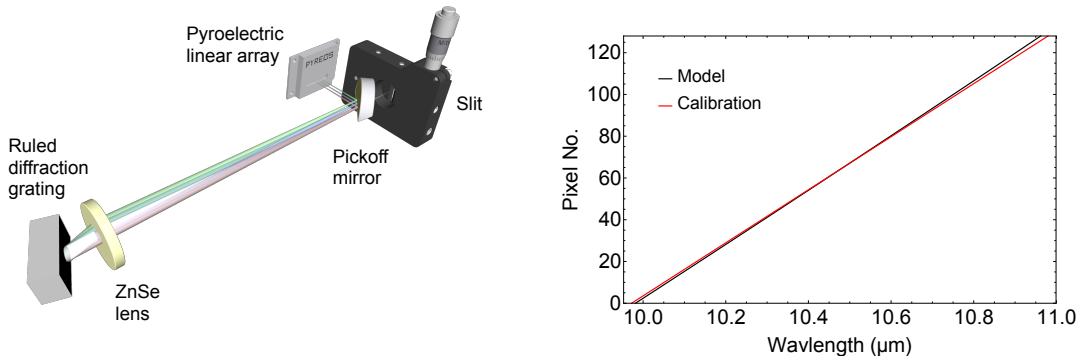

(a) (b)

Figure A.2: (a) Schematic diagram of the experimental setup of the LWIR grating spectrometer and (b) calculated wavelength-to-pixel mapping of the grating spectrometer.

Figure A.2b shows the calculated wavelength-to-pixel mapping of the grating spectrometer based on the general grating equation and Snell's law. Unlike the prism-based spectrometer, a linear dependence of the wavelength to the pixel number can be seen. The spectrometer has a 1 µm spectral coverage that is centered at 10.5 µm. Calibration of the spectrometer was performed using the two ammonia absorption lines at 10.35 µm and 10.72 µm [216]. As shown in Figure A.2b, the calibration matches well with the model. The total FWHM width of the instrumental line profile

is estimated to be ∼15 nm, considering the effects introduced by the grating, the spatial resolution of the detector, the entrance slit width, and the focal spot size. Specifically, the spectrometer has a resolving power of 1875, corresponding to a grating resolution of 5.3 nm at the central wavelength of 10 µm. The pixel pitch of 100 µm of the array sensor and the slit width of ∼100 µm contribute another ∼12.4 nm. The focal spot size of ∼73 µm corresponds to a contribution of 6.5 nm.

APPENDIX B

Ultrashort LWIR Pulse Characterization

Despite the fact that modern photodetectors have much improved performance in terms of their response time, their speed is at best several orders of magnitude slower than ultrashort pulses. Our MCT photodetector is only sufficient to measure LWIR pulses in the nanosecond temporal range. For picosecond pulse characterization in the LWIR regime, streak camera can be used accompanying with a CS_2 Kerr switch, such that the intense LWIR pulses are used as the pump for gating a red diode laser which lies in the sensitive spectral region of the streak camera [4]. For femtosecond LWIR pulse characterization, there are no commercial solutions available. Intensity autocorrelation [5,72,217] and XFROG [36,213] are the approaches that have successfully been transferred to LWIR region. In Section B.1, autocorrelation based on SHG and TPA in the LWIR region is introduced, and the InSb-based autocorrelator that has been developed is shown [179]. In Section B.2, the phase-sensitive XFROG measurement in the LWIR region is discussed, which will be implemented in the near feature [179].

B.1 Autocorrelation

The classical background-free intensity autocorrelation is the simplest technique to measure the pulse duration of an ultrashort pulse. In conventional autocorrelation, the ultrashort pulse is split into two replicas with a relative delay τ. The two replicas

are then focused and mixed in a fast-responding nonlinear crystal. The induced autocorrelation signal can then be conveniently singled out by an aperture. Different nonlinear effects, such as SHG and TPA, can be used in autocorrelation measurements. For the SHG case, the MIR cross-term signal ($E_2(t,\tau) \propto E(t)E(t-\tau)$) on the axis is selected via an aperture and is sent to a square-law photodetector, giving access to the autocorrelation function of the intensity envelope of the test pulse, which can be written as [218],

$$S(\tau) \propto \int |E_2(t,\tau)|^2 dt \propto \int I(t)I(t-\tau)dt. \tag{B.1}$$

Crystals such as AGSe [5] and GaSe [72] are good candidates for phase-matched SHG of the LWIR pulses. An alternative nonlinear process for autocorrelation measurement in the LWIR region is based on TPA in a bulk material. In such TPA case, the ultrashort pulse is split into a strong pump and a weak probe, which are then spatially overlapped in the medium. When temporally overlapped, the contribution of TPA with one photon from each beam creates the autocorrelation signal. The induced signal on the probe beam is selected and measured by a photodetector [219]. In the LWIR window, thin InSb crystals with a bandgap of 0.18 eV (λ=6.9 µm) and a dispersion length of ∼0.6–1 mm for 100-fs pulses could provide satisfactory performance for the autocorrelation measurement [217].

An InSb autocorrelator has been developed to provide simple pulse duration measurement of the generated LWIR pulses. A wedge ZnSe window (Thorlabs, WW70530-E3) is used to split a small part of the LWIR energy as the seed. A delay stage is built in the seed arm to ensure temporal overlapping of the seed with the pump in a 0.5-mm thick undoped InSb (110) crystal (MTI Corp.). The seed and the pump are spatially overlapped in the crystal at a small angle of ∼5°. The TPA of the seed is measured by the 400-MHz MCT detector. Figure B.1 shows the schematic diagram of the home-built InSb autocorrelator.

The autocorrelation function is symmetric in time and washes out structure in the

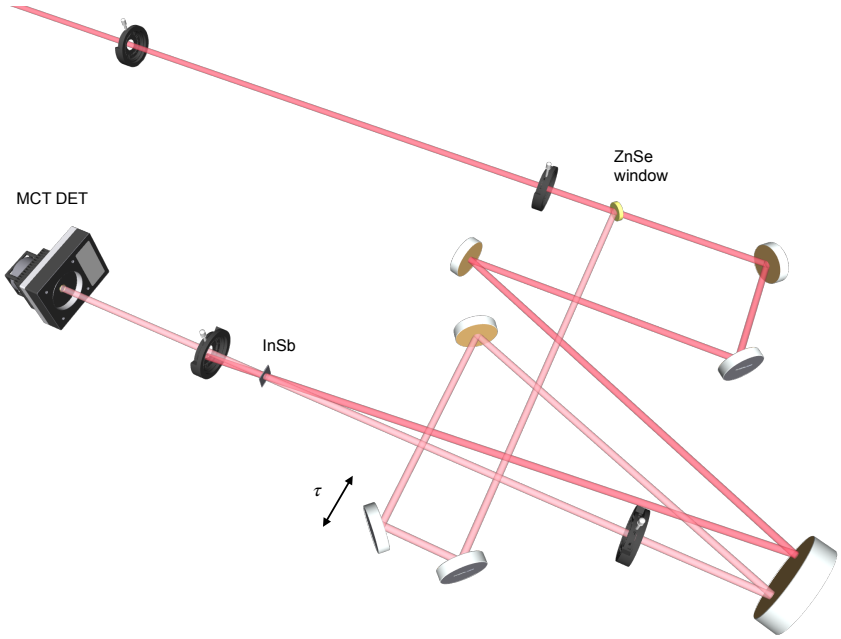

Figure B.1: Schematic diagram of the home-built InSb autocorrelator.

intensity profile. Intensity autocorrelation does not provide any phase information, but it provides a simple estimate of the pulse duration.

B.2 Cross-correlation frequency resolved optical gating

The intensity cross-correlation technique provides an alternative solution for pulse characterization by adopting an ancillary short gate pulse that is fully characterized instead of using the pulse itself, as in an autocorrelator. Cross-correlation measurements using 800-nm beam as the reference have been explored in the LWIR range using AGS crystal [63, 217]. The generated SFG signal thus lies conveniently in the visible to near-infrared spectral range. To provide additional phase sensitivity in the LWIR spectral range, XFROG arrangement is adopted by replacing the photodetector in the cross-correlation setup with a visible-to-near-infrared spectrometer, such that a spectrogram can be taken by recording spectrum versus delay. The 2D spectrogram

signal can be described as

$$S(\tau,\omega) \propto |\int E(t)E_g(t-\tau)e^{i\omega t}dt|^2, \tag{B.2}$$

where E_g is the electric field of the reference gate pulse. A fast iterative algorithm is usually used to retrieve the spectral phase and amplitude of the test pulse [218]. A XFROG device in 0.4-mm AGS has been recently developed and has demonstrated measurements of ∼85 fs pulses at a central wavelength of 8.9 µm [36]. However, GVM of short pulses in AGS is large, limiting the available bandwidth in the SFG process [217].

XFROG based on Four-Wave mixing (FWM) in air can enable intrinsically broadband characterization of few-cycle pulses in the LWIR range due to the weak dispersion of the rare gas medium [213]. The FWM process can convert 3–15 µm to a compact wavelength region of a few tens of nanometers in the visible spectral range (356–416 nm for sum-frequency FWM and 394–468 nm for difference-frequency FWM), where conventional spectrometers are available. The difference-frequency branch of FWM is used for better phase-matching and higher efficiency than its sum-frequency counterparts. Such FWM XFROG alleviates requirements on the nonlinear crystal in the standard XFROG and presents a promising solution for future few-cycle pulse characterization in the LWIR window that is away from the atmospheric molecular absorption bands.

APPENDIX C

Ray-tracing Model

A ray-tracing model used to analyze the stretcher and compressor is based on an extension of the ABCD matrix model and only considers a single transverse dimension. The model describes each optical element in the system using an operator. The deviation from a reference ray in terms of transverse position, angle, and phase as a function of wavelength is propagated through the system [185], which is represented by a vector:

$$\vec{V}(\lambda) = \begin{pmatrix} \delta\theta(\lambda) \\ \delta x(\lambda) \\ \delta\phi(\lambda) \end{pmatrix}. \tag{C.1}$$

The operator for free space propagation through a medium with refractive index $n(\lambda)$ over a distance L is

$$\vec{F}(L) = \begin{pmatrix} \delta\theta_{in}(\lambda) \\ \delta x_{in}(\lambda) + L\ \tan\delta\theta_{in}(\lambda) \\ \delta\phi_{in}(\lambda) + \frac{2\pi}{\lambda}\ L\ \cos\delta\theta_{in}(\lambda) \end{pmatrix}. \tag{C.2}$$

The operator used to describe the grating with groove spacing of d is

$$\vec{G}(\theta_{0,in}) = \begin{pmatrix} f(\theta_{0,in} + \delta\theta_{in}(\lambda)) - f(\theta_{0,in}) \\ \delta x_{in} \frac{\frac{1}{\cos\theta_{0,in}} + \frac{\tan\theta_{0,in}\sin\delta\theta_{in}(\lambda)}{\cos(\theta_{0,in}+\delta\theta_{in}(\lambda))}}{\frac{1}{\cos(f(\theta_{0,in}))} + \frac{\tan(f(\theta_{0,in}))\sin(f(\theta_{0,in}+\delta\theta_{in}(\lambda))-f(\theta_{0,in}))}{\cos(f(\theta_{0,in}+\delta\theta_{in}(\lambda)))}} \\ \delta\phi_{in}(\lambda) \end{pmatrix}, \tag{C.3}$$

where $\theta_{0,in}$ is the input angle of the reference ray, and the angle transformation of the grating is

$$f(\theta) = \arcsin\left(\frac{\lambda}{d} - \sin\theta_{in}\right). \tag{C.4}$$

For a spherical mirror with reference ray on the optical axis and a radius of curvature of R, the operator is given by

$$\vec{S}_{onaxis}(R) = \begin{pmatrix} \delta\theta_{in}(\lambda) + 2\arctan(\delta x_{in}(\lambda)/R) \\ \delta x_{in}(\lambda) \\ \delta\phi_{in}(\lambda) + \frac{2\pi}{\lambda} 2R\sqrt{1 - \sin^2\left(\arctan\frac{\delta x_{in}(\lambda)}{R}\right)} \end{pmatrix}. \tag{C.5}$$

BIBLIOGRAPHY

[1] D. Strickland and G. Mourou. Compression of amplified chirped optical pulses. *Optics Communications*, 55(6):447–449, 1985.

[2] P. F. Moulton. Spectroscopic and laser characteristics of Ti:Al_2O_3. *Journal of the Optical Society of America B*, 3(1):125, 1986.

[3] C. N. Danson, C. Haefner, J. Bromage, T. Butcher, J. F. Chanteloup, E. A. Chowdhury, A. Galvanauskas, L. A. Gizzi, J. Hein, D. I. Hillier, N. W. Hopps, Y. Kato, E. A. Khazanov, R. Kodama, G. Korn, R. X. Li, Y. T. Li, J. Limpert, J. G. Ma, C. H. Ham, D. Neely, D. Papadopoulos, R. R. Penman, L. J. Qian, J. J. Rocca, A. A. Shaykin, C. W. Siders, C. Spindloe, S. Szatmari, R. M. G. M. Trines, J. Q. Zhu, P. Zhu, and J. D. Zuegel. Petawatt and exawatt class lasers worldwide. *High Power Laser Science and Engineering*, 7(54):1–54, 2019.

[4] D. Haberberger, S. Tochitsky, and C. Joshi. Fifteen terawatt picosecond CO_2 laser system. *Optics Express*, 18(17):17865, 2010.

[5] M. N. Polyanskiy, I. V. Pogorelsky, M. Babzien, and M. A. Palmer. Demonstration of a 2 ps, 5 TW peak power, long-wave infrared laser based on chirped-pulse amplification with mixed-isotope CO_2 amplifiers . *OSA Continuum*, 3(3):459, 2020.

[6] V. Petrov. Parametric down-conversion devices: the coverage of the mid-infrared spectral range by solid-state laser sources. *Optical Materials*, 34(3):536–554, 2012.

[7] V. Petrov. Frequency down-conversion of solid-state laser sources to the mid-infrared spectral range using non-oxide nonlinear crystals. *Progress in Quantum Electronics*, 42:1–106, 2015.

[8] H. Pires, M. Baudisch, D. Sanchez, M. Hemmer, and J. Biegert. Ultrashort pulse generation in the mid-IR. *Progress in Quantum Electronics*, 43:1–30, 2015.

[9] B. Wolter, M. G. Pullen, M. Baudisch, M. Sclafani, M. Hemmer, A. Senftleben, C. D. Schröter, J. Ullrich, R. Moshammer, and J. Biegert. Strong-field physics with mid-IR fields. *Physical Review X*, 5(2):021034, 2015.

[10] D. Woodbury, L. Feder, V. Shumakova, C. Gollner, R. Schwartz, B. Miao, F. Salehi, A. Korolov, A. Pugžlys, A. Baltuška, and H. M. Milchberg. Laser wakefield acceleration with mid-IR laser pulses. *Optics Letters*, 43(5):1131–1134, mar 2018.

[11] A. V. Mitrofanov, A. A. Voronin, D. A. Sidorov-Biryukov, A. Pugžlys, E. A. Stepanov, G. Andriukaitis, T. Flöry, S. Ališauskas, A. B. Fedotov, A. Baltuška, and A. M. Zheltikov. Mid-infrared laser filaments in the atmosphere. *Scientific Reports*, 5(1):8368, 2015.

[12] S. Z. Qu, H. K. Liang, K. Liu, X. Zou, W. K. Li, Q. J. Wang, and Y. Zhang. 9 µm few-cycle optical parametric chirped-pulse amplifier based on $LiGaS_2$. *Optics Letters*, 44(10):2422, may 2019.

[13] I. Pupeza, D. Sánchez, J. Zhang, N. Lilienfein, M. Seidel, N. Karpowicz, T. Paasch-Colberg, I. Znakovskaya, M. Pescher, W. Schweinberger, V. Pervak, E. Fill, O. Pronin, Z. Wei, F. Krausz, A. Apolonski, and J. Biegert. High-power sub-two-cycle mid-infrared pulses at 100 MHz repetition rate. *Nature Photonics*, 9(11):721–724, nov 2015.

[14] C. L. Felix, W. W. Bewley, I. Vurgaftman, J. R. Lindle, J. R. Meyer, H. Z. Wu, G. Xu, S. Khosravani, and Z. Shi. Low-threshold optically pumped λ=4.4 μm vertical-cavity surface-emitting laser with a PbSe quantum-well active region. *Applied Physics Letters*, 78(24):3770–3772, 2001.

[15] A. K. Wójcik, P. Malara, R. Blanchard, T. S. Mansuripur, F. Capasso, and A. Belyanin. Generation of picosecond pulses and frequency combs in actively mode locked external ring cavity quantum cascade lasers. *Applied Physics Letters*, 103(23):231102, 2013.

[16] P. Malevich, G. Andriukaitis, T. Flöry, A. J. Verhoef, A. Fernández, S. Ališauskas, A. Pugžlys, A. Baltuška, L. H. Tan, C. F. Chua, and P. B. Phua. High energy and average power femtosecond laser for driving mid-infrared optical parametric amplifiers. *Optics Letters*, 38(15):2746, 2013.

[17] U. Elu, T. Steinle, D. Sánchez, L. Maidment, K. Zawilski, P. Schunemann, U. D. Zeitner, C. Simon-Boisson, and J. Biegert. Table-top high-energy 7 µm OPCPA and 260 mJ Ho: YLF pump laser. *Optics letters*, 44(13):3194–3197, 2019.

[18] L. von Grafenstein, M. Bock, D. Ueberschaer, K. Zawilski, P. G. Schunemann, U. Griebner, and T. Elsaesser. 5 µm few-cycle pulses with multi-gigawatt peak power at a 1 kHz repetition rate. *Optics Letters*, 42(19):3796–3799, 2017.

[19] M. Hemmer, D. Sánchez, M. Jelínek, V. Smirnov, H. Jelinkova, V. Kubeček, and J. Biegert. 2-µm wavelength, high-energy Ho:YLF chirped-pulse amplifier for mid-infrared OPCPA. *Optics Letters*, 40(4):451, 2015.

[20] T. Hu, S. D. Jackson, and D. D. Hudson. Ultrafast pulses from a mid-infrared fiber laser. *Optics Letters*, 40(18):4226, 2015.

[21] W. Du, X. Xiao, Y. Cui, J. Nees, I. Jovanovic, and A. Galvanauskas. Demonstration of 0.67-mJ and 10-ns high-energy pulses at 2.72 µm from large core Er: ZBLAN fiber amplifiers. *Optics Letters*, 45(19):5538–5541, 2020.

[22] E. ueni Slobodtchikov and P. F. Moulton. Progress in ultrafast Cr: ZnSe lasers. In *Advanced Solid-State Photonics*, pages AW5A–4. Optical Society of America, 2012.

[23] N. Myoung, D. V. Martyshkin, V. V. Fedorov, and S. B. Mirov. Energy scaling of 4.3 µm room temperature Fe: ZnSe laser. *Optics Letters*, 36(1):94–96, 2011.

[24] S. B. Mirov, I. S. Moskalev, S. Vasilyev, V. Smolski, V. V. Fedorov, D. Martyshkin, J. Peppers, M. Mirov, A. Dergachev, and V. Gapontsev. Frontiers of mid-IR lasers based on transition metal doped chalcogenides. *IEEE Journal of Selected Topics in Quantum Electronics*, 24(5):1–29, 2018.

[25] E. Migal, A. Pushkin, B. Bravy, V. Gordienko, N. Minaev, A. Sirotkin, and F. Potemkin. 3.5-mJ 150-fs Fe:ZnSe hybrid mid-IR femtosecond laser at 4.4 µm for driving extreme nonlinear optics. *Optics Letters*, 44(10):2550, may 2019.

[26] C. Rolland and P. B. Corkum. Generation of 130-fsec midinfrared pulses. *Journal of the Optical Society of America B*, 3(12):1625, 1986.

[27] C. V. Filip, R. Narang, S. Y. Tochitsky, C. E. Clayton, and C. Joshi. Optical Kerr switching technique for the production of a picosecond, multiwavelength CO_2 laser pulse. *Applied Optics*, 41(18):3743, 2002.

[28] A. J. Alcock and A. C. Walker. Generation and detection of 150-psec mode-locked pulses from a multi-atmosphere CO_2 laser. *Applied Physics Letters*, 25(5):299–301, 1974.

[29] R. Kesselring, A. W. Kälin, H. J. Schötzau, and Fritz K. Kneubühl. Picosecond CO_2 laser-pulse generation and amplification. *IEEE Journal of Quantum Electronics*, 29(3):997–1005, 1993.

[30] D. Tovey, S. Y. Tochitsky, J. J. Pigeon, G. J. Louwrens, M. N. Polyanskiy, I. Ben-Zvi, and C. Joshi. Multi-atmosphere picosecond CO_2 amplifier optically pumped at 4.3 µm. *Applied Optics*, 58(21):5756, 2019.

[31] Y. L. Cui, W. Huang, Z. F. Wang, M. L. Wang, Z. Y. Zhou, Z. X. Li, S. F. Gao, Y. Y. Wang, and P. Wang. 4.3 µm fiber laser in CO_2-filled hollow-core silica fibers. *Optica*, 6(8):951, 2019.

[32] B. W. Mayer, C. R. Phillips, L. Gallmann, and U. Keller. Mid-infrared pulse generation via achromatic quasi-phase-matched OPCPA. *Optics Express*, 22(17):20798, 2014.

[33] K. Zhao, H. Z. Zhong, P. Yuan, G. Q. Xie, J. Wang, J. G. Ma, and L. J. Qian. Generation of 120 GW mid-infrared pulses from a widely tunable noncollinear optical parametric amplifier. *Optics Letters*, 38(13):2159, 2013.

[34] M. Bock, L. von Grafenstein, U. Griebner, and T. Elsaesser. Generation of millijoule few-cycle pulses at 5 µm by indirect spectral shaping of the idler in an optical parametric chirped pulse amplifier. *Journal of the Optical Society of America B*, 35(12):C18, 2018.

[35] D. Sanchez, M. Hemmer, M. Baudisch, S. L. Cousin, K. Zawilski, P. Schunemann, O. Chalus, C. Simon-Boisson, and J. Biegert. 7 µm, ultrafast, sub-millijoule-level mid-infrared optical parametric chirped pulse amplifier pumped at 2 µm. *Optica*, 3(2):147, 2016.

[36] D. J. Wilson, A. M. Summers, S. Zigo, B. Davis, S. J. Robatjazi, J. A. Powell, D. Rolles, A. Rudenko, and C. A. Trallero-Herrero. An intense, few-cycle source in the long-wave infrared. *Scientific Reports*, 9(1):6002, 2019.

[37] M. Baudisch, H. Pires, H. Ishizuki, T. Taira, M. Hemmer, and J. Biegert. Sub-4-optical-cycle, 340 MW peak power, high stability mid-IR source at 160 kHz. *Journal of Optics*, 17(9):094002, 2015.

[38] O. Chalus, P. K. Bates, M. Smolarski, and J. Biegert. Ultrashort mid-IR OPCPA with micro-joule energy at 100 kHz. *Advanced Solid-State Photonics*, 17(5):MF10, 2009.

[39] C. J. Gerritsma and J. H. Haanstra. Infrared transmission of air under laboratory conditions. *Infrared Physics*, 10(2):79–90, 1970.

[40] B. Hassler. Atmospheric transmission models for infrared wavelengths. *Linköping University, Linköping*, 1998.

[41] S. D. Lord. *A new software tool for computing Earth's atmospheric transmission of near-and far-infrared radiation.* Ames Research Center, 1992.

[42] M. N. Polyanskiy, M. Babzien, and I. V. Pogorelsky. BESTIA (Brookhaven Experimental Supra-Terawatt Infrared at ATF) laser: a status report. *AIP Conference Proceedings*, 1812(1):110007, 2017.

[43] D. Tovey, J. J. Pigeon, S. Y. Tochitsky, G. Louwrens, and C. Joshi. Observation of high gain in a CO_2 amplifier pumped by a 4.3 µm laser. In *CLEO: Science and Innovations*, pages SM3E–3. Optical Society of America, 2020.

[44] U. Elu, T. Steinle, D. Sánchez, L. Maidment, K. Zawilski, P. Schunemann, U. D. Zeitner, C. Simon-Boisson, and J. Biegert. Table-top high-energy 7 µm OPCPA and 260 mJ Ho:YLF pump laser. *Optics Letters*, 44(13):3194, jul 2019.

[45] K. Hong, J. T. Gopinath, D. Rand, A. M. Siddiqui, S. Huang, E. Li, B. J. Eggleton, J. D. Hybl, T. Y. Fan, and F. X. Kärtner. High-energy, kHz-repetition-rate, ps cryogenic Yb: YAG chirped-pulse amplifier. *Optics letters*, 35(11):1752–1754, 2010.

[46] Y. C. Yin, J. Li, X. M. Ren, Y. Wang, A. Chew, and Z. H. Chang. High-energy two-cycle pulses at 32 µm by a broadband-pumped dual-chirped optical parametric amplification. *Optics Express*, 24(22):24989, 2016.

[47] U. Elu, M. Baudisch, H. Pires, F. Tani, M. H. Frosz, F. Köttig, A. Ermolov, P. St.J. Russell, and J. Biegert. High average power and single-cycle pulses from a mid-IR optical parametric chirped pulse amplifier. *Optica*, 4(9):1024, 2017.

[48] P. F. Wang, Y. Y. Li, W. K. Li, H. P. Su, B. J. Shao, S. Li, C. Wang, D. Wang, R. R. Zhao, Y. J. Peng, Y. X. Leng, R. X. Li, and Z. Z. Xu. 26 mJ/100 Hz CEP-stable near-single-cycle 4 µm laser based on OPCPA and hollow-core fiber compression. *Optics Letters*, 43(9):2197, may 2018.

[49] H. K. Liang, P. Krogen, Z. Wang, H. Park, T. Kroh, K. Zawilski, P. Schunemann, J. Moses, L. F. Dimauro, F. X. Kärtner, and K. H. Hong. High-energy mid-infrared sub-cycle pulse synthesis from a parametric amplifier. *Nature Communications*, 8(1):141, 2017.

[50] T. Kanai, P. Malevich, S. S. Kangaparambil, K. Ishida, M. Mizui, K. Yamanouchi, H. Hoogland, R. Holzwarth, A. Pugzlys, and A. Baltuska. Parametric amplification of 100 fs mid-infrared pulses in $ZnGeP_2$ driven by a Ho:YAG chirped-pulse amplifier. *Optics Letters*, 42(4):683, feb 2017.

[51] J. W. Zhang, K. Fai Mak, N. Nagl, M. Seidel, D. Bauer, D. Sutter, V. Pervak, F. Krausz, and O. Pronin. Multi-mW, few-cycle mid-infrared continuum spanning from 500 to 2250 cm^{-1}. *Light: Science & Applications*, 7(2):17180–17180, feb 2018.

[52] M. Seidel, X. Xiao, S. A. Hussain, G. Arisholm, A. Hartung, K. T. Zawilski, P. G. Schunemann, F. Habel, M. Trubetskov, V. Pervak, P. Oleg, and K. Ferenc. Multi-watt, multi-octave, mid-infrared femtosecond source. *Science advances*, 4(4):eaaq1526, 2018.

[53] Alessio Gambetta, Nicola Coluccelli, Marco Cassinerio, Davide Gatti, Paolo Laporta, Gianluca Galzerano, and Marco Marangoni. Milliwatt-level frequency combs in the 8–14 µm range via difference frequency generation from an Er:fiber oscillator. *Optics Letters*, 38(7):1155, apr 2013.

[54] M. Beutler, I. Rimke, E. Büttner, P. Farinello, A. Agnesi, V. Badikov, D. Badikov, and V. Petrov. Difference-frequency generation of ultrashort pulses in the mid-IR using Yb-fiber pump systems and $AgGaSe_2$. *Optics Express*, 23(3):2730, feb 2015.

[55] M. Beutler, I. Rimke, E. Büttner, V. Badikov, and V. Petrov. Femtosecond mid-IR difference-frequency generation in $HgGa_2S_4$ from an 80 MHz optical parametric oscillator pumped at 800 nm. *Journal of the Optical Society of America B*, 33(11):D7, nov 2016.

[56] S. Vasilyev, I. S. Moskalev, V. O. Smolski, J. M. Peppers, M. Mirov, A. V. Muraviev, K. Zawilski, P. G. Schunemann, S. B. Mirov, K. L. Vodopyanov, and V. P. Gapontsev. Super-octave longwave mid-infrared coherent transients produced by optical rectification of few-cycle 25-µm pulses. *Optica*, 6(1):111, jan 2019.

[57] T. P. Butler, D. Gerz, C. Hofer, J. Xu, C. Gaida, T. Heuermann, M. Gebhardt, L. Vamos, W. Schweinberger, J. A. Gessner, T. Siefke, M. Heusinger, U. Zeitner, A. Apolonski, N. Karpowicz, J. Limpert, F. Krausz, and I. Pupeza. Watt-scale 50-MHz source of single-cycle waveform-stable pulses in the molecular fingerprint region. *Optics Letters*, 44(7):1730, apr 2019.

[58] C. Gaida, M. Gebhardt, T. Heuermann, F. Stutzki, C. Jauregui, J. Antonio-Lopez, A. Schülzgen, R. Amezcua-Correa, A. Tünnermann, I. Pupeza, and J. Limpert. Watt-scale super-octave mid-infrared intrapulse difference frequency generation. *Light: Science & Applications*, 7(1):94, dec 2018.

[59] K. Kaneshima, N. Ishii, K. Takeuchi, and J. Itatani. Generation of carrier-envelope phase-stable mid-infrared pulses via dual-wavelength optical parametric amplification. *Optics Express*, 24(8):8660, apr 2016.

[60] O. Novak, P. Krogen, T. Kroh, T. Mocek, F. X. Kaertner, and K. H. Hong. A femtosecond 8.5 µm source based on intrapulse difference-frequency generation of 2.1 µm pulses. In *High-Brightness Sources and Light-driven Interactions*, volume Part F87-M, page MW1C.4. OSA, 2018.

[61] F. Rotermund, V. Petrov, and F. Noack. Difference-frequency generation of intense femtosecond pulses in the mid-IR (4–12 μm) using $HgGa_2S_4$ and $AgGaS_2$. *Optics Communications*, 185(1-3):177–183, nov 2000.

[62] F. Seifert, V. Petrov, and M. Woerner. Solid-state laser system for the generation of midinfrared femtosecond pulses tunable from 33 to 10 µm. *Optics Letters*, 19(23):2009, 1994.

[63] J. Song, J. F. Xia, Z. Zhang, and D. Strickland. Mid-infrared pulses generated from the mixing output of an amplified, dual-wavelength Ti:sapphire system. *Optics Letters*, 27(3):200, feb 2002.

[64] C. Erny and C. P. Hauri. Design of efficient single-stage chirped pulse difference frequency generation at 7 µm, driven by a dual wavelength Ti:sapphire laser. *Applied Physics B: Lasers and Optics*, 117(1):379–387, 2014.

[65] R. A. Kaindl, F. Eickemeyer, M. Woerner, and T. Elsaesser. Broadband phase-matched difference frequency mixing of femtosecond pulses in GaSe: Experiment and theory. *Applied Physics Letters*, 75(8):1060–1062, aug 1999.

[66] C. R. Petersen, U. Møller, I. Kubat, B. Zhou, S. Dupont, J. Ramsay, T. Benson, S. Sujecki, N. Abdel-Moneim, Z. Tang, D. Furniss, A. Seddon, and O. Bang. Mid-infrared supercontinuum covering the 1.4–13.3 µm molecular fingerprint region using ultra-high NA chalcogenide step-index fibre. *Nature Photonics*, 8(11):830–834, 2014.

[67] T. Cheng, K. Nagasaka, T. H. Tuan, X. J. Xue, M. Matsumoto, H. Tezuka, T. Suzuki, and Y. Ohishi. Mid-infrared supercontinuum generation spanning 20 to 151 µm in a chalcogenide step-index fiber. *Optics Letters*, 41(9):2117, 2016.

[68] K. W. Guo, R. A. Martinez, G. Plant, L. Maksymiuk, B. Janiszewski, M. J. Freeman, R. L. Maynard, M. N. Islam, F. L. Terry, R. Bedford, R. Gibson, F. Chenard, S. Chatigny, and A. I. Ifarraguerri. Generation of near-diffraction-limited, high-power supercontinuum from 1.57 µm to 12 µm with cascaded fluoride and chalcogenide fibers. *Applied Optics*, 57(10):2519, apr 2018.

[69] K. Liu, H. Liang, L. Wang, S. Qu, T. Lang, H. Li, Q. J. Wang, and Y. Zhang. Multimicrojoule GaSe-based midinfrared optical parametric amplifier with an ultrabroad idler spectrum covering 4.2–16 µm. *Optics Letters*, 44(4):1003, feb 2019.

[70] J. J. Pigeon, S. Y. Tochitsky, C. Gong, and C. Joshi. Supercontinuum generation from 2 to 20 µm in GaAs pumped by picosecond CO_2 laser pulses. *Optics Letters*, 39(11):3246, jun 2014.

[71] F. Silva, D. R. Austin, A. Thai, M. Baudisch, M. Hemmer, D. Faccio, A. Couairon, and J. Biegert. Multi-octave supercontinuum generation from mid-infrared filamentation in a bulk crystal. *Nature Communications*, 3(1):807, jan 2012.

[72] S. Z. Qu, G. Chaudhary Nagar, W. K. Li, K. Liu, X. Zou, S. Hon Luen, D. Dempsey, K. H. Hong, Q. Jie Wang, Y. Zhang, B. G. Shim, and H. K. Liang. Long-wavelength-infrared laser filamentation in solids in the near-single-cycle regime. *Optics Letters*, 45(8):2175, apr 2020.

[73] S. V. Chekalin and V. P. Kandidov. From self-focusing light beams to femtosecond laser pulse filamentation. *Physics-Uspekhi*, 56(2):123–140, feb 2013.

[74] A. M. Zheltikov. Laser-induced filaments in the mid-infrared. *Journal of Physics B: Atomic, Molecular and Optical Physics*, 50(9):092001, may 2017.

[75] A. Couairon and A. Mysyrowicz. Femtosecond filamentation in transparent media. *Physics Reports*, 441(2-4):47–189, 2007.

[76] P. Whalen, P. Panagiotopoulos, M. Kolesik, and J. V. Moloney. Extreme carrier shocking of intense long-wavelength pulses. *Physical Review A*, 89(2):023850, 2014.

[77] P. Panagiotopoulos, P. Whalen, M. Kolesik, and J. V. Moloney. Super high power mid-infrared femtosecond light bullet. *Nature Photonics*, 9(8):543–548, 2015.

[78] P. Panagiotopoulos, K. Schuh, M. Kolesik, and J. V. Moloney. Simulations of 10 µm filaments in a realistically modeled atmosphere. *Journal of the Optical Society of America B*, 33(10):2154, oct 2016.

[79] P. Panagiotopoulos, P. Rosenow, M. Kolesik, S. W. Koch, K. Schuh, and E. W. Wright. Simulation of LWIR TW ultrashort pulses over kilometer ranges in the atmosphere. In Michael K. Rafailov, editor, *Ultrafast Bandgap Photonics III*, page 56. SPIE, may 2018.

[80] A. V. Mitrofanov, D. A. Sidorov-Biryukov, A. A. Voronin, A. Pugžlys, G. Andriukaitis, E. A. Stepanov, S. Ališauskas, T. Flöri, A. B. Fedotov, V. Y. Panchenko, A. Baltuška, and A. M. Zheltikov. Subterawatt femtosecond pulses in the mid-infrared range: new spatiotemporal dynamics of high-power electromagnetic fields. *Physics-Uspekhi*, 58(1):89–94, jan 2015.

[81] A. V. Mitrofanov, A. A. Voronin, D. A. Sidorov-Biryukov, S. I. Mitryukovsky, M. V. Rozhko, A. Pugžlys, A. B. Fedotov, V. Ya. Panchenko, A. Baltuška, and A. M. Zheltikov. Angle-resolved multioctave supercontinua from mid-infrared laser filaments. *Optics Letters*, 41(15):3479, aug 2016.

[82] S. Tochitsky, E. Welch, M. Polyanskiy, I. Pogorelsky, P. Panagiotopoulos, M. Kolesik, E. M. Wright, S. W. Koch, J. V. Moloney, J. Pigeon, and C. Joshi. Megafilament in air formed by self-guided terawatt long-wavelength infrared laser. *Nature Photonics*, 13(1):41–46, 2019.

[83] J. J. Pigeon, S. Ya Tochitsky, E. C. Welch, and C. Joshi. Measurements of the nonlinear refractive index of air, N_2, and O_2 at 10 µm using four-wave mixing. *Optics Letters*, 41(17):3924, sep 2016.

[84] J. J. Pigeon, S. Ya. Tochitsky, E. C. Welch, and C. Joshi. Experimental study of the third-order nonlinearity of atomic and molecular gases using 10-µm laser pulses. *Physical Review A*, 97(4):043829, apr 2018.

[85] S. Zahedpour, S. W. Hancock, and H. M. Milchberg. Ultrashort infrared 2.5–11 µm pulses: spatiotemporal profiles and absolute nonlinear response of air constituents. *Optics Letters*, 44(4):843, feb 2019.

[86] R. W. Boyd. *Nonlinear optics*. Academic press, 2019.

[87] P. A. Franken, A. E. Hill, C. W. Peters, and G. Weinreich. Generation of optical harmonics. *Physical Review Letters*, 7(4):118, 1961.

[88] R. L. Sutherland. *Handbook of nonlinear optics*. CRC press, 2003.

[89] Y. R. Shen. *The principles of nonlinear optics*. Wiley New York, 1984.

[90] A. Yariv and P. Yeh. *Optical waves in crystals*, volume 5. Wiley New York, 1984.

[91] J. A. Armstrong, N. Bloembergen, J. Ducuing, and P. S. Pershan. Interaction between light waves in a nonlinear dielectric. *Pysical Review*, 127(6):1918–1938, 1962.

[92] I. Jovanovic. *Optical parametric amplification for high peak and average power*. PhD thesis, University of California, Berkeley, January 2001.

[93] B. C. Stuart, M. D. Feit, A. M. Rubenchik, B. W. Shore, and M. D. Perry. Laser-induced damage in dielectrics with nanosecond to subpicosecond pulses. *Physical Review Letters*, 74(12):2248–2252, 1995.

[94] B. C. Stuart, M. D. Feit, S. Herman, A. M. Rubenchik, B. W. Shore, and M. D. Perry. Nanosecond-to-femtosecond laser-induced breakdown in dielectrics. *Physical Review B*, 53(4):1749–1761, jan 1996.

[95] L. Gallais, D.-B. Douti, M. Commandré, G. Batavičiūtė, E. Pupka, M. Ščiuka, L. Smalakys, V. Sirutkaitis, and A. Melninkaitis. Wavelength dependence of femtosecond laser-induced damage threshold of optical materials. *Journal of Applied Physics*, 117(22):223103, jun 2015.

[96] D. M. Simanovskii, H. A. Schwettman, H. Lee, and A. J. Welch. Midinfrared optical breakdown in transparent dielectrics. *Physical Review Letters*, 91(10):107601, sep 2003.

[97] C. Manzoni and G. Cerullo. Design criteria for ultrafast optical parametric amplifiers. *Journal of Optics*, 18(10):103501, oct 2016.

[98] G. Cerullo and S. De Silvestri. Ultrafast optical parametric amplifiers. *Review of Scientific Instruments*, 74(1):1–18, jan 2003.

[99] I. N. Ross, P. Matousek, G. H. C. New, and K. Osvay. Analysis and optimization of optical parametric chirped pulse amplification. *J. Opt. Soc. Am. B*, 19(12):2945–2956, 2002.

[100] J. Ma, J. Wang, P. Yuan, G. Xie, and L. Qian. Origin and suppression of back conversion in a phase-matched nonlinear frequency down-conversion process. *Chinese Optics Letters*, 15(2):021901–21904, 2017.

[101] T. Singh and M. R. Shenoy. Modeling and design of singly-resonant optical parametric oscillator with an intracavity idler absorber for enhanced conversion efficiency for the signal. *Journal of Nonlinear Optical Physics & Materials*, 26(03):1750030, sep 2017.

[102] G. Arisholm, Ø. Nordseth, and G. Rustad. Optical parametric master oscillator and power amplifier for efficient conversion of high-energy pulses with high beam quality. *Optics Express*, 12(18):4189, 2004.

[103] G. Porat, O. Gayer, and A. Arie. Simultaneous parametric oscillation and signal-to-idler conversion for efficient downconversion. *Optics Letters*, 35(9):1401, may 2010.

[104] Y. Duan, H. Zhu, C. Xu, X. Ruan, G. Cui, Y. Zhang, D. Tang, and D. Fan. Compact self-cascaded KTA-OPO for 26 µm laser generation. *Optics Express*, 24(23):26529, nov 2016.

[105] J. Zheng and H. Zacharias. Non-collinear optical parametric chirped-pulse amplifier for few-cycle pulses. *Applied Physics B: Lasers and Optics*, 97(4):765–779, 2009.

[106] X. D. Liu, L. Xu, and X. Y. Liang. Numerical investigation of output beam quality in efficient broadband optical parametric chirped pulse amplification. *Optics Communications*, 383:197–207, jan 2017.

[107] A. A. Voronin, A. A. Lanin, and A. M. Zheltikov. Modeling high-peak-power few-cycle field waveform generation by optical parametric amplification in the long-wavelength infrared. *Optics Express*, 24(20):23207, 2016.

[108] Y. C. Yin, A. Chew, X. M. Ren, J. Li, Y. Wang, Y. Wu, and Z. H. Chang. Towards terawatt sub-cycle long-wave infrared pulses via chirped optical parametric amplification and indirect pulse shaping. *Scientific Reports*, 7:45794, 2017.

[109] A. Dubietis, G. Jonušauskas, and A. Piskarskas. Powerful femtosecond pulse generation by chirped and stretched pulse parametric amplification in BBO crystal. *Optics Communications*, 88(4-6):437–440, 1992.

[110] I. N. Ross, J. L. Collier, P. Matousek, C. N. Danson, D. Neely, R. M. Allott, D. A. Pepler, C. Hernandez-Gomez, and K. Osvay. Generation of terawatt pulses by use of optical parametric chirped pulse amplification. *Applied Optics*, 39(15):2422, 2000.

[111] V. V. Lozhkarev, G. I. Freidman, V. N. Ginzburg, E. V. Katin, E. A. Khazanov, A. V. Kirsanov, G. A. Luchinin, A. N. Mal'shakov, M. A. Martyanov, O. V. Palashov, A.K. Poteomkin, A. M. Sergeev, A. A. Shaykin, and I. V. Yakovlev. 200 TW 45 fs laser based on optical parametric chirped pulse amplification. *Optics Express*, 14(1):446–454, 2006.

[112] V. V. Lozhkarev, G. I. Freidman, V. N. Ginzburg, E. V. Katin, E. A. Khazanov, A. V. Kirsanov, G. A. Luchinin, A. N. Mal'shakov, M. A. Martyanov, O. V. Palashov, A.K. Poteomkin, A. M. Sergeev, A. A. Shaykin, and I. V. Yakovlev. Compact 0.56 petawatt laser system based on optical parametric chirped pulse amplification in KD^*P crystals. *Laser Physics Letters*, 4(6):421, 2007.

[113] I. Jovanovic. *Optical parametric amplification for high peak and average power*. PhD thesis, University of California, Berkeley, 2001.

[114] P. G. Schunemann, K. T. Zawilski, L. A. Pomeranz, D. J. Creeden, and P. A. Budni. Advances in nonlinear optical crystals for mid-infrared coherent sources. *Journal of the Optical Society of America B*, 33(11):D36, 2016.

[115] A. V. Smith. SNLO nonlinear optics code. *Sandia National Laboratories, Albuquerque, NM*, 87185(1423):87, 2004.

[116] H. Kildal and J. C. Mikkelsen. The nonlinear optical coefficient, phasematching, and optical damage in the chalcopyrite $AgGaSe_2$. *Optics Communications*, 9(3):315–318, 1973.

[117] B. C. Ziegler and K. L. Schepler. Transmission and damage-threshold measurements in $AgGaSe_2$ at 2.1 µm. *Applied optics*, 30(34):5077–5080, 1991.

[118] P. A. Budni, M. G. Knights, E. P. Chicklis, and K. L. Schepler. Kilohertz $AgGaSe_2$ optical parametric oscillator pumped at 2 µm. *Optics letters*, 18(13):1068–1070, 1993.

[119] S. Haidar and H. Ito. Injection-seeded optical parametric oscillator for efficient difference frequency generation in mid-IR. *Optics communications*, 171(1-3):171–176, 1999.

[120] P. D. Mason and L. F. Michaille. Review of the development of nonlinear materials for mid-IR generation. In *Technologies for Optical Countermeasures V*, volume 7115, page 71150N. International Society for Optics and Photonics, 2008.

[121] D. N. Nikogosyan. *Nonlinear optical crystals: a complete survey*. Springer Science & Business Media, 2006.

[122] G. B. Abdullaev, L. A. Kulevskiĭ, P. V. Nikles, A. M. Prokhorov, A. D. Savel'ev, E. Y. Salaev, and V. V. Smirnov. Difference frequency generation in a GaSe crystal with continuous tuning in the 560–1050 cm_{-1} range. *Soviet Journal of Quantum Electronics*, 6(1):88, 1976.

[123] K. L. Vodopyanov, S. B. Mirov, V. G. Voevodin, and P. G. Schunemann. Two-photon absorption in GaSe and $CdGeAs_2$. *Optics Communications*, 155(1-3):47–50, 1998.

[124] A. O. Okorogu, S. B. Mirov, W. Lee, D. I. Crouthamel, N. Jenkins, A. Y. Dergachev, K.L. Vodopyanov, and V. V. Badikov. Tunable middle infrared downconversion in GaSe and $AgGaS_2$. *Optics communications*, 155(4-6):307–312, 1998.

[125] V. Petrova, V. L. Panyutina, A. Tyazheva, G. Marcheva, A. I. Zagumennyib, F. Rotermunda, F. Noacka, K. Miyataa, L. D. Iskhakovab, and A. F. Zerroukd. $GaS_{0.4}Se_{0.6}$: Relevant Properties and Potential for 1064 nm Pumped Mid-IR OPOs and OPGs Operating above 5 µm. *Laser Physics*, 21(4), 2011.

[126] P. G. Schunemann, S. D. Setzler, L. Mohnkern, T. M. Pollak, D. F. Bliss, D. Weyburne, and K. O'Hearn. 2.05-μm-laser-pumped orientation-patterned gallium arsenide (OPGaAs) OPO. In *Conference on Lasers and Electro-Optics*, page CThQ4. Optical Society of America, 2005.

[127] D. Faye, E. Lallier, A. Grisard, B. Gérard, C. Kieleck, and A. Hirth. High efficiency mid-infrared OPO based on low-loss orientation-patterned GaAs samples (OP-GaAs). In *Nonlinear Frequency Generation and Conversion: Materials, Devices, and Applications VII*, volume 6875, page 68750G. International Society for Optics and Photonics, 2008.

[128] C. Kieleck, M. Eichhorn, A. Hirth, D. Faye, and E. Lallier. High-efficiency 20–50 kHz mid-infrared orientation-patterned GaAs optical parametric oscillator pumped by a 2 µm holmium laser. *Optics Letters*, 34(3):262–264, 2009.

[129] M. Favier, B. Faure, G. Souhaité, J. Melkonian, A. Godard, M. Raybaut, A. Grisard, and E. Lallier. Compact tunable laser source emitting in the LWIR for standoff gas sensing. In *OPTRO 2020*, 2020.

[130] R. A. Fisher and W. K. Bischel. Numerical studies of the interplay between self-phase modulation and dispersion for intense plane-wave laser pulses. *Journal of Applied Physics*, 46(11):4921–4934, 1975.

[131] K. L. Vodopyanov. Parametric generation of tunable infrared radiation in $ZnGeP_2$ and GaSe pumped at 3 µm. *Journal of the Optical Society of America B*, 10(9):1723, sep 1993.

[132] K. Kato, F. Tanno, and N. Umemura. Sellmeier and thermo-optic dispersion formulas for GaSe (Revisited) *. *Applied Optics*, 52(11):2325–2328, 2013.

[133] T. Skauli, P. S. Kuo, K. L. Vodopyanov, T. J. Pinguet, O. Levi, L. A. Eyres, J. S. Harris, M. M. Fejer, B. Gerard, L. Becouarn, and E. Lallier. Improved dispersion relations for GaAs and applications to nonlinear optics. *Journal of Applied Physics*, 94(10):6447–6455, nov 2003.

[134] T. Skauli, K. L. Vodopyanov, T. J. Pinguet, A. Schober, O. Levi, L. A. Eyres, M. M. Fejer, J. S. Harris, B. Gerard, L. Becouarn, E. Lallier, and G. Arisholm. Measurement of the nonlinear coefficient of orientation-patterned GaAs and demonstration of highly efficient second-harmonic generation. *Optics Letters*, 27(8):628, apr 2002.

[135] Y. Shen, Y. Wang, F. Zhu, L. Ma, L. Zhao, Z. Chen, H. Wang, C. Huang, K. Huang, and G. Feng. 200 µJ, 13 ns Er:ZBLAN mid-infrared fiber laser

actively Q-switched by an electro-optic modulator. *Optics Letters*, 46(5):1141, mar 2021.

[136] T. Zhou, J. Ruppe, C. Zhu, I. Hu, J. Nees, and A. Galvanauskas. Coherent pulse stacking amplification using low-finesse gires-tournois interferometers. *Optics Express*, 23(6):7442, mar 2015.

[137] X. Xiao, J. A. Nees, and I. Jovanovic. High-energy nanosecond parametric source at 2.7 µm. *Appl. Opt.*, 60(13):3585–3590, May 2021.

[138] G. Hansson, H. Karlsson, S. Wang, and F. Laurell. Transmission measurements in KTP and isomorphic compounds. *Applied Optics*, 39(27):5058, sep 2000.

[139] W. R. Bosenberg, L. K. Cheng, and J. D. Bierlein. Optical parametric frequency conversion properties of $KTiOAsO_4$. *Applied Physics Letters*, 65(22):2765–2767, nov 1994.

[140] G. Vysniauskas, D. Burns, and E. Bente. Development of a nanosecond high energy KTA OPO system operating 2.9 µm. In *Conference on Lasers and Electro-Optics*, page CWA28. Optical Society of America, 2002.

[141] D. L. Fenimore, K. L. Schepler, U. B. Ramabadran, and S. R. McPherson. Infrared corrected sellmeier coefficients for potassium titanyl arsenate. *Journal of the Optical Society of America B*, 12(5):794, may 1995.

[142] R. L. Phillips, L. C. Andrews, J. Stryjewski, B. Griffis, M. Borbath, D. Galus, G. Burdge, K. Green, C. Kim, D. Stack, C. Harkrider, D. Wayne, D. Hand, and J. Kiriazes. Beam wander experiments: terrestrial path. In *Atmospheric Optical Modeling, Measurement, and Simulation II*, volume 6303, page 630306, aug 2006.

[143] R. L. Schmitt and L. A. Rahn. Diode-laser-pumped Nd:YAG laser injection seeding system. *Applied Optics*, 25(5):629–633, 1985.

[144] V. Evtuhov and A. E. Siegman. A "twisted-mode" technique for obtaining axially uniform energy density in a laser cavity. *Applied Optics*, 4(1):142—-143, 1965.

[145] T. J. Kane and R. L. Byer. Monolithic, unidirectional single-mode Nd:YAG ring laser. *Optics Letters*, 10(2):65–67, 1985.

[146] A. Caprara and G. C. Reali. Time-resolved M^2 of nanosecond pulses from a Q-switched variable-reflectivity-mirror Nd:YAG laser. *Optics Letters*, 17(6):414, mar 1992.

[147] G. Anstett, M. Nittmann, A. Borsutzky, and R. Wallenstein. Experimental investigation and numerical simulation of the spatio-temporal dynamics of nanosecond pulses in Q-switched Nd:YAG lasers. *Applied Physics B*, 76(8):833–838, jul 2003.

[148] R. F. Wu, K. S. Lai, H. Wong, W. J. Xie, Y. Lim, and E. Lau. Multiwatt mid-IR output from a Nd:YALO laser pumped intracavity KTA OPO. *Optics Express*, 8(13):694, 2001.

[149] X. L. Dong, B. T. Zhang, J. L. He, H. T. Huang, K. J. Yang, J. L. Xu, C. H. Zuo, S. Zhao, G. Qiu, and Z. K. Liu. High-power 1.5 and 3.4 µm intracavity KTA OPO driven by a diode-pumped Q-switched Nd:YAG laser. *Optics Communications*, 282(8):1668–1670, 2009.

[150] W. J. Sun, Q. P. Wang, Z. J. Liu, X. Y. Zhang, F. Bai, X. B. Wan, G. F. Jin, X. T. Tao, and Y. X. Sun. High efficiency $KTiOAsO_4$ optical parametric oscillator within a diode-side-pumped two-rod Nd:YAG laser. *Applied Physics B*, 104(1):87–91, jul 2011.

[151] F. Bai, Q. Wang, Z. Liu, X. Zhang, X. Wan, W. Lan, G. Jin, X. Tao, and Y. Sun. Theoretical and experimental studies on output characteristics of an intracavity KTA OPO. *Optics Express*, 20(2):807, jan 2012.

[152] F. Bai, Q. Wang, Z. Liu, X. Zhang, W. Lan, X. Tao, and Y. Sun. Idler-resonant optical parametric oscillator based on $KTiOAsO_4$. *Applied Physics B*, 112(1):83–87, aug 2013.

[153] K. Zhong, Y. Y. Wang, D. G. Xu, Y. F. Geng, J. L. Wang, P. Wang, and J. Q. Yao. Efficient electro-optic Q-switched eye-safe optical parametric oscillator based on $KTiAsO_4$. *Applied Physics B*, 97(1):61–66, sep 2009.

[154] K. Zhong, J. Q. Yao, D. G. Xu, J. L. Wang, J. S. Li, and P. Wang. High-pulse-energy high-efficiency mid-infrared generation based on KTA optical parametric oscillator. *Applied Physics B*, 100(4):749–753, sep 2010.

[155] Q. B. Sun, H. J. Liu, N. Huang, C. Ruan, S. L. Zhu, and W. Zhao. High energy and high efficiency 3.4 µm extracavity KTA optical parametric oscillator. *Laser Physics Letters*, 8(1):16–20, jan 2011.

[156] M. D. Wojcik. Eye-safe, 243-mJ, rapidly tuned by injection-seeding, near-infrared, optical, parametric, oscillator-based differential-absorption light detection and ranging transmitter. *Journal of Applied Remote Sensing*, 6(1):063510, mar 2012.

[157] D. J. Armstrong and A. V Smith. 150-mJ 1550-nm KTA OPO with good beam quality and high efficiency. In *Nonlinear Frequency Generation and Conversion: Materials, Devices, and Applications III*, volume 5337, pages 71–80. International Society for Optics and Photonics, 2004.

[158] H. Li, X. Zhu, X. Ma, S. Li, C. Huang, J. Zhang, and W. Chen. Narrowband optical parametric amplifier for efficient conversion of high-energy pulse with high beam quality. *Chinese Optics Letters*, 12(9):091401–91404, 2014.

[159] A. V. Smith and M. S. Bowers. Image-rotating cavity designs for improved beam quality in nanosecond optical parametric oscillators. *Journal of the Optical Society of America B*, 18(5):706, may 2001.

[160] A. V. Smith and D. J. Armstrong. Nanosecond optical parametric oscillator with 90° image rotation: design and performance. *Journal of the Optical Society of America B*, 19(8):1801, aug 2002.

[161] D. J. Armstrong and A. V. Smith. Demonstration of improved beam quality in an image-rotating optical parametric oscillator. *Optics Letters*, 27(1):40, jan 2002.

[162] R. S. Coetzee, X. Zheng, L. Fregnani, F. Laurell, and V. Pasiskevicius. Narrowband, tunable, 2-µm optical parametric master-oscillator power amplifier with large-aperture periodically poled Rb:KTP. *Applied Physics B: Lasers and Optics*, 124(6):1–8, 2018.

[163] International Organization for Standardization. Lasers and laser-related equipment–Test methods for laser beam widths, divergence angles and beam propagation ratios. ISO 11146, (Geneva, 2005).

[164] A. V. Smith, W. J. Alford, T. D. Raymond, and Mark S. Bowers. Comparison of a numerical model with measured performance of a seeded, nanosecond KTP optical parametric oscillator. *Journal of the Optical Society of America B*, 12(11):2253, nov 1995.

[165] A. E. Siegman. How to (maybe) measure laser beam quality. In *Diode Pumped Solid State Lasers: Applications and Issues*, page MQ1. Optical Society of America, 1998.

[166] J. Bromage, J. Rothhardt, S. Hädrich, C. Dorrer, C. Jocher, S. Demmler, J. Limpert, A. Tünnermann, and J. D. Zuegel. Analysis and suppression of parasitic processes in noncollinear optical parametric amplifiers. *Optics Express*, 19(18):16797–16808, 2011.

[167] D. N. Schimpf, J. Rothhardt, J. Limpert, A. Tünnermann, and D. C. Hanna. Theoretical analysis of the gain bandwidth for noncollinear parametric amplification of ultrafast pulses. *Journal of the Optical Society of America B*, 24(11):2837, 2007.

[168] L. Shen and D. Y. Fan. Theoretical research on noncollinear match conditions of the type I optical parametric process. *J. Opt. Soc. Am. B*, 24(1):90–93, 2007.

[169] V. V. Lozhkarev, G. I. Freidman, V. N. Ginzburg, E. A. Khazanov, O. V. Palashov, A. M. Sergeev, and I. V. Yakovlev. Study of broadband optical parametric chirped pulse amplification in a DKDP crystal pumped by the second harmonic of a Nd: YLF laser. *Laser Physics*, 15(9):1319–1333, 2005.

[170] T. Kobayashi and A. Shirakawa. Tunable visible and near-infrared pulse generator in a 5 fs regime. *Applied Physics B: Lasers and Optics*, 70(s1):239–246, 2000.

[171] S. Hädrich, S. Demmler, J. Rothhardt, C. Jocher, J. Limpert, and A. Tünnermann. High-repetition-rate sub-5-fs pulses with 12 GW peak power from fiber-amplifier-pumped optical parametric chirped-pulse amplification. *Optics Letters*, 36(3):313–315, 2011.

[172] J. Q. Zhu, X. L. Xie, M. Z. Sun, J. Kang, Q. W. Yang, A. L. Guo, H. D. Zhu, P. Zhu, Q. Gao, X. Liang, Z. R. Cui, S. H. Yang, C. Zhang, and Z. Q. Lin. Analysis and construction status of SG-II 5 PW laser facility. *High Power Laser Science and Engineering*, 6:e29, 2018.

[173] X. M. Zeng, K. N. Zhou, Y. L. Zuo, Q. H. Zhu, J. Q. Su, X. Wang, X. D. Wang, X. J. Huang, X. J. Jiang, D. B. Jiang, Y. Guo, N. Xie, S. Zhou, Z. H. Wu, J. Mu, H. Peng, and F. Jing. Multi-petawatt laser facility fully based on optical parametric chirped-pulse amplification. *Optics Letters*, 42(10):2014–2017, 2017.

[174] X. Y. Guo, Y. Xu, X. Zou, X. M. Lu, Y. Y. Li, C. Wang, Y. X. Leng, and R. X. Li. Non-collinear phase-matching geometries in optical parametric chirped-pulse amplification. *Optics Communications*, 330:24–29, 2014.

[175] X. D. Liu, L. Xu, and X. Y. Liang. Output features of optical parametric chirped pulse amplification in LiB_3O_5 near 800 nm at different phase-matching geometries. *Optics Letters*, 41(24):5809–5812, 2016.

[176] S. X. Dou, D. Josse, and J. Zyss. Comparison of collinear and one-beam noncritical noncollinear phase matching in optical parametric amplification. *Journal of the Optical Society of America B*, 9(8):1312–1319, 1992.

[177] E. Sorokin, G. Tempea, and T. Brabec. Measurement of the root-mean-square width and the root-mean-square chirp in ultrafast optics. *Journal of the Optical Society of America B*, 17(1):146, 2000.

[178] X. Xiao, J. Nees, H. Huang, A. Galvanauskas, and I. Jovanovic. Optical parametric amplification at 10.6 µm in gase pumped by a 2.75-µm parametric source. In *CLEO: Science and Innovations*, pages JTu2F–19. Optical Society of America, 2020.

[179] H. Huang. *Ultrashort long-wave-infrared pulse generationg using near-infrared frequency mixing (Unpublished doctoral dissertation)*. PhD thesis, University of Michigan, 2022.

[180] J. F. Xia, J. Song, and D. Strickland. Development of a dual-wavelength Ti:sapphire multi-pass amplifier and its application to intense mid-infrared generation. *Optics Communications*, 206(1-3):149–157, may 2002.

[181] H. Huang, X. Xiao, J. Nees, and I. Jovanovic. Genetic algorithm optimization for ultra-broadband long-wave infrared seed pulse generation. In *CLEO: Science and Innovations*, pages STu1D–7. Optical Society of America, 2021.

[182] E. Treacy. Optical pulse compression with diffraction gratings. *IEEE Journal of quantum Electronics*, 5(9):454–458, 1969.

[183] O. E. Martinez. Grating and prism compressors in the case of finite beam size. *Journal of the Optical Society of America B*, 3(7):929, jul 1986.

[184] I. V. Yakovlev. Stretchers and compressors for ultra-high power laser systems. *Quantum Electronics*, 44(5):393–414, may 2014.

[185] F. Druon, H. Marc, G. Lucas-Leclin, Y. Zaouter, D. Papadopoulos, and P. Georges. Simple and general method to calculate the dispersion properties of complex and aberrated stretchers-compressors. *Journal of the Optical Society of America B*, 25(5):754, may 2008.

[186] M. N. Polyanskiy, M. Babzien, and I. V. Pogorelsky. Chirped-pulse amplification in a CO_2 laser. *Optica*, 2(8):675, aug 2015.

[187] A. Weiner. *Ultrafast optics*, volume 72. John Wiley & Sons, 2011.

[188] G. Cheriaux, P. Rousseau, F. Salin, J. P. Chambaret, B. Walker, and L. F. Dimauro. Aberration-free stretcher design for ultrashort-pulse amplification. *Optics letters*, 21(6):414–416, 1996.

[189] B. Wolter, M. G. Pullen, M. Baudisch, M. Sclafani, M. Hemmer, A. Senftleben, C. D. Schröter, J. Ullrich, R. Moshammer, and J. Biegert. Strong-field physics with mid-IR fields. *Physical Review X*, 5(2):021034, 2015.

[190] P. Colosimo, G. Doumy, C. I. Blaga, J. Wheeler, C. Hauri, F. Catoire, J. Tate, R. Chirla, A. M. March, G. G. Paulus, H. G. Muller, P. Agostini, and L. F. DiMauro. Scaling strong-field interactions towards the classical limit. *Nature Physics*, 4(5):386–389, may 2008.

[191] T. Popmintchev, M. C. Chen, D. Popmintchev, P. Arpin, S. Brown, S. Ališauskas, G. Andriukaitis, T. Balčiunas, O. D. Mücke, A. Pugzlys, A. Baltuška, B. Shim, S. E. Schrauth, A. Gaeta, C. Hernández-García, L. Plaja, A. Becker, A. Jaron-Becker, M. M. Murnane, and H. C. Kapteyn. Bright coherent ultrahigh harmonics in the kev x-ray regime from mid-infrared femtosecond lasers. *Science*, 336(6086):1287–1291, 2012.

[192] F. Calegari, D. Ayuso, A. Trabattoni, L. Belshaw, S. De Camillis, S. Anumula, F. Frassetto, L. Poletto, A. Palacios, P. Decleva, J. B. Greenwood, F. Martín, and M. Nisoli. Ultrafast electron dynamics in phenylalanine initiated by attosecond pulses. *Science*, 346(6207):336–339, 2014.

[193] S. Ghimire and D. A. Reis. High-harmonic generation from solids. *Nature Physics*, 15(1):10–16, jan 2019.

[194] M. G. Pullen, B. Wolter, A. Le, M. Baudisch, M. Hemmer, A. Senftleben, C. D. Schröter, J. Ullrich, R. Moshammer, C. Lin, and J. Biegert. Imaging an aligned polyatomic molecule with laser-induced electron diffraction. *Nature Communications*, 6(1):1–6, 2015.

[195] Y. Li, X. Wang, B. Yu, Q. Tang, G. Wang, and J. Wan. Nonsequential double ionization with mid-infrared laser fields. *Scientific reports*, 6(1):1–9, 2016.

[196] R. J. England, R. J. Noble, K. Bane, D. H. Dowell, C. Ng, J. E. Spencer, S. Tantawi, Z. Wu, R. L. Byer, E. Peralta, K. Soong, C. Chang, B. Montazeri, S. J. Wolf, B. Cowan, J. Dawson, W. Gai, P. Hommelhoff, Y. Huang, C. Jing, C. McGuinness, R. B. Palmer, B. Naranjo, J. Rosenzweig, G. Travish, A. Mizrahi, L. Schachter, C. Sears, G. R. Werner, and R. B. Yoder. Dielectric laser accelerators. *Reviews of Modern Physics*, 86(4):1337–1389, dec 2014.

[197] K. L. Vodopyanov. *Laser-based Mid-infrared Sources and Applications*. Wiley Online Library, 2020.

[198] E. A. Peralta, K. Soong, R. J. England, E. R. Colby, Z. Wu, B. Montazeri, C. McGuinness, J. McNeur, K. J. Leedle, D. Walz, E. B. Sozer, B. Cowan, B. Schwartz, G. Travish, and R. L. Byer. Demonstration of electron acceleration in a laser-driven dielectric microstructure. *Nature*, 503(7474):91–94, nov 2013.

[199] K. J. Leedle, A. Ceballos, H. Deng, O. Solgaard, R. F. Pease, R. L. Byer, and J. S. Harris. Dielectric laser acceleration of sub-100 keV electrons with silicon dual-pillar grating structures. *Optics letters*, 40(18):4344–4347, 2015.

[200] K. P. Wootton, Z. Wu, B. M. Cowan, A. Hanuka, I. V. Makasyuk, E. A. Peralta, K. Soong, R. L. Byer, and R. Joel England. Demonstration of acceleration of relativistic electrons at a dielectric microstructure using femtosecond laser pulses. *Optics Letters*, 41(12):2696, jun 2016.

[201] W. Lu, M. Tzoufras, C. Joshi, F. S. Tsung, W. B. Mori, J. Vieira, R. A. Fonseca, and L. O. Silva. Generating multi-GeV electron bunches using single stage laser wakefield acceleration in a 3D nonlinear regime. *Physical Review Special Topics - Accelerators and Beams*, 10(6):1–12, 2007.

[202] D. Woodbury, L. Feder, V. Shumakova, C. Gollner, R. Schwartz, B. Miao, F. Salehi, A. Korolov, A. Pugžlys, A. Baltuška, and H. M. Milchberg. Laser wakefield acceleration with mid-ir laser pulses. *Optics letters*, 43(5):1131–1134, 2018.

[203] J. Lin, Y. Ma, R. Schwartz, D. Woodbury, J. A. Nees, M. Mathis, A. G. R. Thomas, K. Krushelnick, and H. Milchberg. Adaptive control of laser-wakefield accelerators driven by mid-IR laser pulses. *Optics Express*, 27(8):10912, 2019.

[204] I. V. Pogorelsky, M. N. Polyanskiy, and W. D. Kimura. Mid-infrared lasers for energy frontier plasma accelerators. *Physical Review Accelerators and Beams*, 19(9):091001, sep 2016.

[205] A. Schliesser, N. Picqué, and T. W. Hänsch. Mid-infrared frequency combs. *Nature Photonics*, 6(7):440–449, jul 2012.

[206] H. Timmers, A. Kowligy, A. Lind, F. C. Cruz, N. Nader, M. Silfies, G. Ycas, T. K. Allison, P. G. Schunemann, S. B. Papp, and S. A. Diddams. Molecular fingerprinting with bright, broadband infrared frequency combs. *Optica*, 5(6):727, jun 2018.

[207] I. Coddington, N. Newbury, and W. Swann. Dual-comb spectroscopy. *Optica*, 3(4):414, apr 2016.

[208] F. Keilmann, C. Gohle, and R. Holzwarth. Time-domain mid-infrared frequency-comb spectrometer. *Optics Letters*, 29(13):1542, jul 2004.

[209] A. Schliesser, M. Brehm, F. Keilmann, and D. W. van der Weide. Frequency-comb infrared spectrometer for rapid, remote chemical sensing. *Optics Express*, 13(22):9029, 2005.

[210] O. Kara, L. Maidment, T. Gardiner, P. G. Schunemann, and D. T. Reid. Dual-comb spectroscopy in the spectral fingerprint region using OP-GaP optical parametric oscillators. *Optics Express*, 25(26):32713, dec 2017.

[211] Y. Cui, W. Du, M. Chen, and A. Galvanauskas. Generation of 95 fs mid-IR pulses with 1.8 W average power using an Er:ZrF_4 fiber mode-locked oscillator and a nonlinear amplifier. In *CLEO: Science and Innovations*, pages STh4N–7. Optical Society of America, 2021.

[212] W. Du, E. Hyeon, H. Pei, Z. Huang, Y. Cheong, S. Zheng, and A. Galvanauskas. Improved Machine Learning Algorithms for Optimizing Coherent Pulse Stacking Amplification. In *CLEO: Science and Innovations*, pages JTh3A–1. Optical Society of America, 2021.

[213] A. A. Lanin, A. B. Fedotov, and A. M. Zheltikov. Ultrabroadband XFROG of few-cycle mid-infrared pulses by four-wave mixing in a gas. *Journal of the Optical Society of America B*, 31(8):1901, 2014.

[214] S. F. Wandel. *Generation and Application of Ultrashort Coherent Mid-Infrared Electromagnetic Radiation*. PhD thesis, The Pennsylvania State University, 2016.

[215] J. Connolly and R. Donadio. Specifications of raytran material. In *Contemporary Optical Systems and Components Specifications*, volume 181, pages 141–144. International Society for Optics and Photonics, 1979.

[216] L. Yuan, Z. He, G. Lv, Y. Wang, C. Li, and J. Wang. Optical design, laboratory test, and calibration of airborne long wave infrared imaging spectrometer. *Optics express*, 25(19):22440–22454, 2017.

[217] R. A. Kaindl, M. Wurm, K. Reimann, P. Hamm, A. M. Weiner, and M. Woerner. Generation, shaping, and characterization of intense femtosecond pulses tunable from 3 to 20 µm. *Journal of the Optical Society of America B*, 17(12):2086, 2000.

[218] A. Monmayrant, S. Weber, and B. Chatel. A newcomer's guide to ultrashort pulse shaping and characterization. *Journal of Physics B: Atomic, Molecular and Optical Physics*, 43(10), 2010.

[219] C. Homann, N. Krebs, and E. Riedle. Convenient pulse length measurement of sub-20-fs pulses down to the deep UV via two-photon absorption in bulk material. *Applied Physics B: Lasers and Optics*, 104(4):783–791, 2011.